Master's thesis

NTNU
Norwegian University of Science and Technology
Faculty of Engineering
Department of Geoscience and Petroleum

Hanna Margrete Høgset

A STUDY OF FAILURE IN FRICTIONAL AND LOW-COHESIVE MATERIALS UNDER THE LOAD OF GROUND ANCHORS THROUGH SMALL-SCALE PHYSICAL MODEL TESTS AND NUMERICAL SIMULATIONS

Master's thesis in Geotechnology
Supervisor: Professor Charlie Chunlin Li
Co-supervisor: Are Håvard Høien
March 2021

NTNU
Norwegian University of
Science and Technology

Hanna Margrete Høgset

A STUDY OF FAILURE IN FRICTIONAL AND LOW-COHESIVE MATERIALS UNDER THE LOAD OF GROUND ANCHORS THROUGH SMALL-SCALE PHYSICAL MODEL TESTS AND NUMERICAL SIMULATIONS

Master's thesis in Geotechnology
Supervisor: Professor Charlie Chunlin Li
Co-supervisor: Are Håvard Høien
March 2021

Norwegian University of Science and Technology
Faculty of Engineering
Department of Geoscience and Petroleum

NTNU
Norwegian University of
Science and Technology

NTNU | Faculty of Engineering
Department of Geoscience and Petroleum

MASTER'S THESIS

Project Description

Name of Candidate: Hanna Margrete Høgset

Title of Thesis: A STUDY OF FAILURE IN FRICTIONAL AND LOW-COHESIVE MATERIALS UNDER THE LOAD OF GROUND ANCHORS THROUGH SMALL-SCALE PHYSICAL MODEL TESTS AND NUMERICAL SIMULATIONS

Norwegian Title: BRUDD I FRIKSJONS- OG LAVKOHESIVE MATERIALER SOM FØLGE AV BELASTNING AV STAG, GJENNOM SMÅSKALA MODELLFORØK OG NUMERISKE SIMULERINGER

Detailed Description: The project aims to study failure in frictional and low-cohesive materials under the load of ground anchors. The major objectives of the work are:

1) A small-scale apparatus is designed and constructed for tests of 2D physical models that replicate pullout of a ground anchor buried in frictional and low-cohesive materials.
2) Appropriate types of materials are determined and acquired. The frictional and low-cohesive materials for the model tests are prepared or made from the acquired materials. Relevant mechanical properties of the model materials are detemrined.
3) A series of model tests are performed on the apparatus to study the failure pattern in the materials.
4) Numerical simulations are carried out using RS2 to study the stress field and the failure in the model material. The numerical output is compared with the physical model test results.

From these four objectives, the candidate analyses findings with respect to the main goal of the study, and recommends future work.

Main Profile: Engineering- and Environmental Geology

Specialization: Engineering Geology and Rock Mechanics

Time Frame: 31.08.2020 - 01.03.2021

Charlie Chunlin Li, Professor/hovedveileder

NTNU, 25.02.2021

Abstract

Ground anchors are structural members that transmit an applied tensile load to soil or rock mass at a certain ground depth. To date, there exists limited knowledge on how failure initiates and progresses through the rock/soil under the load of an anchor. This project aims to study failure development in frictional and low-cohesive materials under the load of ground anchors through small-scale physical model tests and numerical simulations.

The physical model setup consists of a transparent PVC test chamber, a rigid "anchor block", and hydraulic jack, instrumented with a camera, an extensometer and load cell to continuously record the failure development and resistance from the material, as the anchor block is pushed through the specimens. The results are applied to verify two-dimensional FEM numerical models in RS2.

The load-displacement response of the anchor under loading may be described by a 1) pre-peak behavior, 2) peak resistance, 3) post-peak behavior with resistance decrease, and 4) constant resistance. Pre-peak behavior involves a linear-elastic response to a small anchor displacement, typically 1-2 mm. This elastic phase accounts for 65-95 % of the peak resistance. The post peak phase is characterized by the development of a delimited failure body from the underlying, stationary material. The resistance decreases gradually, until the separated failure body is lifted by the anchor and/or slips off at a constant resistance.

From the results of the small-scale physical model tests, it has been shown that in the frictional materials, a small vertical displacement of the anchor mobilizes a larger body of material than the final pullout body defined by the failure planes. Failure initiates at a point low on the anchor's socket, typically up to 1/4 of its length, depending on the material type. It propagates outward with an inclination to the anchor axis, thus creating a cone-shaped pullout body. Cone angles generally vary with a few degrees from the peak friction angle of the material. The failure planes are straight, curved or a combination, the latter being observed in most of the tests.

The low-cohesive materials demonstrated similar characteristics as the frictional materials, i.e. failure created a delimited body the shape of an inverted cone. The angle of the cone was larger than in the frictional materials. The peak resistance was also considerably higher, and related to the material's strength.

Peak resistance values of both frictional and cohesive materials show that there is a considerable amount of resistance which cannot be explained solely by the weight of the pullout body. Numerical simulations reveal that this increased resistance may be explained by the presence of arching effect in the materials. Namely, an increased pressure arch, inducing a vertical component on the socket, resisting the pullout. The angle of this pressure arch was found to be more narrow in frictional material than in cohesive material, and has been shown to affect the shape of the failure body. Failure surfaces are studied by

tracking the zones of maximum strain, in addition to points of shear and tensile failure. The peak and residual friction angle are found to be controlling parameters in the frictional material, while Young's modulus has been found to have a significant influence on the extent and angle at which failure propagates through the low-cohesive materials.

Numerical models have successfully extended the study on the physical phenomena revolving arching effect and failure in the materials. Arching effect has been identified in both the frictional soils and low-cohesive materials. Arching effect unquestionably increases the resisting stresses from the material, and affects where failure is expected to develop. Cohesion and tensile strength influence the arch shape, and increase the resistance in cohesive materials.

Sammendrag

Forankringsstag, eller ankere, er strukturelle legemer som overfører påførte strekkspenninger til grunnen ved et bestemt dyp. Per dags dato er det begrenset kunnskap på hvordan brudd initieres og propagerer gjennom berg- og løsmasser ved overbelastning av et anker. Dette prosjektet har som mål å studere bruddforløp i friksjons- og lavkohesive materialer som er belastet av et anker, gjennom småskala fysiske modellforsøk og numeriske analyser.

Oppsettet til den fysiske modellen består av et transparent testkammer av pleksiglass, en stiv "ankerblokk" og hydraulisk jekk, utstyrt med et kamera, et ekstensometer og lastcelle som kontinuerlig måler bruddutviklingen og lasten idet ankerblokken skyves gjennom prøvene. Resultatene benyttes til å verifisere todimensjonale FEM-modeller i RS2.

Last-forskyvnings-reaksjonen til den belastede ankerblokken utviser en karakteristisk oppførsel i alle materialene: 1) Pre-peak (før maksimum), 2) peak (maksimal) last, 3) post-peak (etter maksimum) med avtakende last, og 4) konstant last. Pre-peak oppførsel kjennetegnes av en lineær-elastisk respons til en liten forskyvning av ankeret, typisk mellom 1 og 2 mm. Denne elastiske fasen utgjør om lag 65-95 % av den maksimale lastsverdien. Under post-peak fase utvikles et tydelig avgrenset utrivningslegemene imens lasten gradvis avtar. Det separerte utrivningslegemet løftes av ankeret eller faller av, slik at ankeret utviser tilnærmet konstant last. Resultater fra de fysiske modellforsøkene har vist at det ved små forskyvninger mobiliseres et større volum av materialet enn det endelige utrivningslegemet som avgrenses av bruddflatene. Brudd initieres fra et lavt punkt på forankringslengden, opp til $\frac{1}{4}$ av forankringslengden, avhengig av materialet. Bruddet propagerer oppover med en vinkel til forankringsaksen, og skaper dermed et konisk utrivningslegeme. Vinkelen varierer typisk med noen grader fra peak friksjonsvinkel til materialet. Bruddflatene er rette, kurvede eller en kombinasjon. Sistnevnte ble observert i flerparten av testene. De lav-kohesive materialene utviser liknende oppførsel som friksjonsmaterialene, nemlig brudd som danner et avgrenset bruddlegeme med form som en endevendt konus. Vinkelen til konusen var større enn i friksjonsmaterialene. Peak last var også betydelig høyere, og relatert til materialenes styrke.

Peak lastsverdi for både friksjons- og lavkohesive materialer viser at det er en betydelig andel av lasten som ikke kan forklares ved vekten av utrivningslegemet alene. Numeriske simuleringer avdekker at denne økte lasten kan forklares ved tilstedeværelsen av spenningsbuer i materialene. Det vil si, en bue med forhøyet trykk som induserer en vertikal spenningskomponent på forankringslengden, som motsetter seg oppløftsbevegelsen. Vinkelen til denne spenningsbuen er smalere i friksjonsmaterialet enn i lavkohesive materialer, og påvirker formen på bruddlegemet. Bruddflatene studeres ved å spore sonene med maksimal tøyning, i tillegg til punkter med skjær- og tensilbrudd. Peak og residual friksjonsvinkel har tydelig innvirkning på bruddformen i friksjonsmaterialet, mens elastisitetsmodulen har vist seg å ha betydelig innflytelse på vinkelen og omfanget til brudd gjennom de lavkohesive

materialene. De numeriske modellene har på en vellykket måte utvidet studien på de fysiske fenomenene rundt dannelsen av spenningsbuer, så vel som utviklingen av brudd i friksjons- og lavkohesive materialer. Spenningsbuer er identifisert begge materialtypene. Spenningsbueeffekten øker utvilsomt de motsettende spenningene i materialene, og påvirker hvor brudd utvikles. Kohesjon og tensilstyrke påvirker formen til spenningsbuene, og øker utrivningsmotstanden i kohesjonsmaterialene.

Acknowledgments

This thesis concludes my small contribution to the understanding of failure development and arching effect caused by the load of rock anchors. It also marks the end of my time at the Department of Geoscience and Petroleum (IGP) at NTNU, and in the amazing student city of Trondheim.

First of all, I owe a great thanks to my supervisor and ROCARC Project Manager, Professor Charlie Chunlin Li. Li introduced me to the project, which suited my interests very well. His own interest in the subject is almost contagious, and he has been a positive driving force at times when my own motivation ran low during the most meticulous work. Additionally, he has always been a friendly face at the department, and is eager on sharing his expertise. I must also thank my co-supervisor, Are H. Høien, for his helpful feedback on my results, and some food for thought.

Handing in my thesis is a very humbling experience. It is in no way accomplished singlehandedly, but by the smaller and larger contributions of many. On this note, I wish to extend my deepest gratitude to Jon Runar Drotningshaug and Gunnar Vistnes at the Rock Mechanics Laboratory at IGP. I have bounced many ideas off of them, and they helped me greatly in both designing my model and conducting the experiments. Especially Drotningshaug has put many hours of labor into assisting my work, while providing many fun conversations during my weeks in the lab. I must also acknowledge the men at the workshop, herein Noralf Vedvik, for constructing the physical model according to my ever-changing instructions. Also, thank you Simon Alexander Hagen, Engineer at SINTEF, for that extra – and much needed – finesse added to the physical model on a short notice, and for teaching me the software. I must also thank Professor Alexandre Lavrov, for helpful feedback on my first numerical model drafts, and last – but not least – my close pal Lars S. Engen, for reading over parts of my thesis.

Finally, I owe thanks to so many people that I am lucky to have met during my time as a student in Trondheim. Friends who have provided good academic conversations, but mainly many laughs and joyous experiences which I cherish deeply. I cannot possibly mention them all, but some are extra special to me: My roommates in Lisbon, Bendik, Martin and Anna; and of course the girls in “Gjengen Allianse”, who have been with me since Day One of my degree. However, two people have been there for me through thick and thin over the past 15 years – my dear friends from home, Andrea and Thea. I am very lucky to know you both. Finally, thank you to my siblings and parents for your support and encouragement throughout the years.

Hanna Margrete Høgset
Trondheim, February 2021

Preface

This thesis presents a Master's project within the study profile Engineering Geology and Rock Mechanics, course code TGB4945 at the Norwegian University of Science and Technology, NTNU. The project was carried out during the fall semester of 2020 and early 2021.

The project is intended to contribute to the work involved with an ongoing research project, ROCARC, at the Department of Geoscience and Petroleum at NTNU and SINTEF. Thus, the objectives of the thesis are adopted from some of the main goals of ROCARC, though at a much smaller scope and time frame.

It is recommended that the reader possesses some knowledge on the the topics of Physics, Rock Mechanics, Soil Mechanics and Numerical Modeling, as the thesis touches on all of these topics, and an attempt has been made to keep the theory short.

I hope this work may provide some help into the understanding of failure development and arching caused by the loading of ground anchors, and show how small-scale apparatuses and numerical models may be combined for future studies on ground anchor dimensioning.

H.M.H.
Trondheim, February 2021

Contents

List of Figures

List of Tables

List of Abbreviations

DST	Direct Shear Test
FEM	Finite Element Method
GSD	Grain Size Distribution
ISRM	International Society for Rock Mechanics
M-C	Mohr-Coulomb failure criterion
N/A	Not applied or not available
NA	Nominal Aperture
NPRA	Norwegian Public Road Authorities
NTNU-IGP	Norwegian University of Science and Technology, Department of Geoscience and Petroleum
POM	Polyoxymethylene
PVC	Polyvinyl Chloride
UCS	Uniaxial Compressive Strength
Unk.	Unknown

Test Materials

A.1	Test material A.1: 0-3 mm crushed eclogite, dry
A.2	Test material A.2: 0-3 mm crushed eclogite, moist
B.1	Test material B.1: 0.5-6.3 mm crushed eclogite, dry
B.2	Test material B.2: moist 0.5-6.3 mm crushed eclogite, moist
C.1	Test material C.1: 0-3 mm crushed eclogite with 4 % cement
C.2	Test material C.2: 0-3 mm crushed eclogite with 2 % cement

1 Introduction

Rock or ground anchors are structural members that transmit an applied tensile load to the soil or rock mass at a certain ground depth. High capacity anchors are commonly used for stabilizing slopes, retaining walls and large-scale infrastructure, such as building foundations, wind turbines, concrete dams and bridge towers. It is of great importance to ensure that the anchors are correctly dimensioned, as a failure of the anchor may lead to structural damage, and potentially great economic or social consequences.

The principles behind anchoring dimensioning are primarily based the four failure modes:

A) rupture of the steel tendon,

B) failure of the tendon-grout interface/bond,

C) failure of the grout-rock bond, and

D) failure and uplift of a conical body of rock/soil mass.

Failure mechanisms A) and B) are thoroughly studied and well known. There are, on the other hand, great uncertainties attached to modes C) and D), as there currently exists limited knowledge on how failure initiates and progresses through the rock/soil and in the rock-grout interface following over-stressing of the anchor. For this reason, a research project, *ROCARC*, was established by the Department of Geoscience and Petroleum at the Norwegian University of Science and Technology, that aims to investigate:

1) how the load from the anchorage is transferred to the rock mass and how failure occurs in the rock mass,

2) how arching effect occurs during loading of the anchor,

3) how the bond strength between the rock and grout may be realistically determined, and

4) the existing guidelines for rock anchor design.

The overall objective of the project is to develop an updated approach for dimensioning rock anchors that leads to realistic and economical solutions. The project work includes laboratory model tests, numerical modeling and field trials. An advanced, two-dimensional test rig will be constructed for the laboratory work, which is to be begin during the spring of 2021.

To contribute to this work, a small-scale physical model has been developed to simulate overstressing of an anchor, using frictional and low-cohesive materials. The purpose of these small-scale tests is to achieve preliminary knowledge on the failure development, shape and arching effect in the frictional materials, which in turn may provide valuable insight to the work involving the full-scale test rig. The small-scale model examines

different frictional material, herein 0-3 mm and 0.5-6.3 mm crushed eclogite, both moist and dry. Additionally, a small amount of cement is added to the 0-3 mm eclogite, to create low-cohesive materials simulating a weak rock. This is intended to reveal any significant differences between the frictional and low-cohesive material. Finite Element Method numerical models are created using RS2, to supplement the physical experiments and extend the study on the mechanisms that occur at the point of failure.

2 Theory

2.1 Ground Anchoring

The information provided in this section is largely extracted from the TGB4500 specialization project (Høgset, 2020). This theory is considered essential to the understanding of anchoring procedures in rock and soil, and the relevant failure mechanisms which will be examined through the physical and numerical modeling in this thesis.

2.1.1 General Principles

Ground anchors are used for a wide variety of purposes, including stabilizing rock slopes, underground excavations, retaining walls and large-scale infrastructure, such as foundations, wind turbines, concrete dams and bridge towers. The anchoring process includes inserting single or multiple bars, wires or strands (multiples are termed cables) deep into a borehole, and bonding it to the soil or rock mass at its distal end, using cement grout, resin or mechanical fixtures. The tendon between the bonded anchorage at the distal end and exposed head at the surface remains free, that is, unattached to the ground, while the head may be attached to the structure in need of stabilizing or to a plate, grid or other structural element which distributes tensile stresses to a wider surface area. The anchor is post-tensioned or left passive before the attachment.

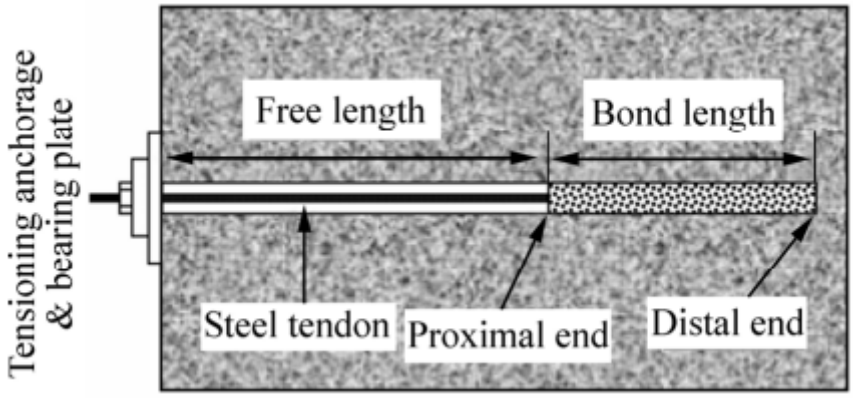

Figure 2.1: Basic components of an anchor (Showkati et al., 2015)

2.1.2 Mechanisms of Anchor Failure

While anchor scale, capacity and detailed design installation may vary significantly between purposes and projects, the overall principles of ground anchor dimensioning remain largely unchanged since the 1970s (Brown, 2015), and are based on the following four types of failure, shown in Figure 2.2:

A) Rupture of the steel tendon,

B) Grout-tendon bond failure,

C) Rock-grout bond failure, and

D) Uplift from a conical failure surface in the rock mass.

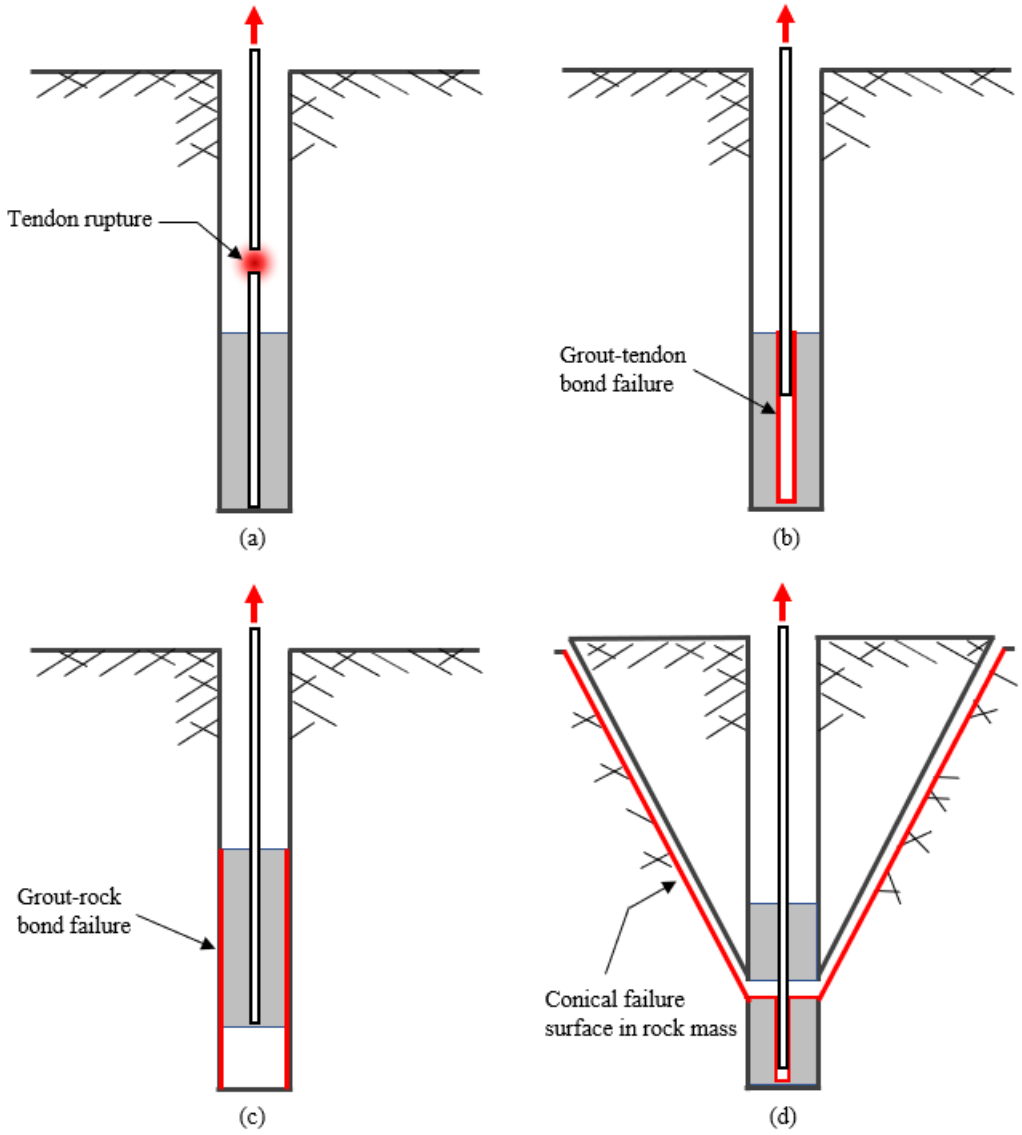

Figure 2.2: Failure mode A – rupture of the steel tendon; (b) Failure mode B – gorut-tendon bond failure; (c) Failure mode C – rock-grout bond failure; and (d) Failure mode D – a conical failure surface in the rock mass

In general, the ultimate tensile capacity of an anchor under failure modes A, B, C and D can be given as Q_{tu}, Q_{tgu}, Q_{rgu} and Q_{ru}, respectively. Then, following (Kim and Cho, 2012), the ultimate capacity, which is the dimensioning requirement, will be the minimum of those four values, i.e.:

$$Q_u = \min|Q_{tu}, Q_{tgu}, Q_{rgu}, Q_{ru}| \tag{1}$$

Pease and Kulhawy (1984) noted that the criteria for failure modes A and B, are well developed and are matters of only structural concern governed by the material properties of the steel and grout. As they are not regarded to be of concern in this study, the reader

is urged to review the specialization work which covers these criteria for more information (See Høgset, 2020). On the other hand, criteria for modes C and D are of a geotechnical character – predominantly empirical, derived from summaries of load test results available at the time. Modes C and D are regarded most relevant to this work, and will be presented here. Additionally, a more detailed description of anchoring in frictional soil will be given in section 2.1.3.

Design against failure mode C: Rock-Grout bond failure

The mechanisms that provide resistance to failure mode C, grout-rock bond failure, are a combination of adhesion, friction and mechanical interlocking, with friction being the main contributor after an initial displacement. The equation for the ultimate rock-grout axial shear resistance is therefore given as

$$Q_{rgu} = 2\pi r_g \int_0^{l_{brg}} \tau_{rgu}(z)dz \tag{2}$$

where r_g is the outside radius of the grouted annulus around the tendon, l_{brg} is the length of the rock-grout bond, and $\tau_{rgu}(z)$ is the shear resistance generated at distance z along the interface. The shear resistance along the interface is assumed to be uniformly distributed, making τ_{rgu} constant, so that the equation above simplifies to

$$Q_{rgu} = 2\pi r_g l_{brg} \tau_{rgu} \tag{3}$$

The value of τ_{rgu} is either selected based on rock type and condition using tables of presumptive values or by performing pullout tests of trial anchors at site (Brown, 2015).

Design against failure mode D: Uplift from a conical failure surface in the rock mass

Assuming the interface between the grout and rock remains intact, several methods exist for calculating the rock mass' resistance against uplift in an isotropic rock. All of the methods assume that a defined body of rock mass, with a simple geometric shape of an inverted cone, is separated and pulled up from the ground by the axial force applied to the anchor. The main approaches for analyzing the uplift resistance of the conic body are through the (Berg-Christiensen and Ongstad, 2010):

1) Weight of the conic body of rock mass.

2) Shear strength of the conic body.

1) Uplift Resistance by Weight of the Conic Body of Rock Mass

The most conservative method of estimating the resistance to rock mass uplift involves assuming that uplift is resisted solely by the weight of conic body of rock mass. Thus, the conic body is expected to be completely loosened from the surrounding rock mass, and

no bridges or interlocking elements exist, such that the surfaces have no shear strength, and thereby generate no joint surface friction. These assumptions ignore the fact that the rock mass generally has shear and/or tensile strength which must be overcome for uplift to occur.

The angle of the cone may vary according to the assumed rock mass properties. The most common angles used are 60° for weak, tightly jointed or weathered rock mass, and 90° for strong, low jointed rocks. One may also use 80° for rock mass of moderate quality, or 120° for high quality rock mass (Duncan, 1999; Norwegian Public Road Authorities, 2004 and 2010). The location of the apex will typically be at the center or end of the socket length, and relies to some extent on the rock mass quality. Usually, the apex is assumed to be at the center of the socket when dealing with low quality rock mass (either weak or tightly jointed) or for cases in which the properties are unknown due to lack of pull-out test data. The apex is placed at the end when the rock mass is known to be of good quality with few joints – confirmed by pullout-tests, or when the loads from the anchor are transferred to rock mass by use of an end plate or wedges (Littlejohn and Bruce, 1975).

For a cone angle θ_c and apex of the cone located at the center of the embedment length, the force required to uplift the weight of the rock cone, W_c, may be given as (Brown, 2015):

$$Q_{ru} = \frac{1}{3}\pi\gamma \tan^2 \frac{\theta_c}{2} \left(D + \frac{L}{2}\right)^3 \tag{4}$$

where γ is the unit weight of the rock, D is the depth from the surface to the top end of the embedment length, and L is the grouted embedment length. For embedment beneath the ground water level, the submerged unit weight should be used.

When multiple anchors are installed either in a row or grid, the anchors transfer the stress in specific patterns. In a row, the cones will overlap or interact, as illustrated in Figure 2.3 b). For such cases, one may use a simplified 2D approximation, by assuming that the anchors influence a prism-shaped zone with a triangular cross-section. Thus, the uplift resistance per unit length of the anchor row is given as (Brown, 2015):

$$Q_{ru} = \frac{1}{2}\frac{\gamma}{s} \left(D + \frac{L}{2}\right)^2 \tan \frac{\theta_c}{2} \tag{5}$$

where s is the spacing between anchors along the row.

2) Uplift Resistance by Shear Strength of the Conic Body

The second approach also presumes failure of a conic body of the rock mass, but assumes that the shear or tensile strength or cohesion of the rock mass alone provides the resistance against uplift of the conic body (Coates, 1970; Hobst and Zajíc, 1983; Anon, 1966 (as cited by Brown, 2015; and Kim and Cho, 2012)). The strength and cohesion are constants that depend on the quality of the rock mass. For cases where the in-situ stresses are zero,

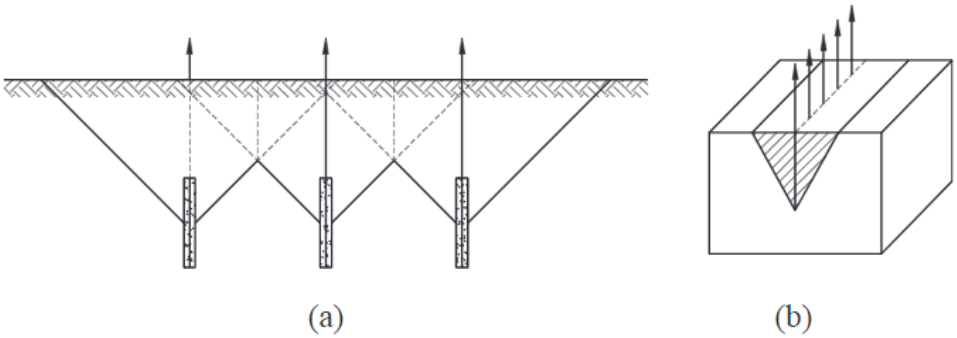

Figure 2.3: Interaction of uplift cones in a single row of tensioned anchors a) parallel, vertical cross-section by Littlejohn (1993), and b) a simplified triangular cross-section normal to the row, by Hobst and Zajíc (1983).

and no other stresses are imposed from structures on the rock mass, the shear strength may be conservatively assumed as equal to the rock mass cohesion (U.S. Army Corps of Engineers, 1994). Some choose to apply both the weight of the cone and the estimated resistance from cohesion, shear or tensile strength to the total uplift resistance (Brown, 2015).

Brown (2015) also states that the 90° uplift cone assumption may not always be as valid for cases of deep anchors, as the controlling surface mechanisms differ from those of shallow, fully grouted anchors, which display this phenomena more commonly. "The deeper the anchor, or the greater the ratio of the anchor depth, D, to the embedment length, L, the less likely the conical rock mass uplift mechanism is to control the behavior of the post-tensioned anchor" (Brown, 2015).

2.1.3 Anchoring in Soils

Weak rocks, meaning both hard soils and soft rocks, are often encountered in the shallow stratums around the world, thus forming the foundation ground for many construction projects (Nickmann et al., 2006). Determining whether a material is a hard soil or soft rock may be difficult, though also crucial, as it determines whether applying Soil Mechanics or Rock Mechanics is the most appropriate approach. One way to distinguish rocks from soils – that is, from frictional soils – is by the Mohr-Coulomb strength parameter *cohesion*, c. Cohesion represents the *pure shear strength* of the material, and is independent of the material's *angle of internal friction*, φ (Li, 2017). A material is often considered a soil or loose material if its shear strength is a result of purely frictional resistance, that is, $c = 0$. Some soils, such as clays, do possess true cohesion, though it is due to inter-particle bonding rather than crystallization as it is in rocks.

The Mohr-Coulomb strength criteria is widely used in geotechnincal applications:

$$\tau = c + \sigma_n \tan \varphi \tag{6}$$

where τ is the shear strength that can be developed on a plane a-b, with a normal stress, σ_n, acting on said plane, and φ is the internal friction angle of the material (Zhao, 2000). See the relationship between the Mohr-Coulomb parameters, principle stresses and a shear stress on plane a-b in a specimen in Figure 2.4:

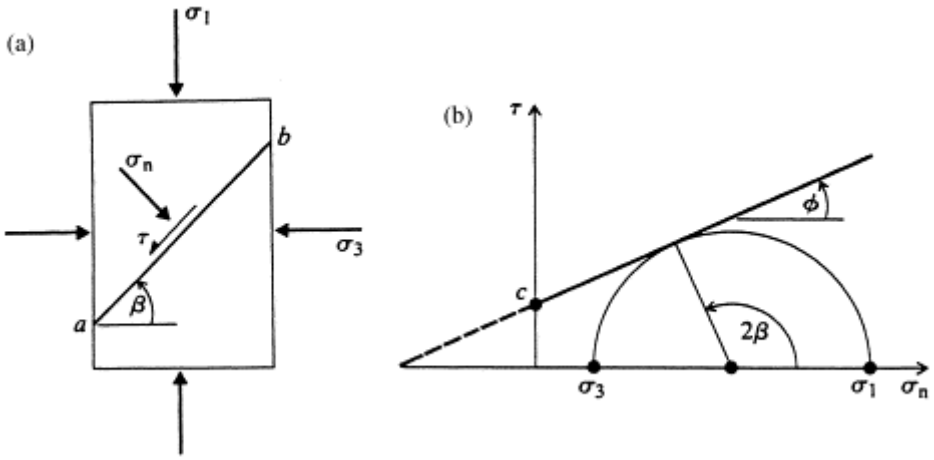

Figure 2.4: The Mohr–Coulomb strength criterion: (a) shear failure on plane a–b, and (b) strength envelope of shear and normal stresses, modified from ISRM (2000)

The International Society for Rock Mechanics (ISRM) (1978), classifies a material with uniaxial compressive strength, UCS, $\leq$ 0.25 MPa as a soil, regardless of its texture, structure, jointing or cohesion. Cohesive soils, such as clays, are not within the scope of this thesis, however when anchored in, they are assumed to fail in the cone-shaped failure wedge described earlier, with an apex angle twice the angle of internal friction, φ (Hobst and Zajíc, 1983). The anchor pullout resistance is generally lower in cohesive soils than the frictional soils.

Anchoring in frictional, non-cohesive soils

An anchor is loaded in its neutral state by the pressure of the overlying soil. If a tension is applied to the anchor equal to the downward acting force arising from this pressure, the anchor will not move. However, using this limit as the governing design criterion leads to borehole depths and anchor cross-sections that are oversafe and uneconomic. Therefore, this condition is not applied in practice. By allowing some deformation of the ground above the anchor and some degree of pullout, greater anchor loads may be considered than if no movement is allowed. However, the exact stress state in the soil as a result of the anchor tension is difficult to express theoretically. This is mostly because the soils cannot be considered elastic materials while they are undergoing plastic deformation, as tensile stresses cannot occur within the soil. Shear failure is expected to occur in the soil as a conical shape, when the ultimate shear strength is reached at its surface, the cone angle being equal to twice the angle of internal friction, φ (Hobst and Zajíc, 1983).

The anchor capacity is dependent on the soil's degree of compaction. Increasing compaction increases the angle of internal friction and coefficients of transverse expansion. Stresses

from the anchor are introduced to a wedge of mass surrounding the socket, creating radial stresses. These radial stresses are larger in more compacted soils, and contribute to an increased shear strength of the soil and resistance to pullout. Such soils often show dilatancy at the point of shear failure, which increases pressure in the soil, thus further impeding anchor pullout. In less compacted soils, shear failure may cause increased compaction, which in turn reduces the soil volume. This makes it difficult to ensure sufficiently high resistance from pullout in uncompacted soils. Anchor pullout does not cause shearing above the anchor, in fact, in most cases the soil flows around the anchor (Hobst and Zajíc, 1983).

The resistance against pullout in frictional soils depends considerably on the type and arrangement of structures used for fixing the anchor. An anchor with repeating fixtures along its entire length, extending to the surface, will transfer stresses only to a comparatively narrow cylinder of the soil surrounding it. Near the surface, this cylinder widens to a funnel shape. With an end-plate fixed anchor, a greater part of the soil receives the stress transmitted by the anchor, thus increasing the pullout resistance. Many scaled model experiments have been performed throughout the years on various anchor fixtures buried in frictional soils. Niroumand (2017) published a summary from an extensive literature review on previous theoretical and experimental works focusing on pullout capacity of end-plated anchors, some of which have been paired with numerical analysis'. Though the findings can not be gathered to a single conclusion for the ultimate uplift capacity for soil anchors, some typical failure modes were found to be proposed by several authors. Mainly, three distinct failure forms, as shown in Figure 2.5.

For a vertical grouted type anchor, as will be simulated in the model tests of this study, the failure mode of the frictional cylinder proposed by Majer (1955) (Figure 2.5 (a)) is not relevant, as the cross-section directly above the anchor will be free of material. The soil cone method (Mors, 1959) and the circular failure surface (Ball, 1961; Baker and Konder, 1966) may on the other hand be more of interest, as they are similar to the cone shaped failure mode previously described by Hobst and Zajíc (1983) for vertical embedded rock and soil anchors.

The failure cones with the circular surfaces were observed by Ball (1961) and Baker and Konder (1966), and found to extend from the edge of the anchor toward the surface, intersecting it with an inclination of roughly $45° - \varphi/2$ (Liu et al., 2012), as shown in Figure 2.5 (c).

As mentioned, the proposed soil cones normally cause over-conservative dimensions for shallow anchors, as the uplift capacity is considered equal to the weight of the pullout body alone, thus disregarding frictional stress along the failure surface. On the other hand, assuming the cone shape leads to overestimating the capacity of deep soil anchors, as the failure cone rarely extends fully to the surface, and the failure body becomes smaller than the predicted soil cone (Liu et al., 2012).

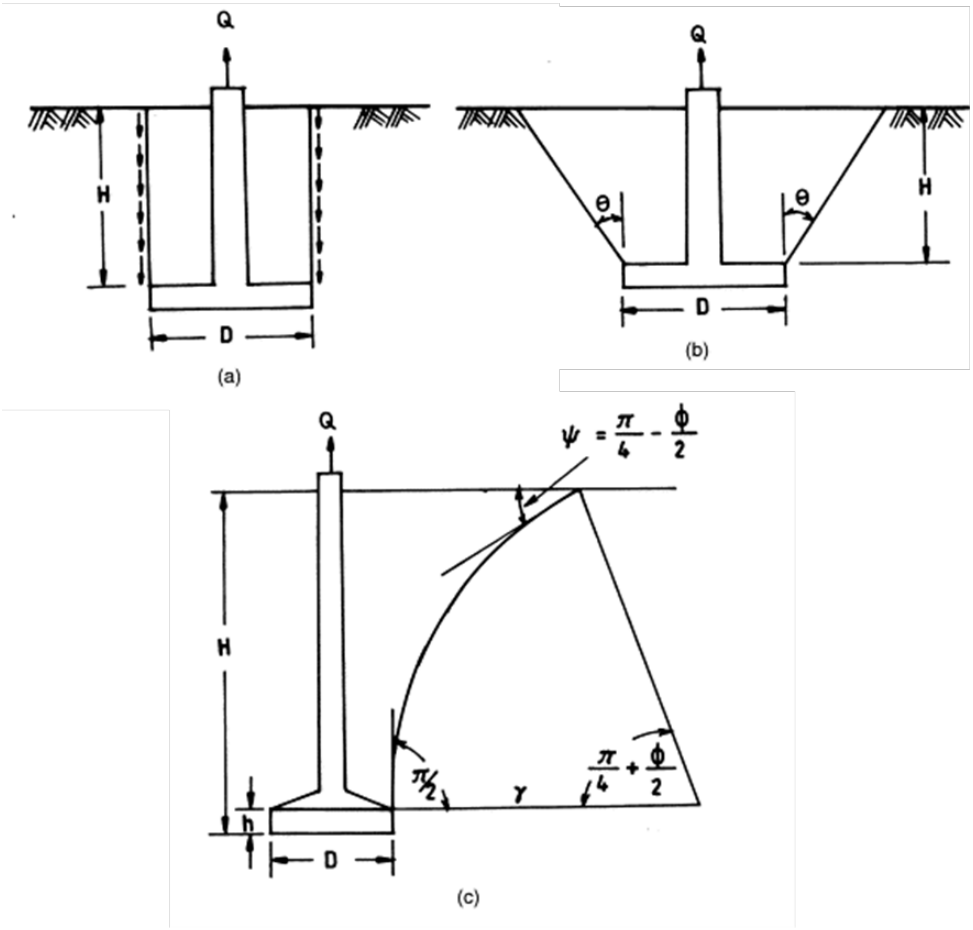

Figure 2.5: Predicted failure shapes with end-plated anchors: (a) friction cylinder method (Majer, 1955); (b) soil cone method (Mors, 1959); (c) circular arc failure surface (Ball, 1961). From Ilamparuthi and Muthukrishnaiah (1999).

Even with extensive research on the behavior of anchors, is there still a lack of understanding of the anchor's interaction with the surrounding soil during uplifting. Most studies have focused on measuring the final shape of the pullout body (Liu et al., 2012), thus disregarding how the failure develops in the soil. Further understanding will require verification of the failure shape to true rupture surfaces for varying anchor and soil parameters (Niroumand, 2017).

2.2 Arching Effect in Soils

Terzaghi (1943) described a soil phenomena which may be observed both naturally in the field as well as in the laboratory, namely the "arching effect". The arching effect occurs when a granular soil mass yields relative to adjoining, stationary soil masses. Shearing stresses are mobilized in the yielding soil, which resist, or counteract, the relative movement. The effect itself is a load transfer mechanism. "The soil is said to *arch* over the yielding part" (Terzaghi, 1943).

The effect was illustrated with the theoretical and experimental "Yielding Trapdoor" model: A trapdoor lies beneath a horizontal soil bed. The trapdoor gradually displaces downward, causing a downward movement to a yielding mass of soil above it, while the adjoining soil remains stationary. If the trapdoor is wide, shear failure occurs along two slip surfaces which originate from the outer boundaries of the trapdoor and rise to the surface of the soil, as shown in Figure 2.6.

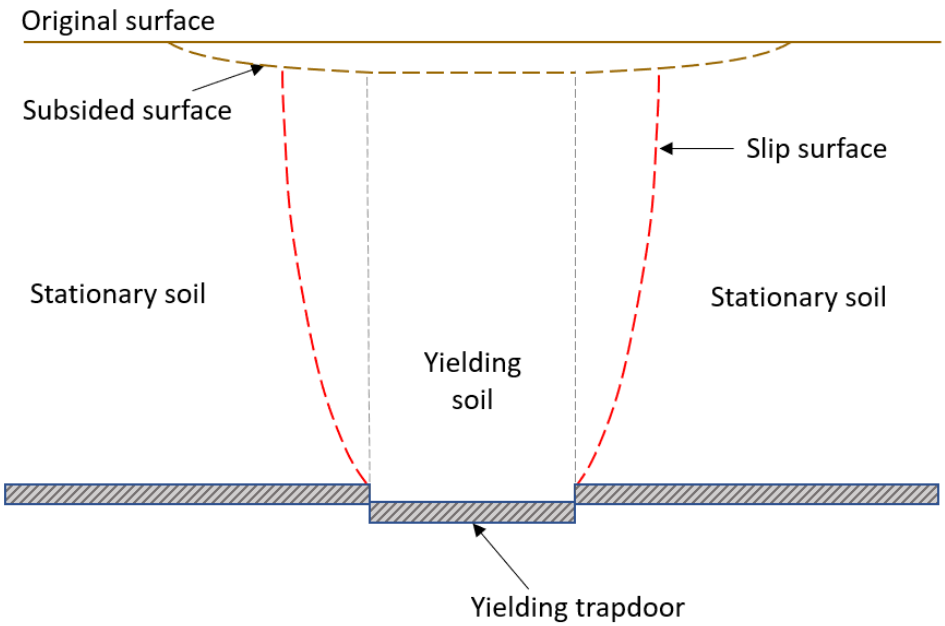

Figure 2.6: A simplified replication of Terzaghi's (1943) yielding trapdoor problem.

If the trapdoor width is small enough, its relative movement will cause a small increase in pressure in the stationary soil, and an equal pressure reduction in the yielding soil above the trapdoor. This is due to the vertical component of the mobilized shearing resistance at the stationary-yielding interface. In effect, the stationary soil carries some of the weight of the yielding soil mass, as a result of the arching effect.

At the edges of the trapdoor, an abrupt increase in vertical stress is induced. This discontinuity in the vertical stress distribution requires the existence of a zone of *radial shear*, illustrated in Figure 2.7. The soil located within the high-pressure zones expands laterally, due to this radial shear (Terzaghi, 1943).

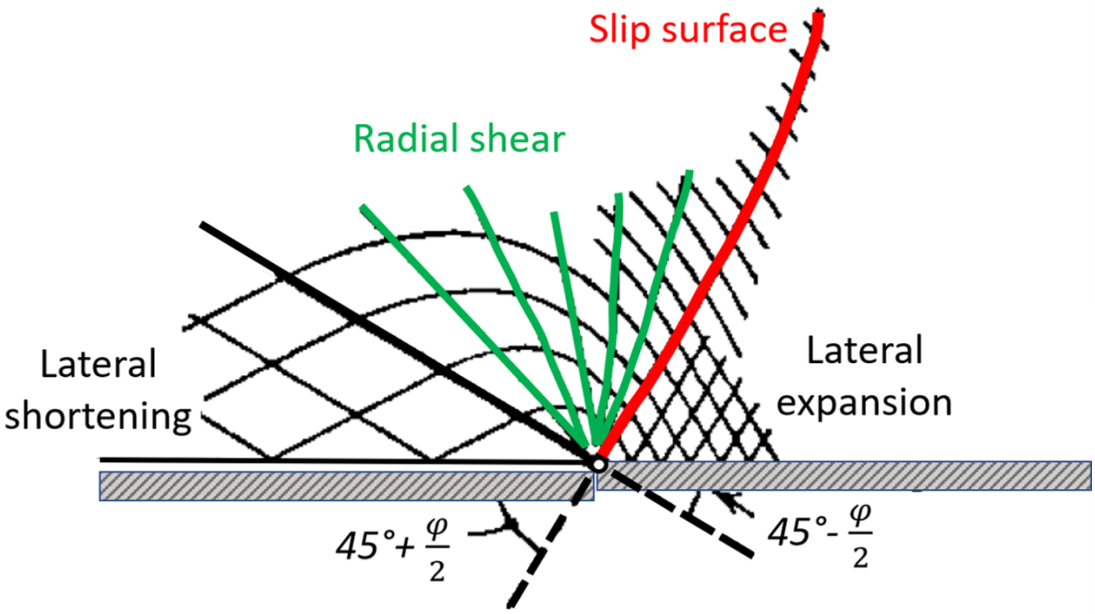

Figure 2.7: Illustration of radial shear zone at the edge of the trapdoor, modified from Terzaghi (1943).

To clearly visualize the state of stress in the retained soil, assume the following:

1) A granular soil settles between two vertical, stationary, rough walls, and

2) the settlement is large enough so that the weight of the soil becomes partially supported by fully developed friction between the soil and the walls.

The frictional resistance induced in the soil will cause a change in the direction of the principal stresses acting on a soil element. Handy (1985) demonstrated this change in principle stresses by using the Mohr circle (Figure 2.8 (a)): Minor principle planes drawn through the Mohr circle poles show that the minor principle stress trajectory is in the shape of a concave, continuous compression arch, meaning that the major principle stress radiates from the center line (Handy, 1985), as shown in Figure 2.8 (b) on the next page.

To date, there has not been established a consensus regarding the exact shape and composition of the soil arch (Lai et al., 2020). However, when the yielding portion of soil has a downward movement relative to the stationary parts (thus creating upward shear stress at the interface), the stress redistribution is often referred to as *positive soil arching*, as the arch is supportive and convex. Reversing the movement will reverse the shearing actions, creating *negative soil arching* and a concave arch. However, at some height above the trapdoor, displacement of the trapdoor appears to have no effect on the stress state in the soil, so that the vertical stress remains equal to the overburden stress (Terzaghi, 1943). This level is often termed the "equal settlement plane" in geotechnics. Figure 2.9 on the following page illustrates the equal settlement plane above a positive soil arch between two vertical walls:

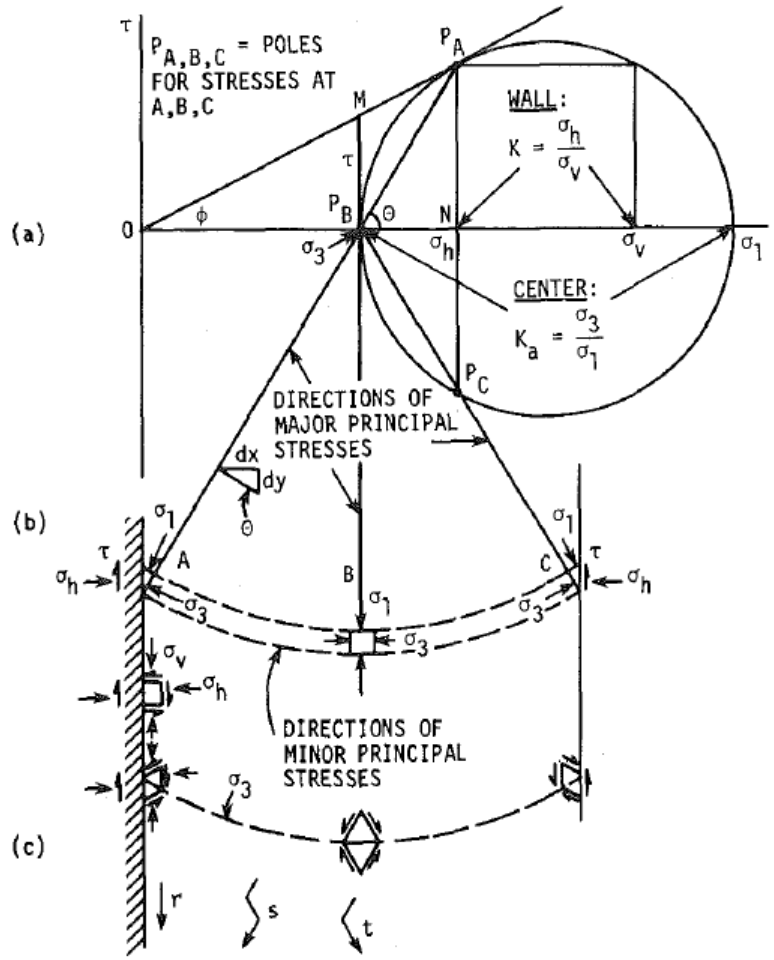

Figure 2.8: Construction of Mohr Circle (a) to show the direction of the major principle stress and the minor principle stress trajectory (b), by Handy (1985). (c) shows the shear line directions.

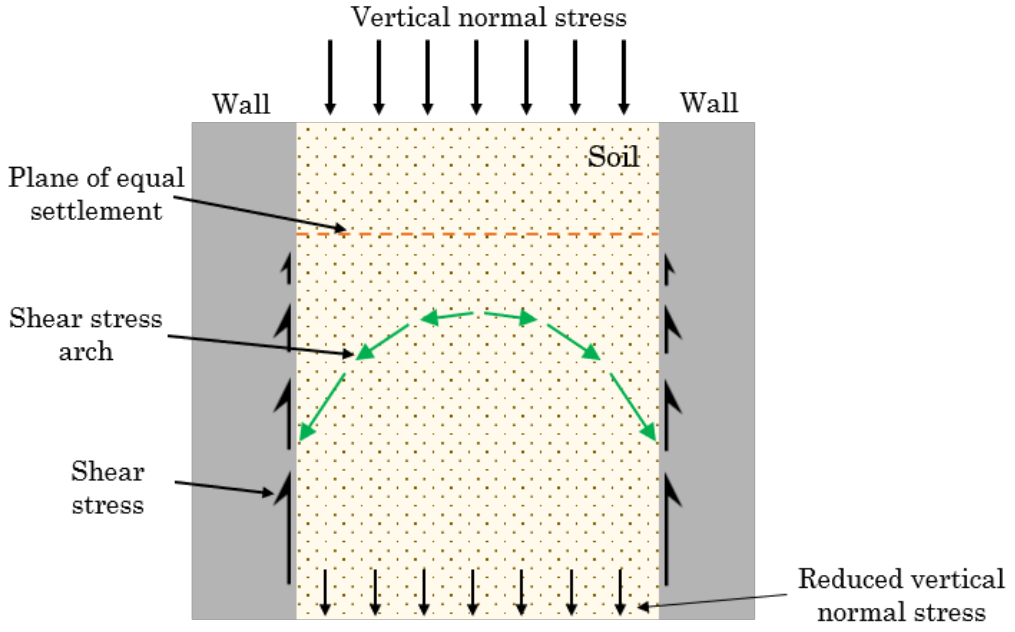

Figure 2.9: Positive arching between vertical walls. The vertical normal stress is redistributed to shear stress beneath the plane of equal settlement.

Much research has been conducted on arching effect during the past century, for a variety of geotechnical engineering problems. Some design approaches utilize arching directly when dimensioning different structures. For instance, the Norwegian Public Road Authorities (NPRA)'s Handbook for Geotechnics in Road Constructions (2014a) employs arching principles to reduce pressures on buried, rigid pipelines and conduits (Figure 2.10). Weight and surcharge from road embankments are transferred to spaced piles by arching mechanisms in the embankment fillings (NPRA, 2014b), as shown in Figure 2.11. However to date, arching effect is not incorporated as a part of rock anchoring design principles.

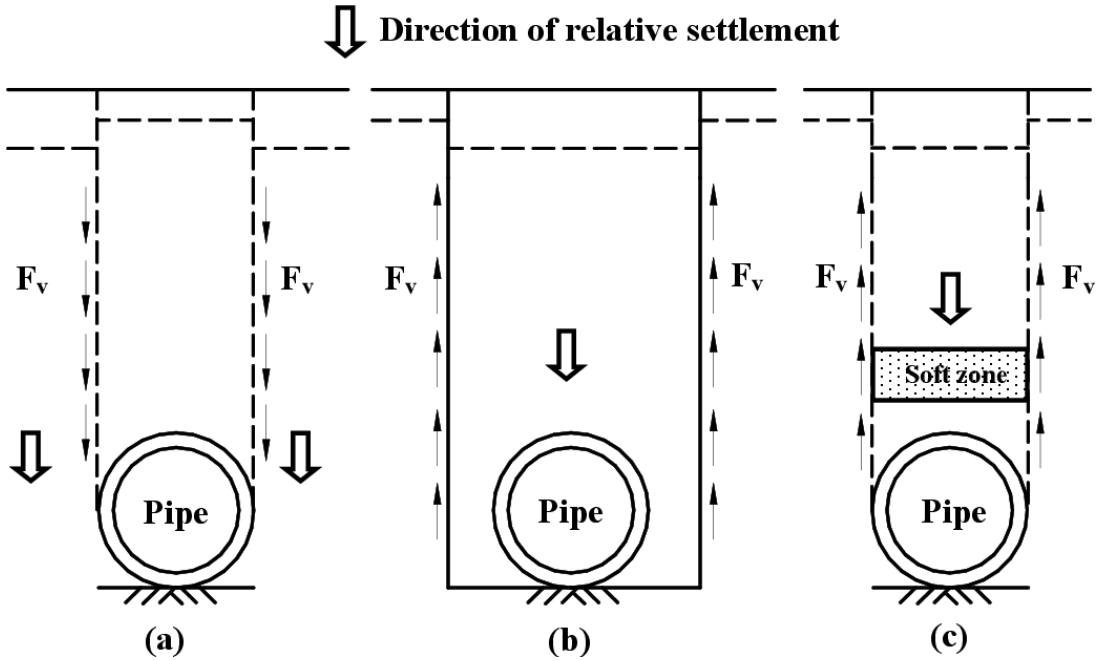

Figure 2.10: In (a), shearing pressure is transferred to a soil body above a rigid pipe due to differential settlement in the adjacent soil, thus increasing the pressure on the pipe due to natural positive arching. This may be reduced or avoided by reversing the relative soil movement by use of the trench method (b) or imperfect trench/ soft filling (c) above the pipe, thereby transferring the shear to the adjacent soil. (F_v denotes the frictional force or shearing stresses) (Kang, 2007).

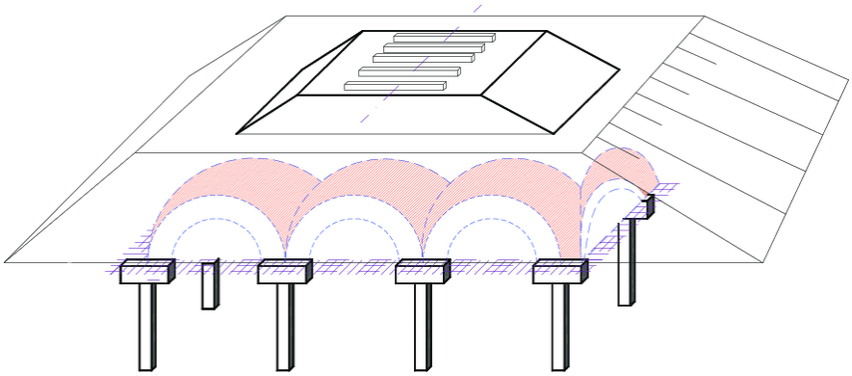

Figure 2.11: Arching in a piled embankment caused by differential settlement of the filling between and above the piles (Drusa et al., 2014)

2.3 Numerical Simulation and the Finite Element Method

A part of this study involves complementing the physical model tests with numerical simulations of the same problem. The software chosen for this purpose is RS2 (version 2019 11.002, Rocscience Inc.). RS2 is a user friendly software which may be applied to a wide variety of 2D geotechnical problems. In this section, the Finite Element Method (FEM) will be explained thoroughly, as it is utilized by RS2 software.

2.3.1 The Finite Element Method

Discretization

Problems which have domains of continuum (on a macroscopic scale) may theoretically require representing the domain by an infinite number of *infinitesimal* elements. Differential equations at the field points describe the system's behaviour, however continuous systems like these have infinite degrees of freedom. To solve such continuous problems by numerical simulation, the problem is reduced through representing the domain by a finite number of individual elements of standard shapes with a fixed number of nodes on the vertices and, optionally, the sides. This process is called *discretization.* The behaviour of the elements may be approximated by simpler mathematical descriptions, as the domain is now reduced to a *discrete* system with finite degrees of freedom. Each element must satisfy the continuity conditions at their interfaces with neighbouring elements, as well as the governing differential equations of the problem. When assuming continuum, points in the problem domain cannot be divided or broken, and all material points remain in the same neighborhood throughout deformation or translation (Jing, 2003).

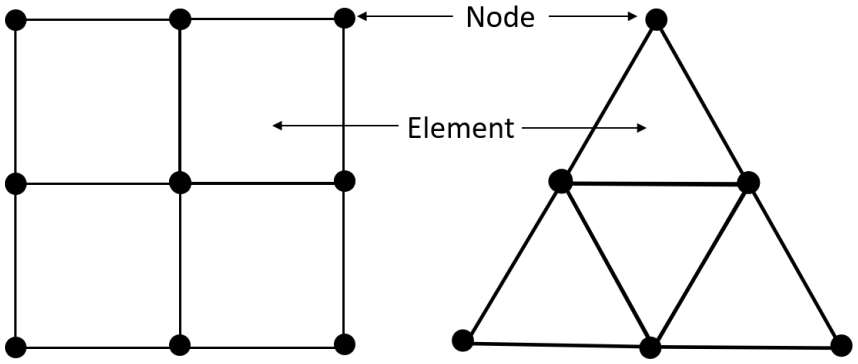

Figure 2.12: Example illustration of quadrilateral and triangular mesh elements with nodes at each vertice.

Achieving Convergence

Static finite element analysis involves obtaining the nodal displacements that occur in response to applied forces on the elements. Through a process of performing multiple iterations of an incremental loading step, the aim is to obtain a system that reaches force *equilibrium.* This means that the internal forces of each element approach the applied loads, until a user-defined tolerance of error is achieved. The system is said to *converge*

toward the solution. Each element is represented by a stiffness matrix that governs the relationship between the applied incremental loading and the incremental displacement at the nodes (Rocscience, a). In RS2, this stiffness matrix is assumed to be global and kept constant throughout all the calculation steps. This assumption is referred to as the *Initial Stiffness Method*, and reduces the computational effort compared to assembling the stiffness matrix at each iteration. However, it requires a greater number of iterations to achieve convergence (Rocscience, b).

Material Models

The magnitude of the internal nodal forces – and thus, strain – in the material is controlled by the applied loads as well as the user defined boundary conditions and material model. Application of an elastic material, that is, a material which follows the Theory of Elasticity, means that the material's stress-strain relationship is linear, and only controlled by the deformation parameters Young's modulus, E, and Poisson's ratio, ν. By definition in RS2, an elastic material has infinite strength and cannot fail. Alternatively, materials may behave plastically, meaning they undergo yielding and irreversible strains when loading exceeds the material's failure criterion. The stress-strain relationship beyond the peak strength is defined by the residual strength and deformation parameters defined from different material models (Rocscience, c). Numerically, this behaviour is simulated through the procedure of applying load increments to an element (achieving convergence for each load step) until the load exceeds the failure criterion of the material. At this point, no further load is absorbed by the element as it deforms, and excess loads are transferred to neighboring elements. This process continues until the loads transferred to the neighboring elements no longer exceed the material's strength, at which point, convergence has been achieved (Hinton and Owen, 1980).

Limitations with FEM Numerical Modeling

Due to it's flexibility in handling material inhomogeneity, non-linear deformability (mainly plasticity), anisotropy, in-situ stresses and complex boundary conditions, the FEM has long been the most popular numerical method in rock mechanics and geotechnical problems in civil engineering (Jing, 2003). However, some limitations do exist: Many are related to the difficulty of establishing the real-life physical properties involved in rock mechanics or geotechnical problems; others are due to the mathematical approximations following the FEM method itself; while some are limitations resulting from the software, hardware or user.

Adequately representing the material, rock or soil may be difficult, as it is related to the extent of investigation, the material's inhomogeneity and continuity, anisotropy, in-situ stresses, and more – not least the classification systems, test methods and/or user's subjective decisions that determine the input parameters. How well these features may be

incorporated into a computer model depends on which physical processes are involved and which modeling technique is applied. Consequently, subjective judgments will affect any models and their solutions (Jing, 2003). These issues concern all numerical modeling of a geotechnical character, not solely the FEM and RS2. Problem-specific limitations will be addressed in the discussions of the numerical models developed for this work, in Section 5.2.

3 Physical Modeling

A two-dimensional small-scale physical model test for "pull-out" of an anchor socket buried in frictional and low-cohesive materials was designed and constructed to study how failure occurs within the material specimens; particularly which shape the failure attains and how it propagates throughout the material. Finally, the model will be used to acquire experimental data to calibrate and validate numerical models of the same problems, as described in Section 4.1.

3.1 Concept, Design and Construction

The desire to create a small-scale physical model arose as a result of considerable delays to the construction of the full-scale ROCARC test rig during the spring of 2020. Whereas the full-scale test rig is an advanced apparatus specifically designed for testing with concrete bricks in varying patterns, the small-scale model was intended for use with frictional and low-cohesive material. Its purpose was to replicate the ROCARC test rig and facilitate studies of a similar nature, though at a greatly simplified scope, lowered cost and scale. This way, some helpful insight may be obtained while awaiting finalization of the full-scale test rig. With this as the background for the design/model layout, the model was to serve the following requirements and desires:

- The model should effectively simulate overstressing of an anchor
- It must be suitable for testing different types of materials, herein frictional and low-cohesive
- It must allow for observation of failure form and development
- It should be of a small scale
- It should be operable by one person
- It should have overall low costs and short construction time (preferably a few weeks)

Initial design concepts consisted of a 60 cm $\times$ 10 cm $\times$ 40 cm transparent test chamber with a small block inside, to represent an anchor socket, which somehow must be pushed or pulled upward. The model was found to be simplest if designed to have the anchor "socket" pushed up from the bottom, rather than pulled upward by a jack or pulley from the top. This decision also enabled use of equipment which already existed in the combined laboratories of the Department of Geoscience and Petroleum at NTNU (IGP-NTNU) and SINTEF, herein a manual hydraulic jack, a load cell and an extensometer. A digital camera and PC were also available for monitorization. The mechanism chosen for displacing/loading the socket governed much of the design layout. Jacking the socket from the bottom required a rigid base frame to resist uplift of the entire construction. The materials must also be stiff to avoid deformation, including the PVC glass of the test

chamber, which was decided to be 1 cm thick. Initial design involved use of timber to create a solid frame and base. This was changed to steel at the request of the contractors at the workshop, and was possible as the difference in material costs was minimal.

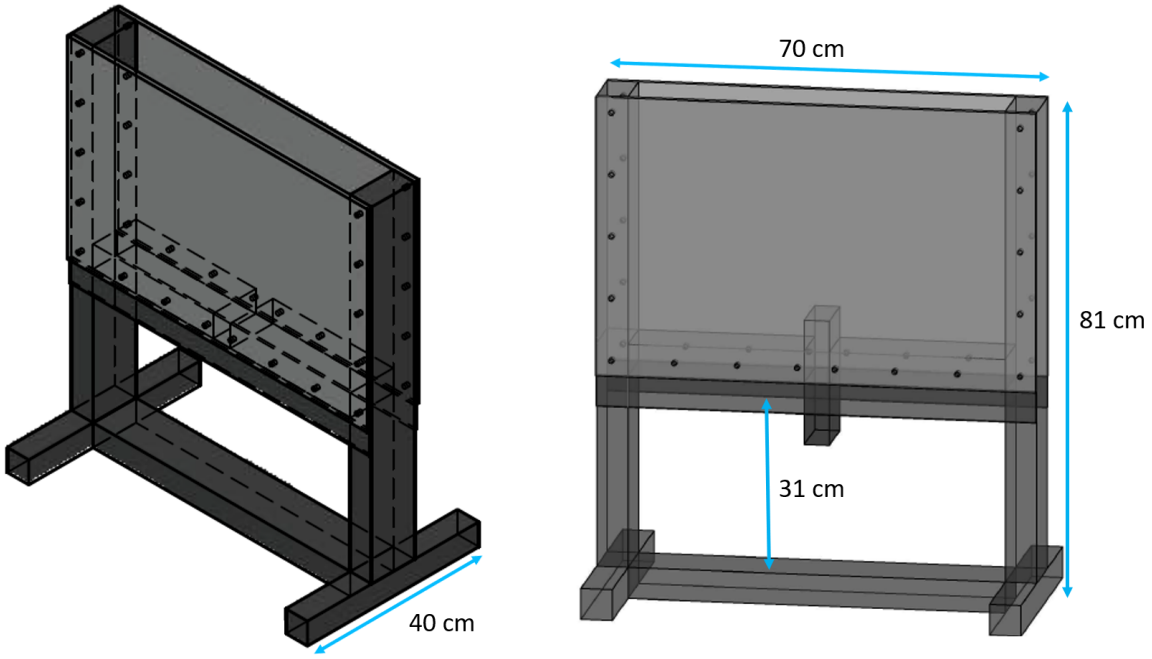

Figure 3.1: Illustration of the steel frame model design. The internal dimensions of the test chamber are 60 cm × 10 cm × 40 cm (Length×Width×Height).

The block that simulates the socket must fulfill two requirements: It must be stiff, and it must have rough surfaces in contact with the test material – rough enough to fully grip and mobilize it as the socket is raised. This was achieved by furrowing horizontal, semi-circular grooves into an engineering thermoplastic, Polyoxymethylene (POM), block. The grooves have a radius of 3.5 mm, and are spaced 5.5 mm apart. The block fits tightly between the PVC glass sheets and a guide slot in the steel frame, ensuring its straight path and preventing material from emptying.

To mimic the the situation of a socket in an empty borehole, its vertical pathway must remain free of material. Mobilization of the material should only be caused by the rough faces of the socket, not from lifting by the top face. To ensure this and prevent loose material from filling the pathway/"borehole", thus burying the socket, a smooth POM extension is added above the socket block. The exact length of the rough and smooth areas were somewhat arbitrarily established, as the block was furrowed *prior to* modifications which later became necessary to fit the load cell and extensometer to the jack. Additionally, the smooth extension was attached separately, and the remaining POM block available for this was only 20 cm long. Ultimately, the rough surface protrudes 16 cm into the test chamber, while the upper 20 cm are smooth. Figure 3.3 shows the final "anchor block".

In the end, the model underwent many tweaks and improvements from its initial design, until the final assembly was completed in medio December 2020. The setup is shown in

Figure 3.4, below.

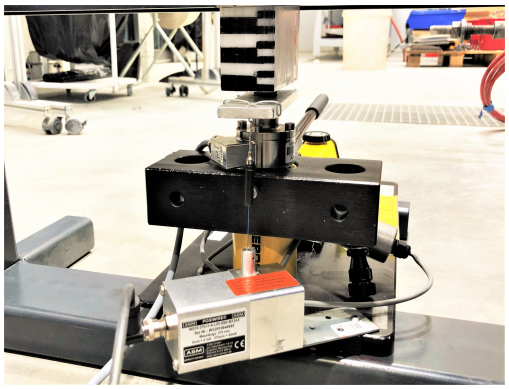

Figure 3.2: Extensometer and load cell setup.

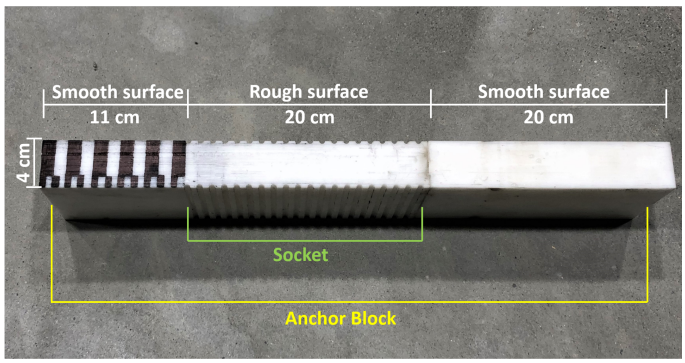

Figure 3.3: POM block (Anchor block).

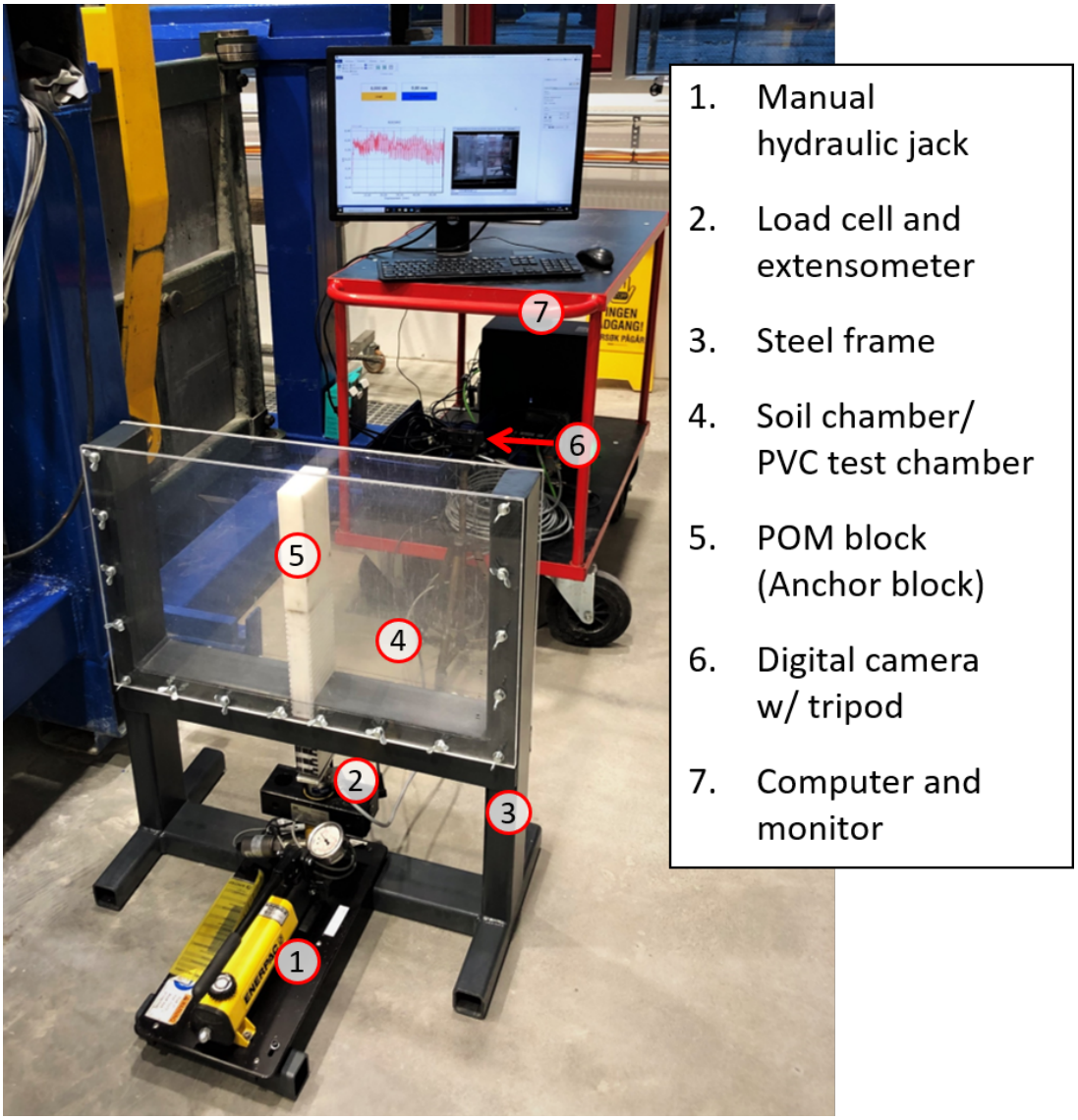

Figure 3.4: Final model and equipment setup.

3.2 Test Materials

The model was designed to accommodate different frictional soils and low-cohesive test materials. The soils were obtained from waste material at IGP's own mineral processing laboratory, which consisted of homogeneous, crushed eclogite. This was also used to create a low-cohesive concrete material.

3.2.1 Preparation of the Frictional Soils

The waste material was available in two fractions: 0-3 mm and 0-8 mm. These were dried and sieved to achieve desired particle sizes. Water was added when needed to reach specific moisture contents. This way, four different frictional test soils were created, presented in Table 1. Grain Size Distribution (GSD) analysis and Direct Shear Tests (DST) were performed to determine additional geotechnical properties of each soil.

Grain Size Distribution by Sieve Analysis
Sieve analysis' were performed on the 0-3 mm and 0.5-6.3 mm crushed eclogite. The procedure follows the standard given by the Norwegian Public Road Authorities (2015), using wire mesh sieves (0.063; 0.125; 0.250; 0.500; 1.00 and 2.00 mm nominal aperture (NA)) for grains smaller than 4 mm, and square hole perforated plate sieves (4.00; 5.00 and 8.00 mm NA) for larger material. Note that 5.00 mm is not a NA used according to the standard, but was added to provide more detail to the analysis of the 0.5-6.3 mm soil. The Grain Size Distribution (GSD) is shown in figures 3.5 and 3.6 as the cumulative weight percentage passing through each sieve.

From a GSD, it is possible to determine D_{60} and D_{10}, i.e., the diameter at which 60 % and 10 % of the material passes through the sieves, respectively. From this, the Coefficient of Uniformity, C_u, may be determined as:

$$C_u = \frac{D_{60}}{D_{10}} \tag{7}$$

According to the NPRA (1980), a soil is considered *well graded* if $C_u > 10$, and *uniformly graded* if $C_u < 5$ (these definitions vary somewhat between countries and standards). Thus, the 0-3 mm soil is well graded and the 0.5-6.3 mm soil is uniformly graded. The GSD's also show that the 0-3 mm soil in fact contains some grains larger than 3 mm, and has a high content of fines, i.e. 15 % <0.063 mm.

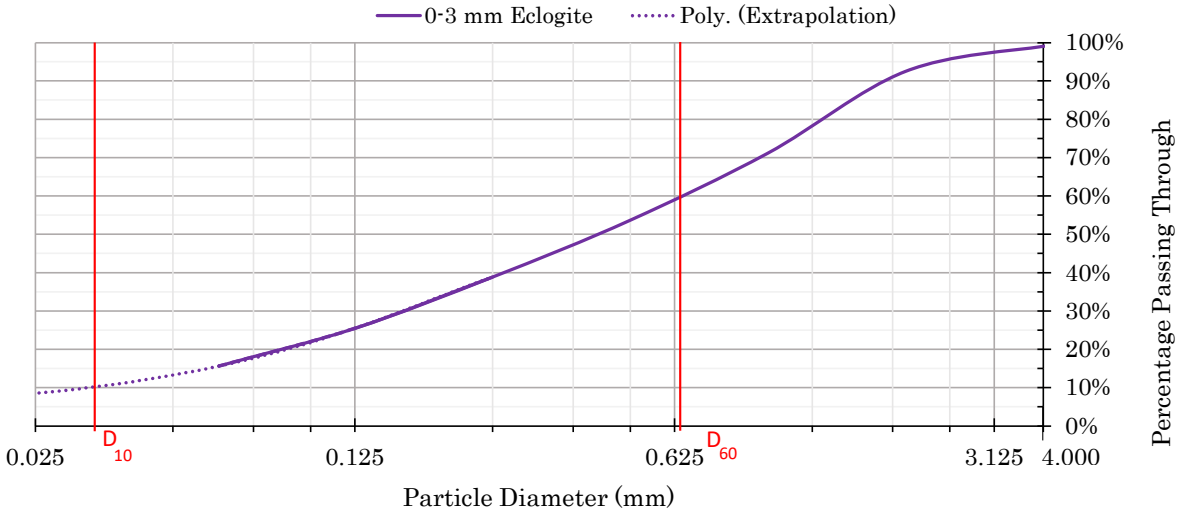

Figure 3.5: Grain Size Distribution for 0-3 mm eclogite.

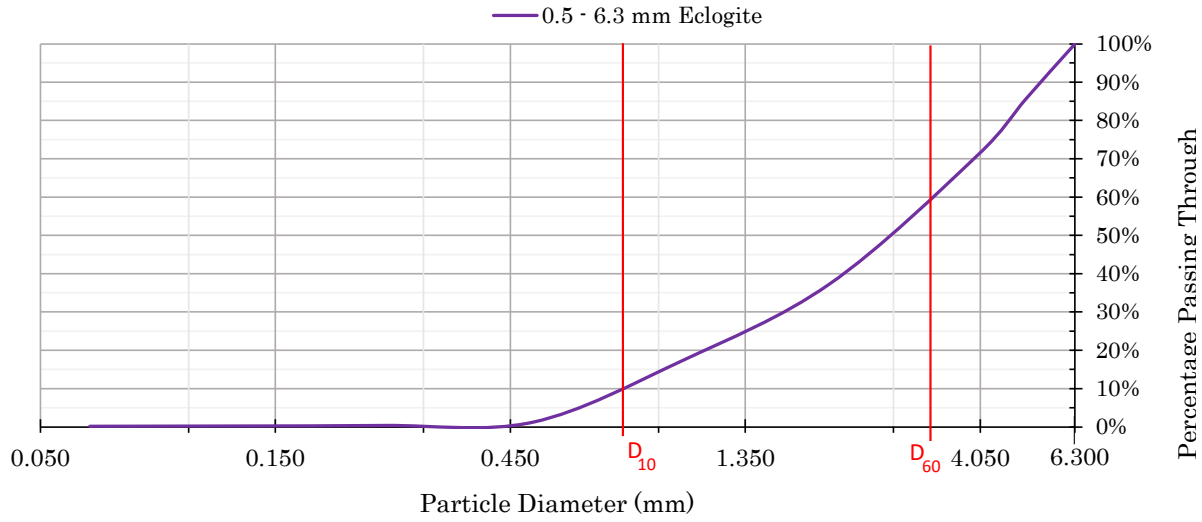

Figure 3.6: Grain Size Distribution for 0.5-6.3 mm eclogite.

Determining the Soil's Friction Angle Through Direct Shear Tests

Direct shear tests were performed at the IGP-NTNU Rock Mechanics Laboratory, to determine the friction angle of each soil type. During the direct shear test, a soil specimen is filled and into two stacked box frames, one of which is fixed while the other is free to move horizontally. A constant normal stress, σ_n, is applied perpendicularly to the lid of the upper box, before an increasing shear stress is applied to the free-moving box, perpendicular to the direction of the normal stress (See Figure 3.7). The shear stress, horizontal and vertical displacements are recorded continuously. Equipment and procedures may vary between laboratories. The test procedure at IGP-NTNU is thoroughly described by Opsal (2017, pp. 150-152). Specifically for this work, each specimen was compacted in the frames and applied a consolidating normal stress up to the value applied during the tests. Each

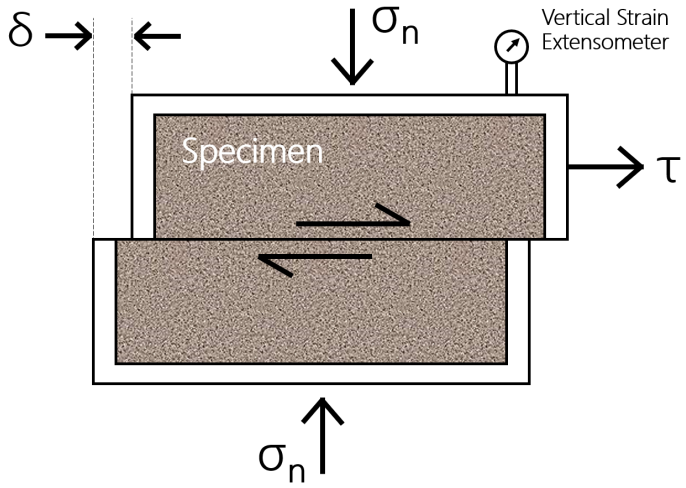

Figure 3.7: A simple illustration showing the principles of the Direct Shear Test.

soil type was tested at 100 kPa, 200 kPa and 300 kPa normal loading, with a shear rate of 2 mm/min until maximum 40 mm displacement was reached. The result from DST on one of the test materials (A.1, see Table 1) is shown in Figure 3.8. By performing multiple tests and increasing the normal stress each run, one obtains the maximum shear stress values, τ_{max}, as a function of the applied normal stress. The inverse tangent of its slope gives the peak friction angle, φ_{peak}, as according to Mohr-Coulomb theory (Equation 6). Equally, one may obtain the *critical state friction angle*, φ_{cr}, by plotting the near-constant shear stress values that the soil approaches post-peak. For soil samples that do not display a peak shear stress value, the curve approaches the constant critical shear stress value. Figure 3.9 shows the Mohr-Coulomb fit curves obtained from the three tests on material A.1, a dry 0-3 mm, crushed eclogite.

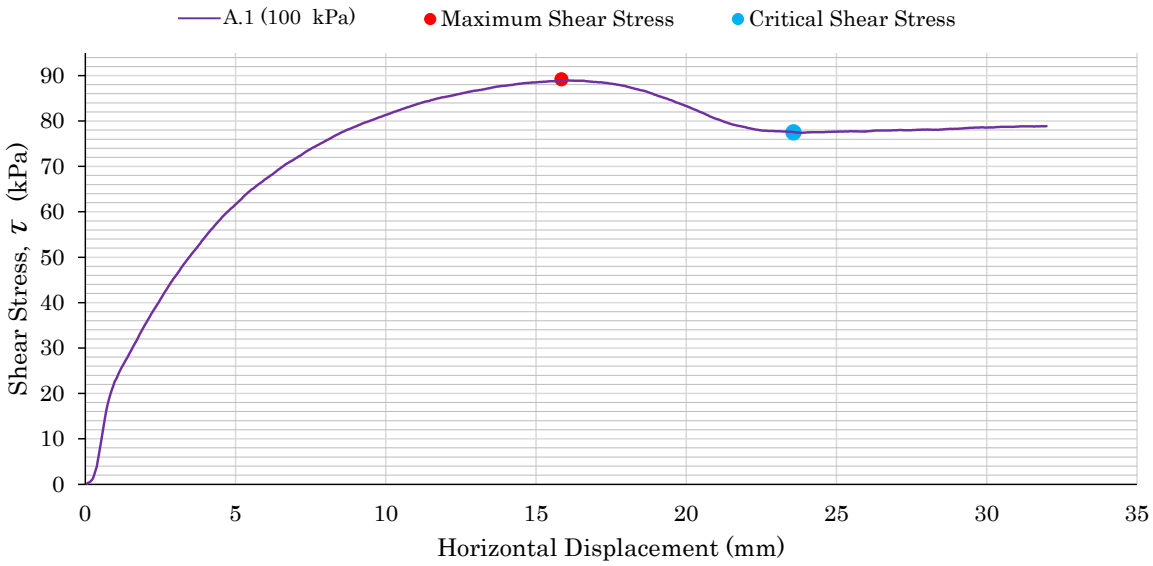

Figure 3.8: Direct Shear Test result on material A.1 at 100 kPa normal loading.

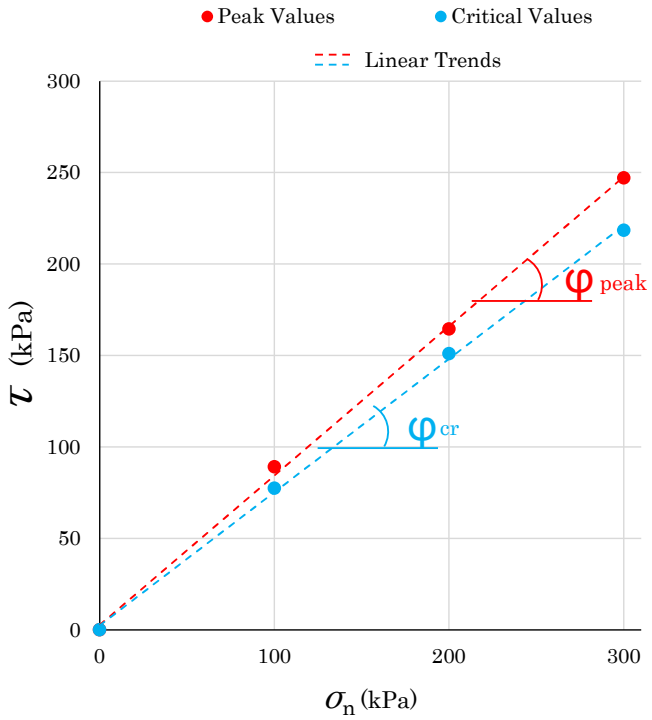

Figure 3.9: Mohr-Coulomb curve fit to results from the direct shear tests, material A.1.

Table 1 shows different geotechnical properties obtained for the four different soil types.

Table 1: Physical and geotechnical properties of the frictional test material.

		Eclogite 0-3 mm		Eclogite 0.5-6.3 mm	
Parameter	**Name:**	**A.1**	**A.2**	**B.1**	**B.2**
Moisture Content, w		Dry	7 %	Dry	5 %
Average Loose Density, ρ_L (kg/l)		1.8	1.5	1.8	1.6
Average Compacted Density, ρ_C (kg/l)		2.1	2.3	2.1	2.1
Coefficient of Uniformity, C_u		22		4.5	
Peak Friction Angle φ_{peak} (°) *		39	35	43	38
Critical State Friction Angle φ_{cr} (°) * †		36	-	38	-

*From moderately compacted specimens

† φ_{cr} equals the residual friction angle post-peak for tests with a peak value

3.2.2 Creating a Cohesive "Weak Rock" Material

To represent a weak rock, a small amount of cement was mixed with the 0-3 mm eclogite. The cement is added to create cohesive bonds between the grains. The water-soil-cement mixture ratio was determined by creating cup-sized samples of different mixtures of water, soil and cement, and different mixing techniques. When hardened, the characteristics of each sample was examined to find a blend that created a material which would not crumble or compress like a soil, yet could be easily broken by hand. Samples which fulfilled

these requirements were up-scaled to a larger mold and re-examined after hardening. The final selected mixture for material C.1 is given in Table 2. After performing a test with material C.1, following the approach described in Section 3.3.3, it was decided to create an even weaker material by reducing the amount of cement. The mixture for this material, named C.2, is also given in Table 2

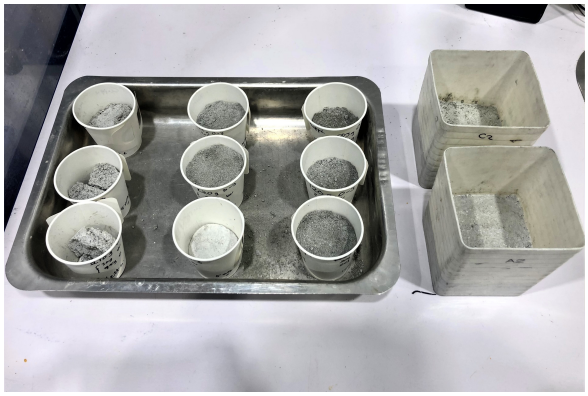

Figure 3.10: Water-soil-cement samples.

Figure 3.11: Assessing the sample's cohesive strength by hand.

Table 2: Mixture ratios and properties of materials C.1 and C.2

Description	**Test Material**	
	C.1	**C.2**
Material	*Contents (wt%)*	
Sand, 0-3 mm	84	86
Water (w)	12	12
Cement (c)	4	2
w/c Ratio	4	6

Note: Water and cement were combined before adding the soil

Determining the Strength by Uniaxial Compression Tests

To gain better knowledge of the strength of the cohesive material, core samples were created to be used in Uniaxial Compressive Strength tests (UCS-tests), following the standard procedure by ISRM (1979). During a UCS-test, a core sample is uniaxially loaded until the sample breaks under the load. This load equals the maximum compression the sample can bear without confinement.

To create samples for the UCS-test, a stiff plastic pipe of 53 mm inner diameter was sawed into six pieces, roughly 140 mm long, which were sawed into half-cylinders. The half-cylinders were paired correctly and carefully duct-taped together to form cylinders molds, once again (Figure 3.12). One end of each cylinder was then covered with plastic wrap, secured by rubber bands, before the cylinder was lightly greased with form oil

internally. The wet mixes of C.1 and C.2 were cast into three cylinders each, compacting it lightly during filling to minimize air pockets.

The cores were left to harden for three days, before they were cut to create plane ends. It was found that cutting gave smoother ends than surface grinding, as grinding had an abrasive effect on the cement but left the harder mineral grains intact. Therefore the cores were not surface ground, which may cause the ends to depart from perpendicularity to the long-axis by more than what is required by the ISRM (1979) standard. Due to the low strength of the material, this was considered to be of less importance. After cutting, the plastic molds were opened and the cores carefully removed. Each core sample was marked and wrapped in plastic film before running the test.

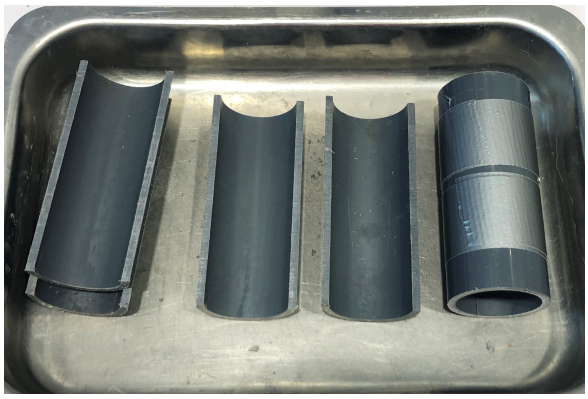

Figure 3.12: Preparation of core molds.

Figure 3.13: Core samples from molds (C.2).

Table 3: Properties of the hardened concrete materials, C.1 and C.2

Property	**Material**	
	C.1	**C.2**
Avg. UCS (MPa)	0.660	0.473
Standard Deviation (Mpa)	0.248	0.100
Avg. Density (kg/dm^3)	2.26	2.33

A UCS value between 0.25 - 1 MPa is considered an *extremely low strength rock* by ISRM (1978), border-lining the definition of a hard soil. Thus, the results prove that a desired strength was achieved for materials C.1 and C.2.

3.3 Testing Approach

The anchor block is to be pushed upward by the hydraulic jack, thus simulating the over-stressing of a buried anchor. Displacements and loads during pushing are measured by an extensometer and load cell, installed on the jack and block, as seen in Figure 3.2.

3.3.1 Calibration of the Apparatus

The average frictional force arising from the block-steel and block-PVC glass interface is determined by conducting a test with an empty test chamber prior to the material experiments. An empty chamber test is also repeated after the final material test, to control whether the system's internal friction has changed during use. Figure 3.14 shows the results of the two tests. Prior, the value ranges within approximately 0.35 kN to 0.40 kN past the first 1 mm of displacement. After, it varies between approximately 0.27 kN to 0.33 kN beyond 1 mm displacement. The reduction likely results from paint on the steel slot being worn off, and slight bulging of the PVC glass.

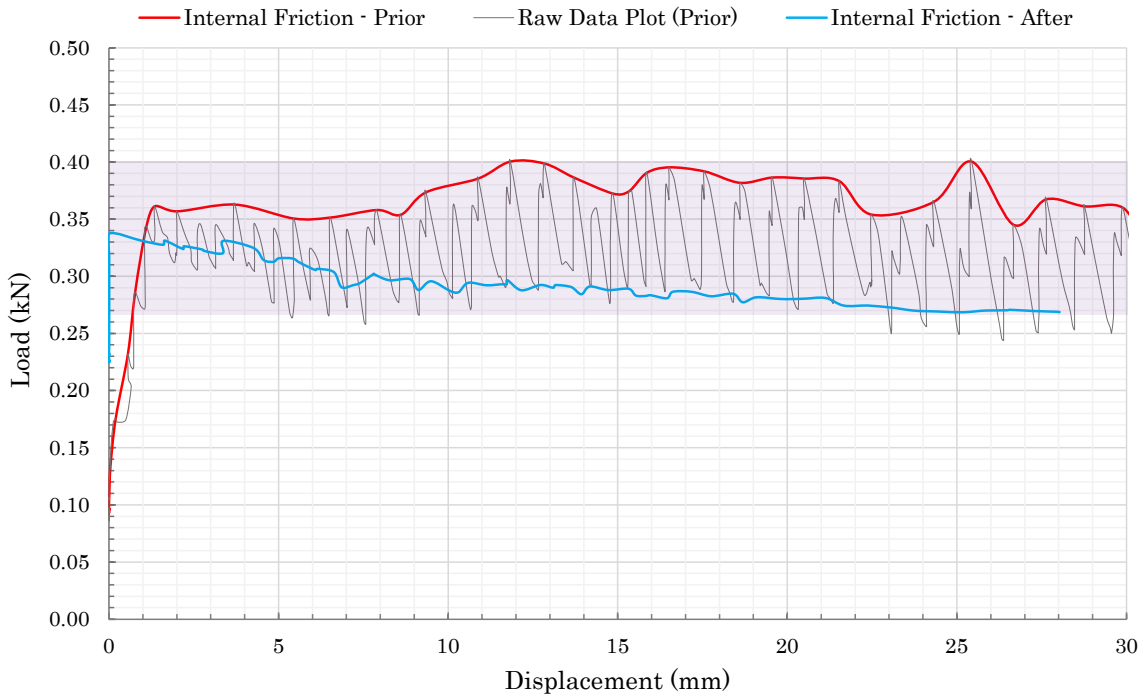

Figure 3.14: Load-displacement plot from an empty model tests.

Note that the Raw Data Plot (Prior) shows the values as recorded by the load cell on the hydraulic jack. The hydraulic jack is manually pumped by raising and lowering a lever. The load fluctuation is the result of very minor movements and pressure reduction in the hydraulic jack's internal system when the lever is raised and the pumping abruptly stops. This phenomenon causes the local minimas in the Raw Data Plot (Prior), which do not represent the response from the actual jacking action. Therefore, the local minimas are filtered out, providing a more correct and presentable curve of the load-displacement relationship.

Once the system's internal friction has been determined, the chamber is filled with a single type of test material. The procedure varies between the frictional and cohesive material:

3.3.2 Procedure for the Frictional Materials

The loose frictional material is added to the test chamber in even layers requiring on average 1.4-1.5 l per added layer. Material A.2 required 1.5-1.6 l per layer. It was found necessary to compact the material to induce horizontal stresses on the socket surface, thus increasing the grip of the socket. Compaction is done by use of a fitted wood plank and a wood post, as shown in Figure 3.16. The post is used to pound the plank at total of 60 times per layer, which distributes the force evenly to the material. Compaction caused the PVC glass to bulge outwards; therefore a wood clamp was applied during filling/compaction to limit the bulging (Figure 3.16). Note that this was done for all frictional material tests *except* for *Test 1 on material A.1.*

On each compacted layer, an even line of a contrasting, white mineral is placed near the PVC glass, as shown in Figure 3.15. This allows for easy visual observation of displacements in the soil body as the experiment commences. When the soil depth reaches approximately 30 cm in the container, the experiment may begin (Figure 3.17). The jack is manually pumped, thus pushing the block into the material. The displacement and load is registered, while the developing failure in the material is recorded by a video camera. The video recordings are synchronized to the displacement and load recordings, providing easy post-analysis. The block is displaced until it slips through the material, or until the jack reaches its maximum extension (50 mm). The entire procedure is repeated twice per material.

Figure 3.15: Adding of contrast mineral.

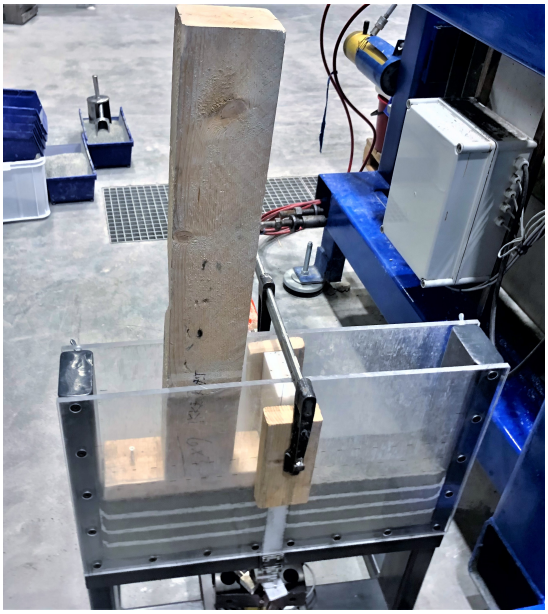

Figure 3.16: Compacting tools.

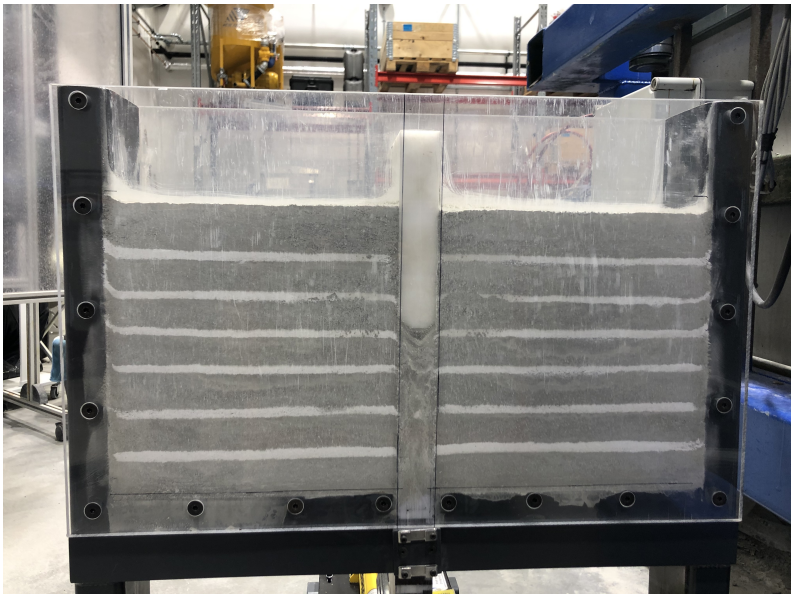

Figure 3.17: Test model filled with compacted test material (dry Eclogite, 0-3 mm) and contrasting lines, pre experiment.

3.3.3 Procedure for the Cohesive Materials

Test C.1: 0.3 mm eclogite containing 4 % cement

First, the hydraulic jack, extensometer and load cell are covered in plastic wrap for protection from any liquid cement which may leak from the test chamber. The anchor block and PVC glass are greased with form oil to prevent the cement from adhering to the surfaces after hardening. Then, loose material, water and cement are combined to create approximately 18 l of material C.1, following the ratios given in Table 2. The wet mixture is added to the test chamber and moderately compacted by hand to reduce the presence of large air pockets.

After filling the chamber up to approximately 30 cm depth, the model is left for 3 days to allow the material to harden sufficiently. On day 2, the PVC glass was loosened slightly from the material to allow excess moisture evaporate and to ensure that the material is detached from the surfaces. After fully hardening, the PVC glass is reassembled as normal, and the experiment proceeds as described for the frictional materials.

During the experiment on C.1, failure did not occur through the material, but as slipping between the material and steel walls. To prevent further slipping in the model, wood blocks were clamped onto the top corners of the material block, before proceeding as usual.

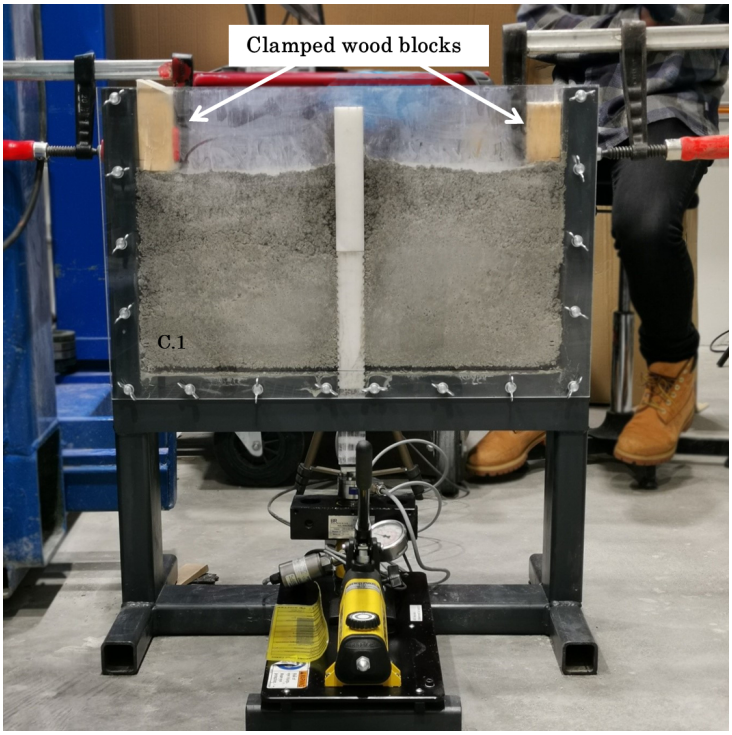

Figure 3.18: Photo showing the clamped wood blocks on the model, for preventing uplift of the material.

Test C.2: 0-3 mm eclogite containing 2 % cement

Following experiences from the test on material C.1, it was decided to perform some modifications to the model, in addition to creating the weaker material, C.2. The modifications included increasing the friction between the material and vertical steel walls, and reducing the material depth. The steel side walls were therefore clad in a coarse sandpaper, using duct tape and by clamping the sandpaper securely between the steel and PVC glass. This effectively created a coarser surface for the material to interact with.

The hydraulic jack, extensometer and load cell are covered in plastic wrap for protection from any liquid cement that may leak from the test chamber. Tape is used to cover the transitions and gaps between the steel and PVC. The PVC glass and anchor block are greased in form oil. Material C.2 is mixed and added to the test chamber, regularly compacting by hand, as for C.1. The chamber is filled to reach only 20 cm depth for this experiment.

The model is left to harden for 3 days. On day 2, the PVC glass was loosened slightly from the material to allow excess moisture evaporate and to ensure that the material is detached from the PVC glass, as done for C.1. After fully hardening, the PVC glass is reassembled as normal, and the experiment proceeds as previously described.

Figure 3.19: Sandpaper on frame.

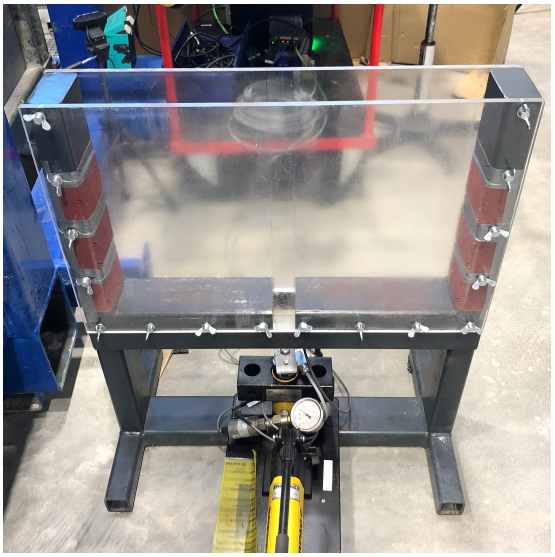

Figure 3.20: Modified model.

3.4 Results

3.4.1 Frictional Materials

Material A.1: 0-3 mm Dry Eclogite

Two tests were run on separate samples of material A.1, the dry 0-3 mm eclogite. Figure 3.21 shows the load-displacement plot from test 1 and 2:

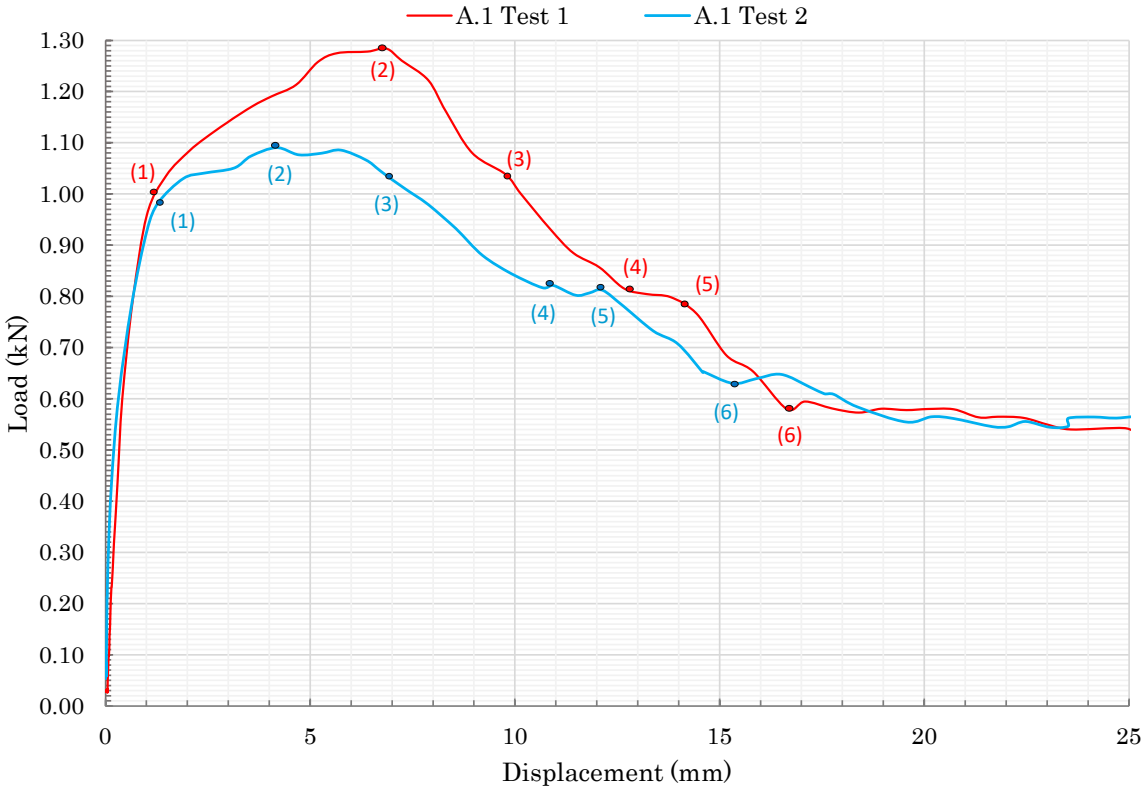

Figure 3.21: Load-Displacement plot for material A.1

Phase 0-1: Up until approximately 0.95 to 1.00 kN loading, the material's response is nearly linear elastic, and roughly equal for the two curves. Load increases abruptly up until a small displacement of only 1 mm.

During **Phase 1-2**, the slopes of the curves begin to decrease, though remain positive. The material continues to absorb loads but enters an initial phase of failure. From Point 1, movement becomes more visible. It is even possible to observe a faint V-shape begin to develop from a point near the base of the anchor block. It becomes more distinct as the displacement continues, though no definite separation has begun. Point 2 denotes the peak load registered during the tests.

Phase 2-3 is characterized by a more visible V-shape mobilizing in the frictional material. The the resistance starts to reduce for both cases. In Test 1, the angle at which the V-shape continues to develop appears to decrease post peak.

Phase 3-4, At point 3, a separation between the V-shaped body and the underlying material becomes visible as the failure planes clearly begin to form. They initiate at a point on the rough socket surface, roughly 3 cm from the base, and gradually propagate upward through the specimen at an inclination. For Test 1, this angle is clearly narrower than the initial mobilized mass.

With further displacement, the failure plane continues to develop toward the surface, thus creating a delimited V-shaped body at Point 4. This is lifted during **Phase 4-5**, which is seen from the 2 mm displacement with nearly constant resistances of 0.82 - 0.80 kN in both Test 1 and Test 2.

In Test 1, the angle of the V-shape widens somewhat towards the surface, giving a slight curve to the shape. It is now clearly separated from the underlying material. The case is different for Test 2, in which material continuously loosens from the uplifted failure body and falls down on the underlying material during this phase. Visually, this causes the angle the uplifted body to appear steeper, however, the video recording captures the actual failure angle.

In **Phase 5-6** the failure bodies on each side of the anchor are either gradually or more abruptly released from the anchor block. The load reduction corresponds roughly to the reduced mass being held up by the anchor. Beyond point (6), the block is slipping through the material.

Note: Compaction caused outward bulging of the PVC glass, which was attempted overcome by use of a large clamp during filling of the test chamber. This was done for all of the tests except for the first test on material A.1. Hence for this test, the block-PVC friction may differ – even increasing significantly – from the readings without material, as grains became lodged and compacted between the PVC glass and block.

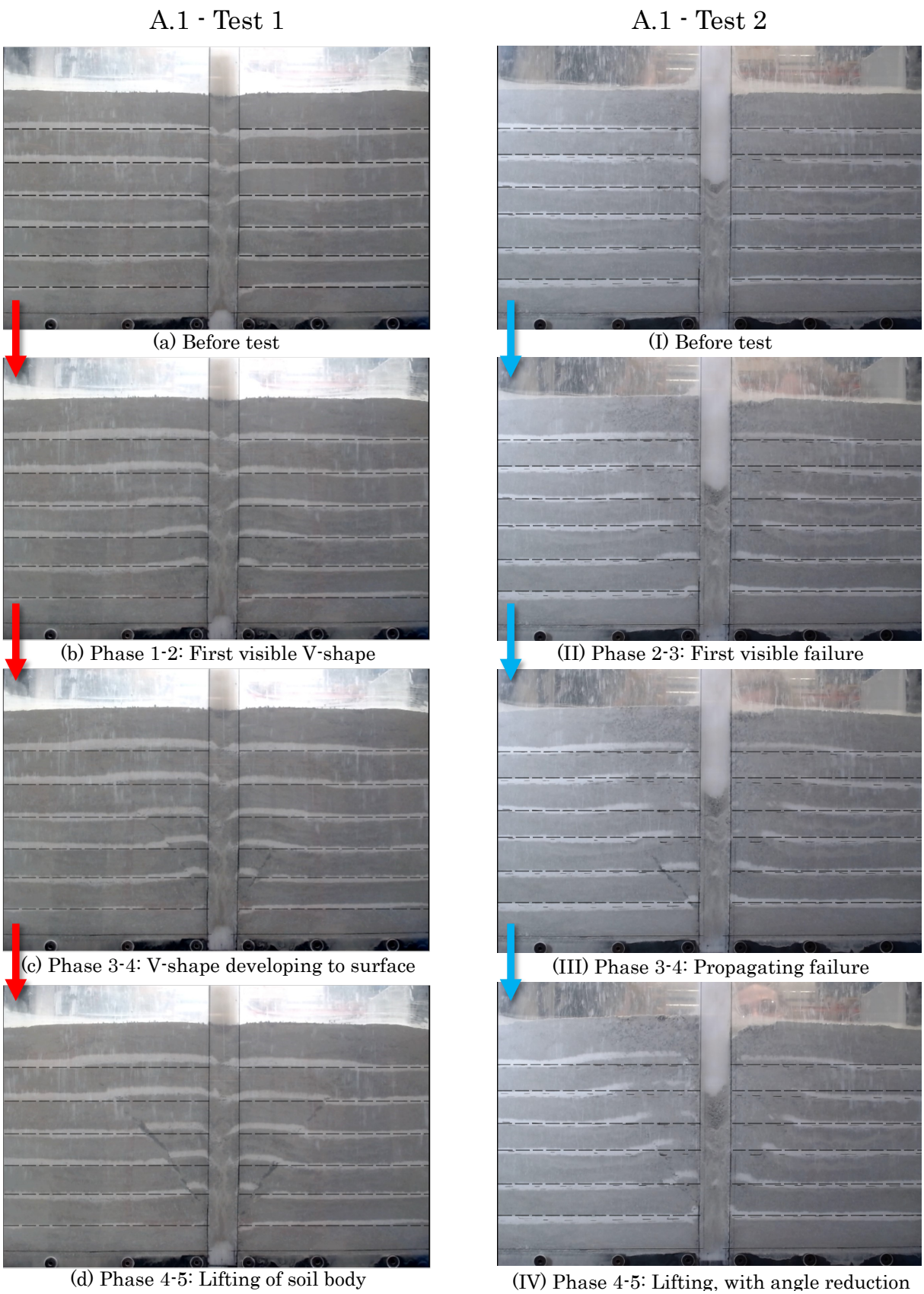

Figure 3.22: Photos from Test 1 (left) and Test 2 (right) with Material A.1: 0-3 mm dry eclogite. The phases correspond to the markings on the plots in Figure 3.21.

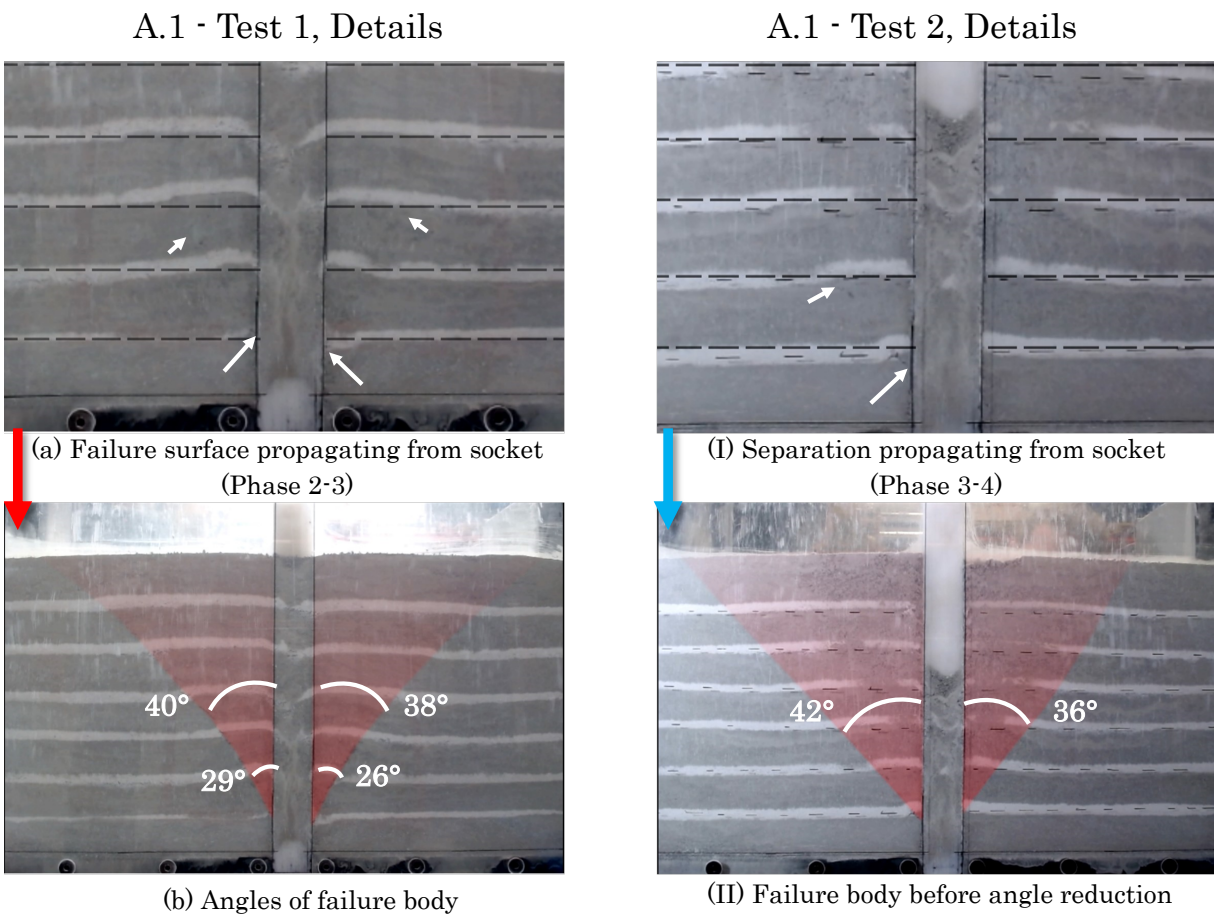

Figure 3.23: Detailed images from tests on material A.1.

Images (a) and (I) in Figure 3.23 show details of the initiation points and beginning failure propagation in test 1 and 2. The failure surfaces create a V-shaped body, highlighted in red in (b) and (II), Figure 3.23. As shown, the angles may vary at different points on the failure surface, and may also change during lifting and further development of the failure body.

Material A.2: 0-3 mm Moist Eclogite

Two tests were run on separate samples of material A.2: 0-3 mm moist eclogite. Figure 3.24 shows the load-displacement plot from test 1 and 2:

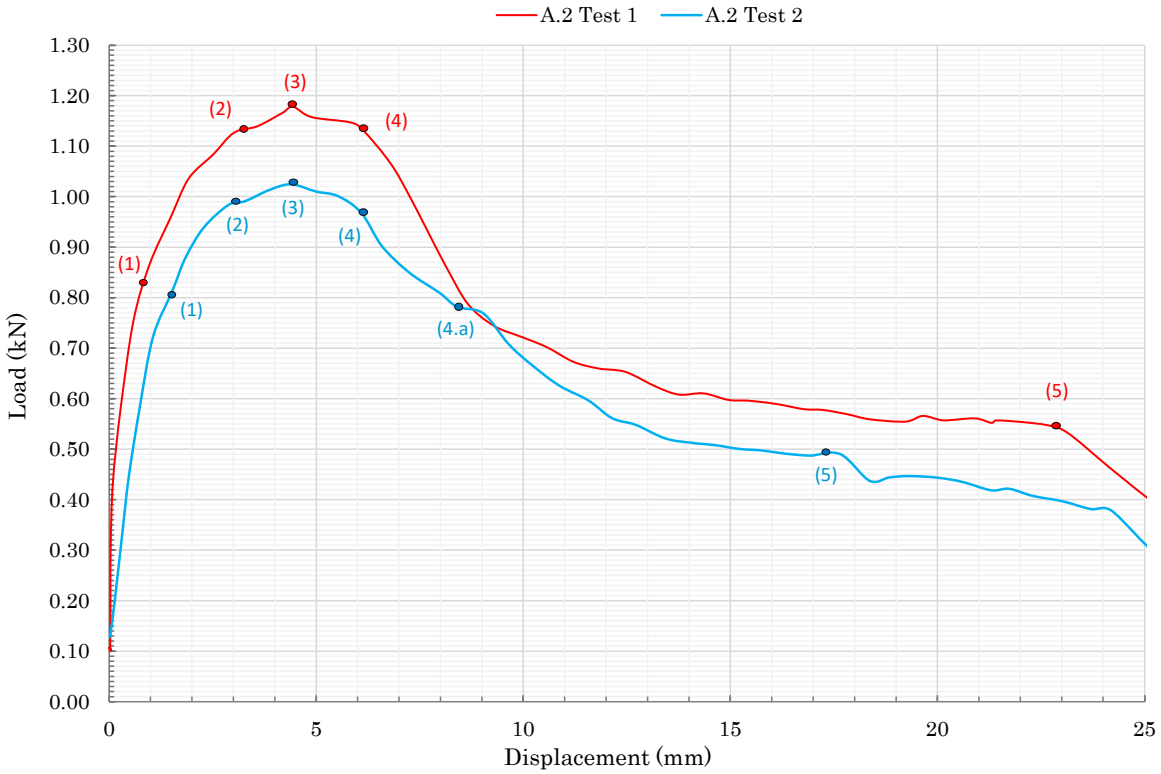

Figure 3.24: Load-Displacement plot for material A.2.

Phase 0-1 represents a nearly linear-elastic response from the model, until roughly 0.75 kN for Test 1 and 0.70 kN for Test 2. The slope decreases slightly when approaching, Point 1. Movement is barely visible. At Point 1, a slight V-shape begins to form in both samples. The amount of movement increases visibly in the material during **Phase 1-2**. At Point 2, the first distinct failure planes may be observed.

The V-shape continues to propagate from the points of initiation towards the surface at an inclination during **Phase 2-4**, with 3 marking the peak load. At Point 4, failure appears to have reached the surface, as minor material separations become visible and the surface noticeably rises.

In **Phase 4-5**, the V-shaped failure body continues to develop, breaking remaining material bridges and reducing contact between the moving pullout body and underlying material. The resistance gradually reduces. Special for Test 2, is that at Point 4.a the angle of the failure body suddenly begins to narrow on the right hand side, and a new failure surface emerges. Shortly after, this final failure form continues to develop and lift, while the resistance continues to drop. As the curve flattens out, the resistance is mostly caused by the weight of the pullout body. This drops beyond point 5, as loose material begins to slip from the surface of the anchor.

A.2 - Test 1

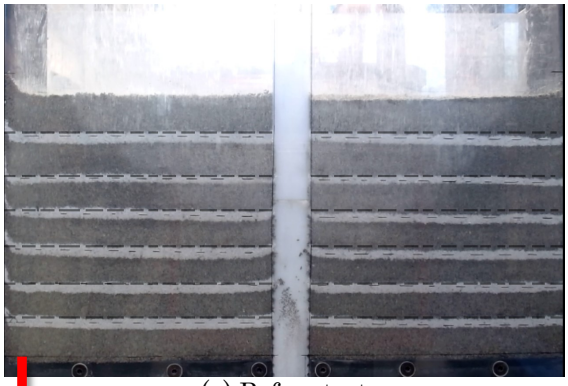

(a) Before test

(b) Point 2: First visible failure plane

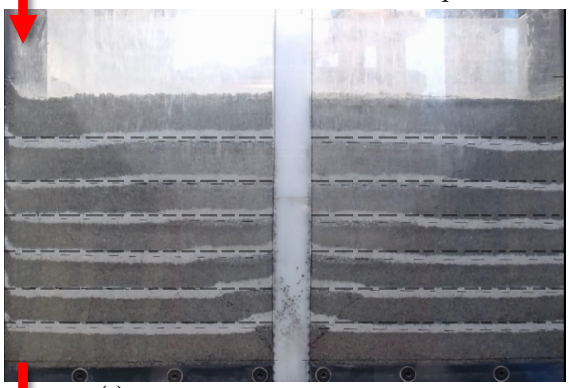

(c) Point 4: Developed to surface

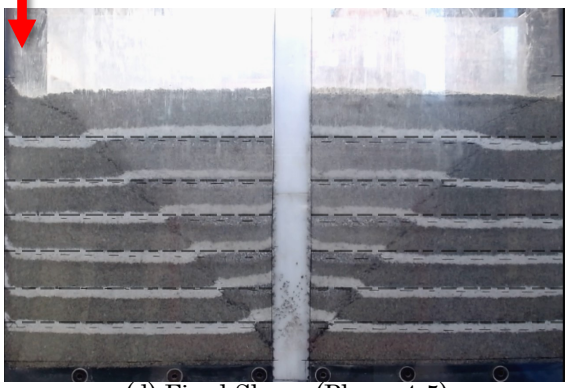

(d) Final Shape (Phase 4-5)

A.2 - Test 2

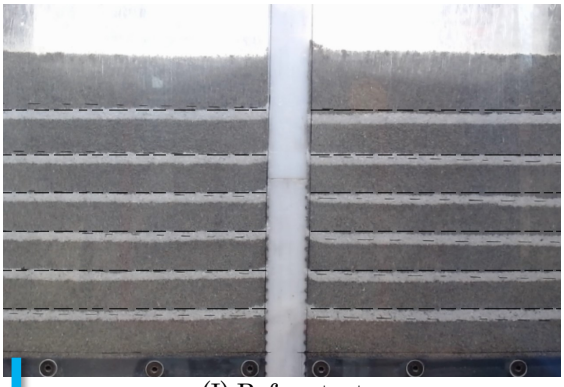

(I) Before test

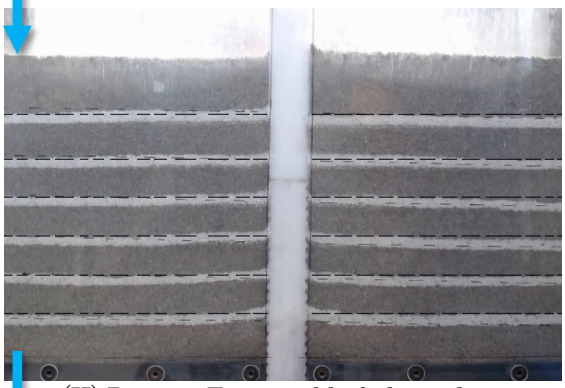

(II) Point 2: First visible failure plane

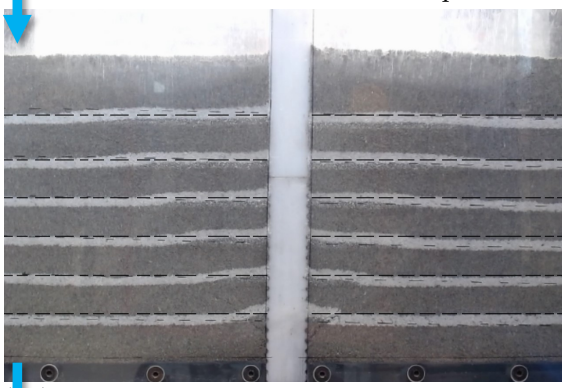

(III) Point 4: Developed to surface. Initial angle

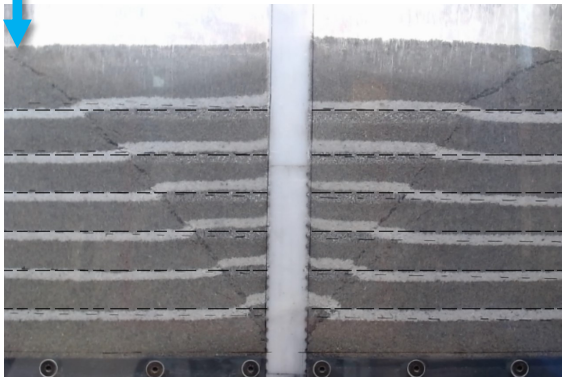

(IV) Phase 4.a -5: Lifting at new angle

Figure 3.25: Photos from Test 1 (left) and Test 2 (right) with Material A.2. The phases correspond to the markings on the plots in Figure 3.24

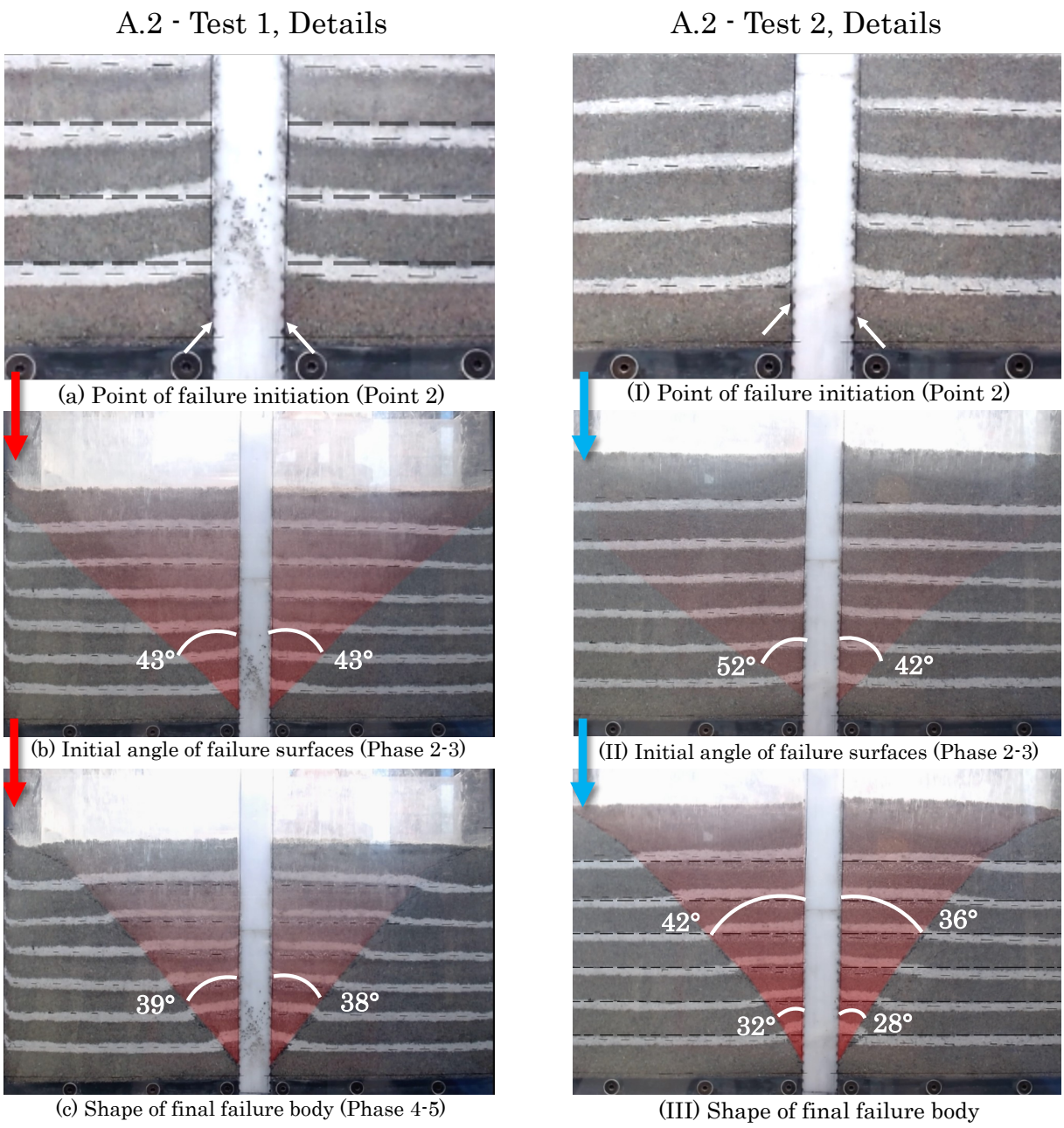

Figure 3.26: Detailed images from test 1 (left) and 2 (right) on material A.2.

The images in Figure 3.26 provide details of the failure initiation points ((a) and (I)), as well as the initial angle of the failure surfaces ((b),(II)) before the body assumes a final shape ((c), (III)). The developed failure visibly curves towards the surface.

Material B.1: 0.5-6.3 mm Dry Eclogite

Two test were run on identical samples of material B.1. Figure 3.27 shows the load-displacement plot from test number 1. A software issue caused the load-displacement data for Test 2 to go missing. Test 1 is therefore described following the plot in Figure 3.27 and video recordings, while Test 2 is described solely by observations from the video. An estimate of the displacement may be made for Test 2, by studying the indicator drawn on the block.

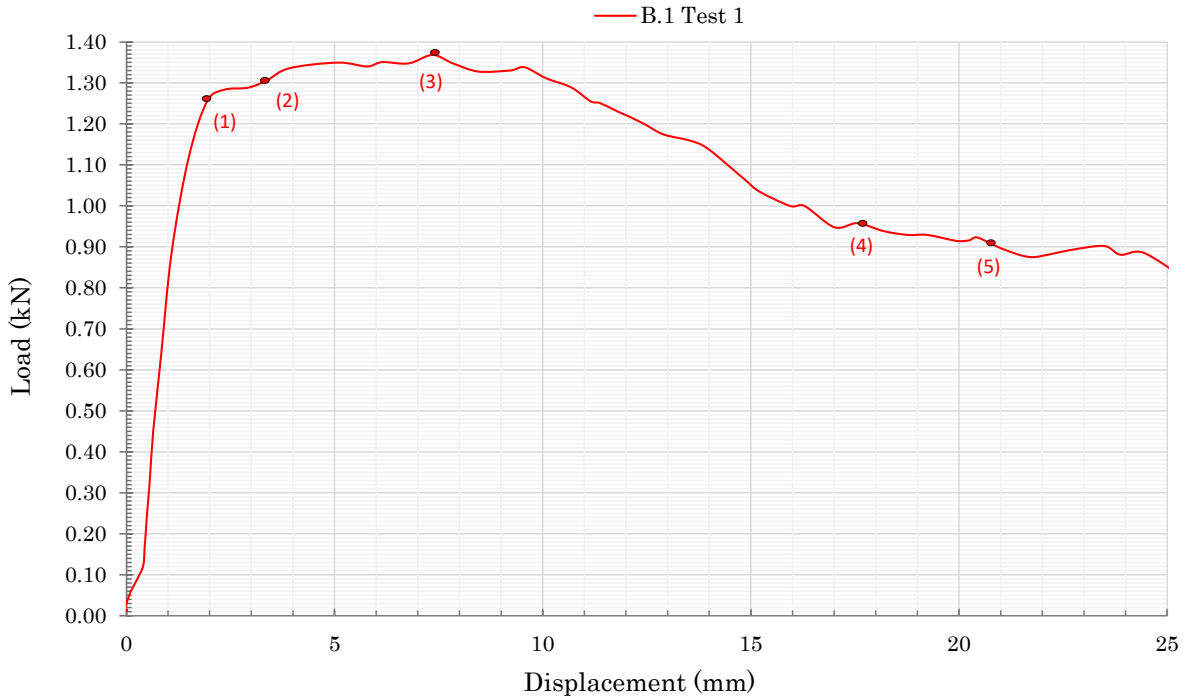

Figure 3.27: Load-Displacement plot for material B.1: 0.5-6.3 mm dry eclogite

Phase 0-1 shows very little visible movement in the frictional material. The response is nearly linear elastic between 0.10 kN to 0.95 kN.

Phase 1-2, the slope abruptly flattens while a slight visible separation initiates from a point near the base of the anchor, inclined towards the surface at a wide angle – observably mobilizing movement in a large, V-shaped portion of the specimen. Movement in the surface material is apparent already during this stage.

Just beyond Point 2, the angle of the mobilized material reduces. Simultaneously, the point from which the failure initiated progresses upward on the block. This new shape appears to remain mostly intact while displacement continues. The resistance is nearly constant (roughly 1.35 kN between 4 mm and 7 mm displacement) until the peak load is reached in Point 3. Then, separation more clearly develops between the V-shaped failure body and the underlying material. The resistance gradually decreases during **Phase 3-4**.

In **Phase 4-5** the shape remains nearly constant, until Point 5, at which loose material begins to slip off the pullout body, thus continuously changing its angle and size.

Beyond Point 5, loose material gradually slips from the block, causing the apex to progress upward, thus mobilizing a continuously shrinking portion of the material. Eventually, the block slips straight through the material (outside of the diagram area).

Visual analysis of Test 2 shows a similar response: During the first 1-2 mm displacement, only very faint movement is detected. When the block has moved approximately 4 mm, the characteristic V-shape visibly forms, with its apex roughly 1 cm from the base of the anchor. Movement of the surface material indicates that the V extends fully to the surface.

The failure body maintains its shape and size as the block proceeds to 12 mm displacement. After this, the angle reduces slightly and the material begins to slip from the block surface, beginning at the V-shape apex and progressing upwards. The angle remains more consistent and the material does not slip as aggressively as it does in Test 1.

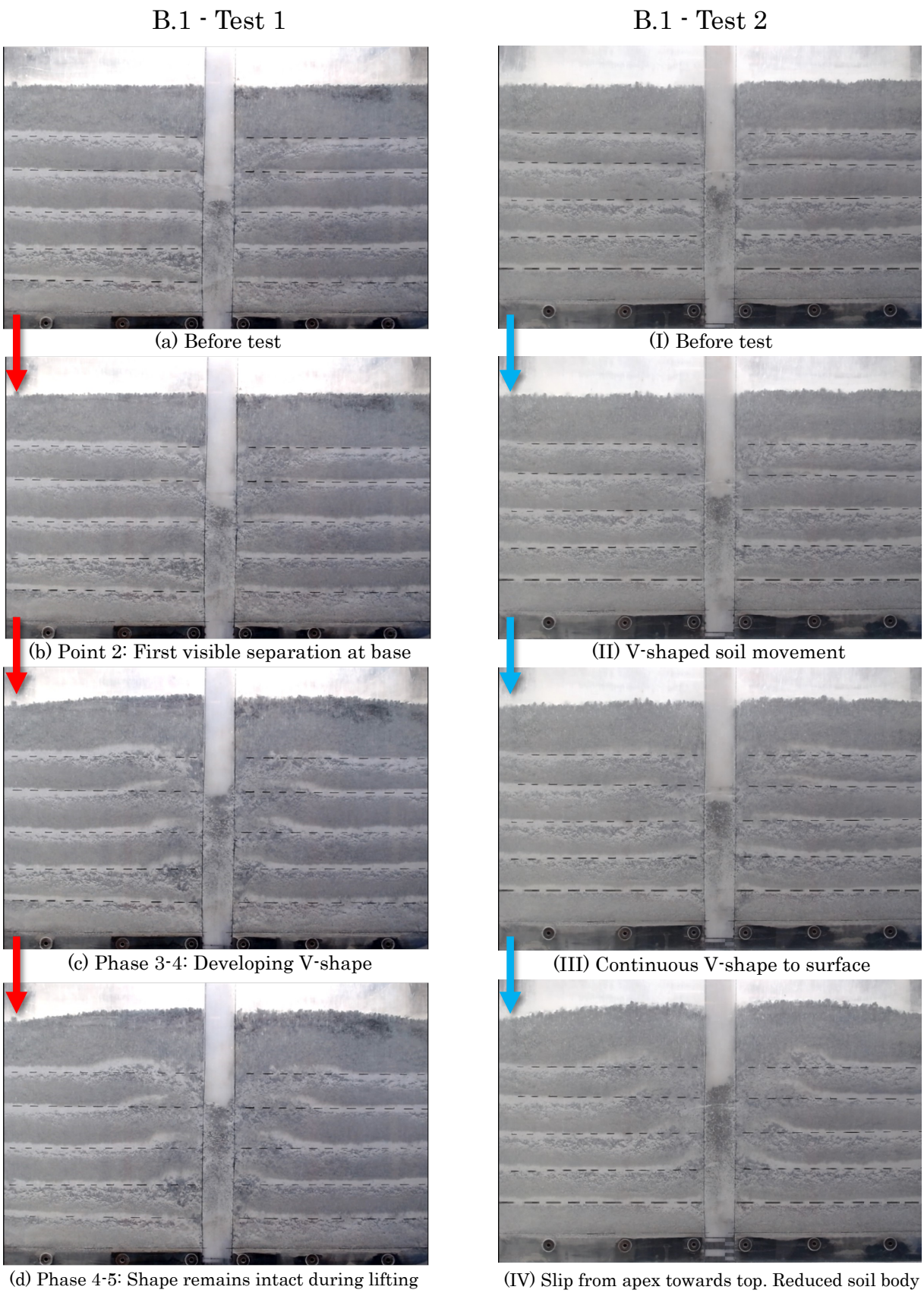

Figure 3.28: Photos from Test 1 (left) and Test 2 (right) with material B.1: 0.5-6.3 mm dry eclogite. Phases correspond to the the markings in Figure 3.27

B.1 - Test 1, Details

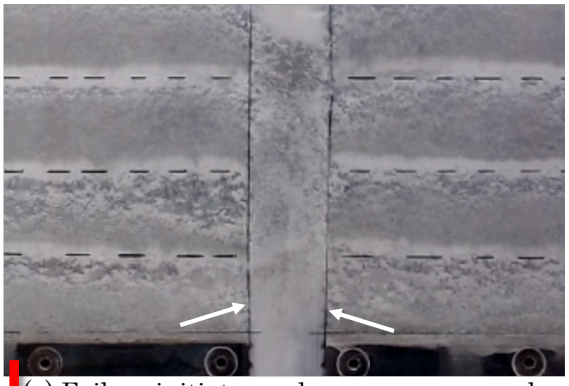

(a) Failure initiates and progresses upwards

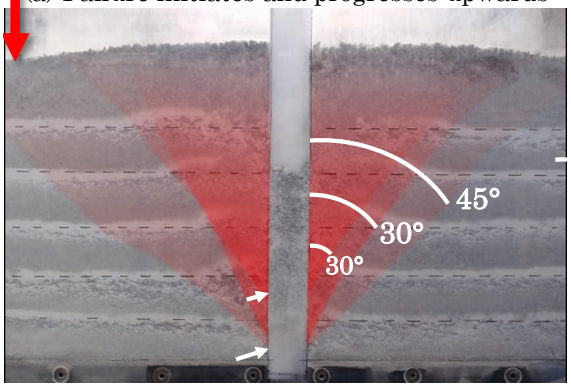

(b) Development from a wide angled soil mass to a narrower, shorter soil body

B.1 - Test 2, Details

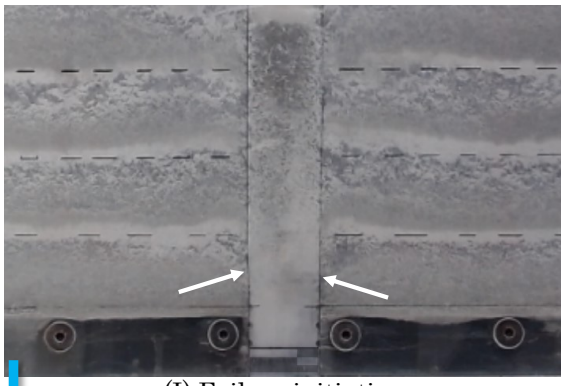

(I) Failure initiation

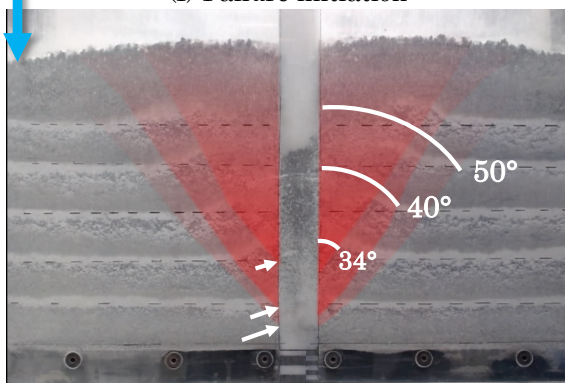

(II) Development from a wide angled soil mass to a narrower, shorter soil body

Figure 3.29: Detailed images from tests on material B.1: 0.5-6.3 mm dry eclogite

Material B.2: 0.5-6.3 mm Moist Eclogite

Two tests were run on separate samples of material B.2: 0.5-6.3 mm moist eclogite. Figure 3.30 shows the load-displacement plot from test number 1 and 2 of Material B.2: 0.5-6.3 mm moist eclogite.

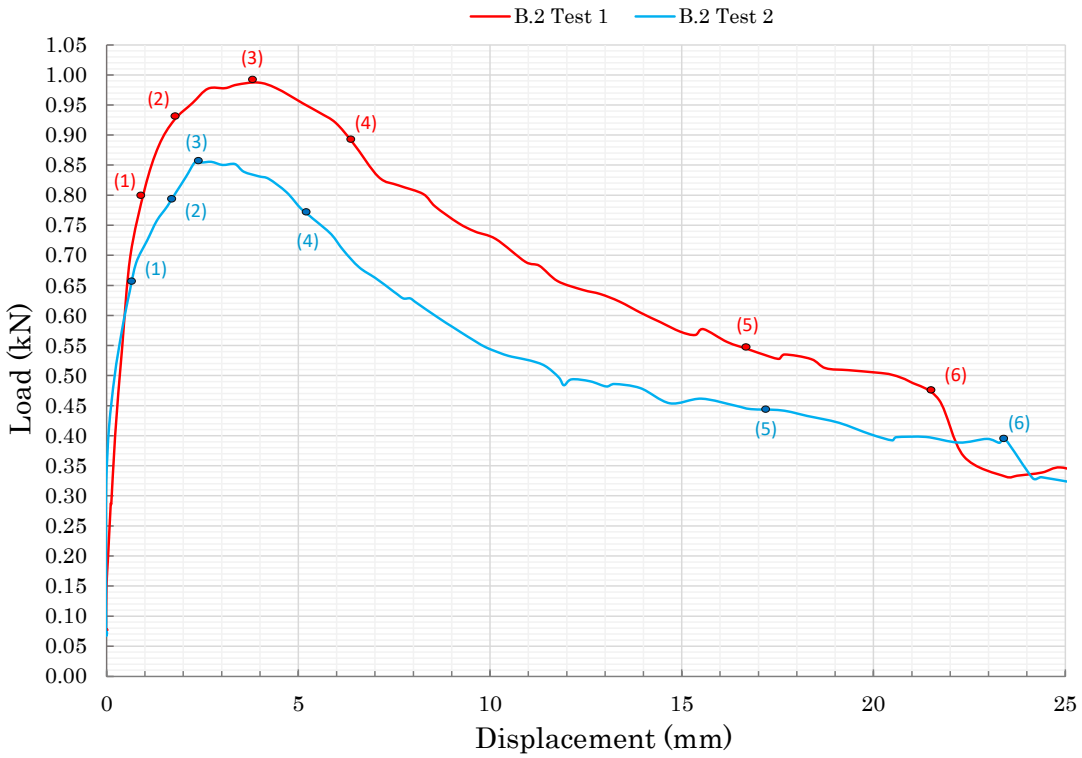

Figure 3.30: Load-Displacement plot for material B.2: 0.5-6.3 mm moist eclogite

In **Phase 0-1**, the system responds with an abrupt load increase over a very small displacement. During **Phase 1-2**, it is possible to see a V-shaped portion of the material begin to mobilize. At Point 2 in Test 2, a small separation begins to form an apex approximately 1.5 cm from the anchor base. No clear separation has yet begun in Test 1 in this phase.

The mobilized, V-shaped body continues to become more distinct, though the angle reduces slightly as the displacement continues to Point 4 (Point 3 denotes the peak load values). At Point 4, the V-shape appears to have reached, which is indicated by faint separation and greater movement in the surface material. During **Phase 4-5**, this continues to develop, while the resistance gradually reduces. From Point 5, the shape remains largely intact, before slipping from the block at Point 6.

Details on the failure shape and development in B.2 are very similar to those of A.2. Inclination angles and failure initiation points are summarized in Table 4 with the results from the other frictional materials.

B.2 - Test 1

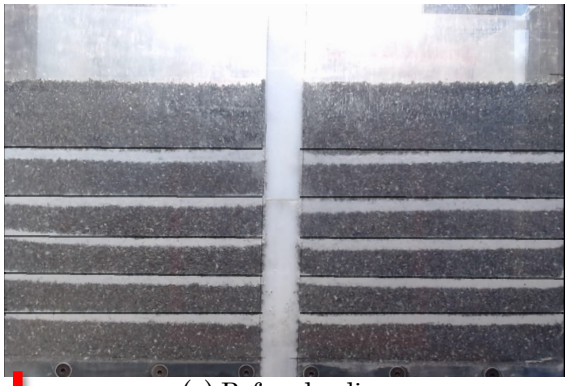

(a) Before loading

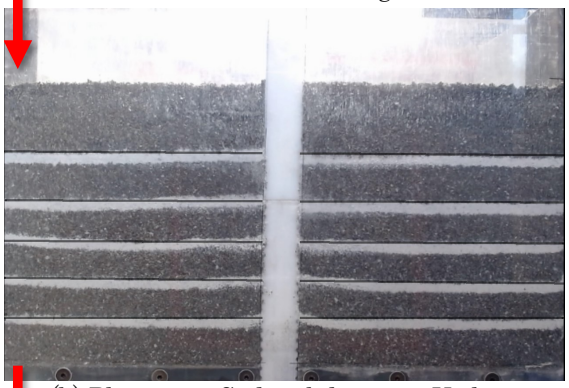

(b) Phase 3-4: Soil mobilizing in V-shape

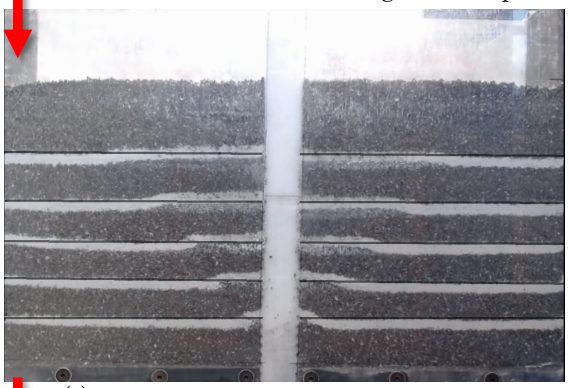

(c) Phase 4-5: Lifting of V-shaped body

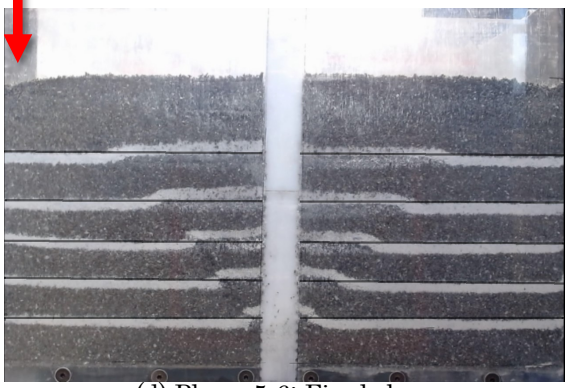

(d) Phase 5-6: Final shape

B.2 - Test 2

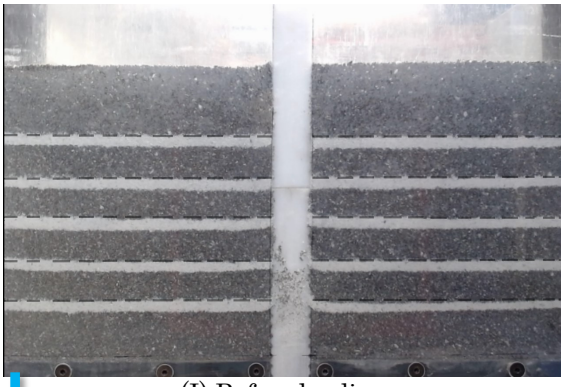

(I) Before loading

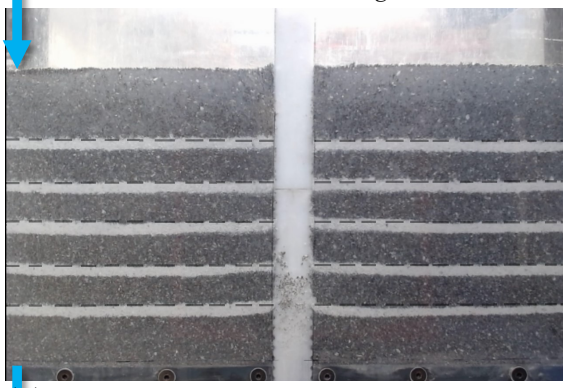

(II) Phase 1-2: V-shape forms with small separatior

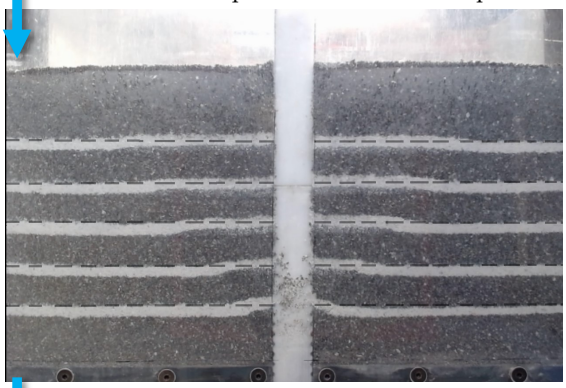

(III) Phase 4-5: V-shape develops at a steeper angle

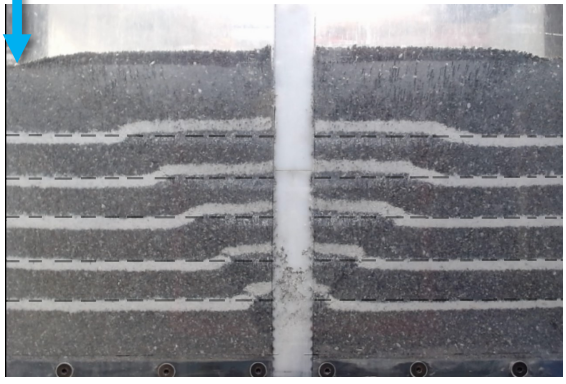

(IV) Phase 5-6: Lift of final shape.

Figure 3.31: Photos from Test 1 (left) and Test 2 (right) with material B.2, the moist 0.5-6.3 mm eclogite. Phases correspond to the the markings in Figure 3.30.

3.4.2 Low-Cohesive Materials

Material C.1: 0-3 mm eclogite with 4% cement

Figure 3.32 shows the load-displacement plot from the test on Material C.1. Note that the material sample has been lifted slightly from the bottom due to slip along the sides before the blocks were clamped on.

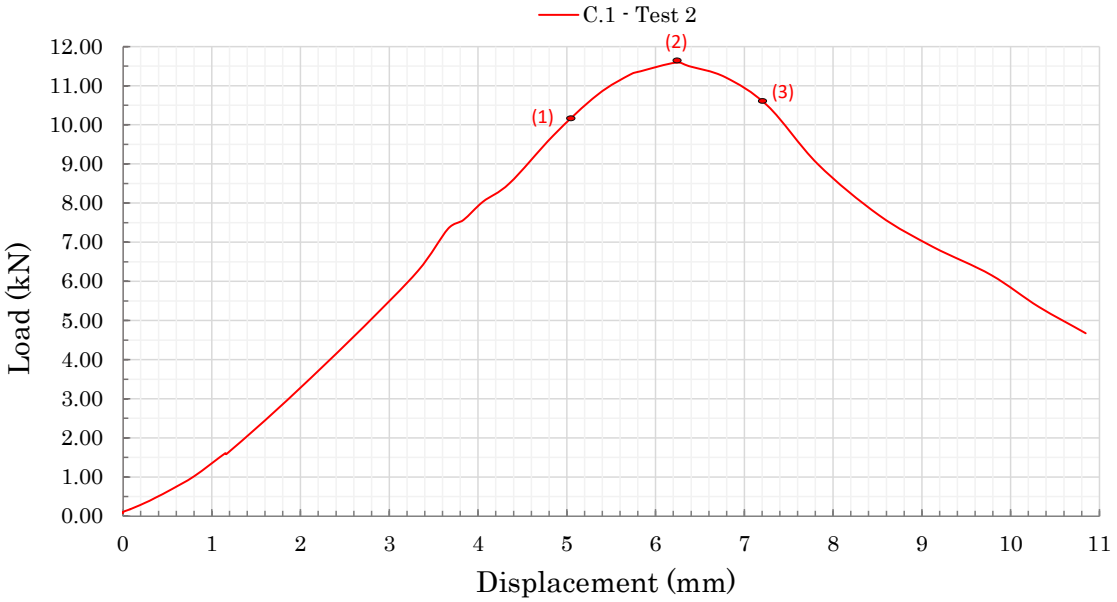

Figure 3.32: Load-Displacement plot for material C.1: 0-3 mm eclogite with 4% cement.

Phase 0-1: slight lifting of the entire block continues initially, before a nearly linear load-displacement response from 1 mm to Point 1. At Point 1 the first visible fractures begin to occur in the material. The fractures appear in the center of the material, forming the same characteristic V-shape as in the soil experiments.

The fracture continues to develop and propagate in both directions at a wide angle. The development appears to halt as the fracture reaches the material located vertically beneath the clamps. Displacement of the block continues, and the peak load is reached – Point 2 in the plot. Now, in **Phase 2-3**, the direction of the fracture propagation shifts, and multiple fractures begin to appear in a zone located beneath the corners of the blocks. These fractures develop to the surface as the resistance reduces beyond Point 3. The curve is nearly symmetric about Point 3.

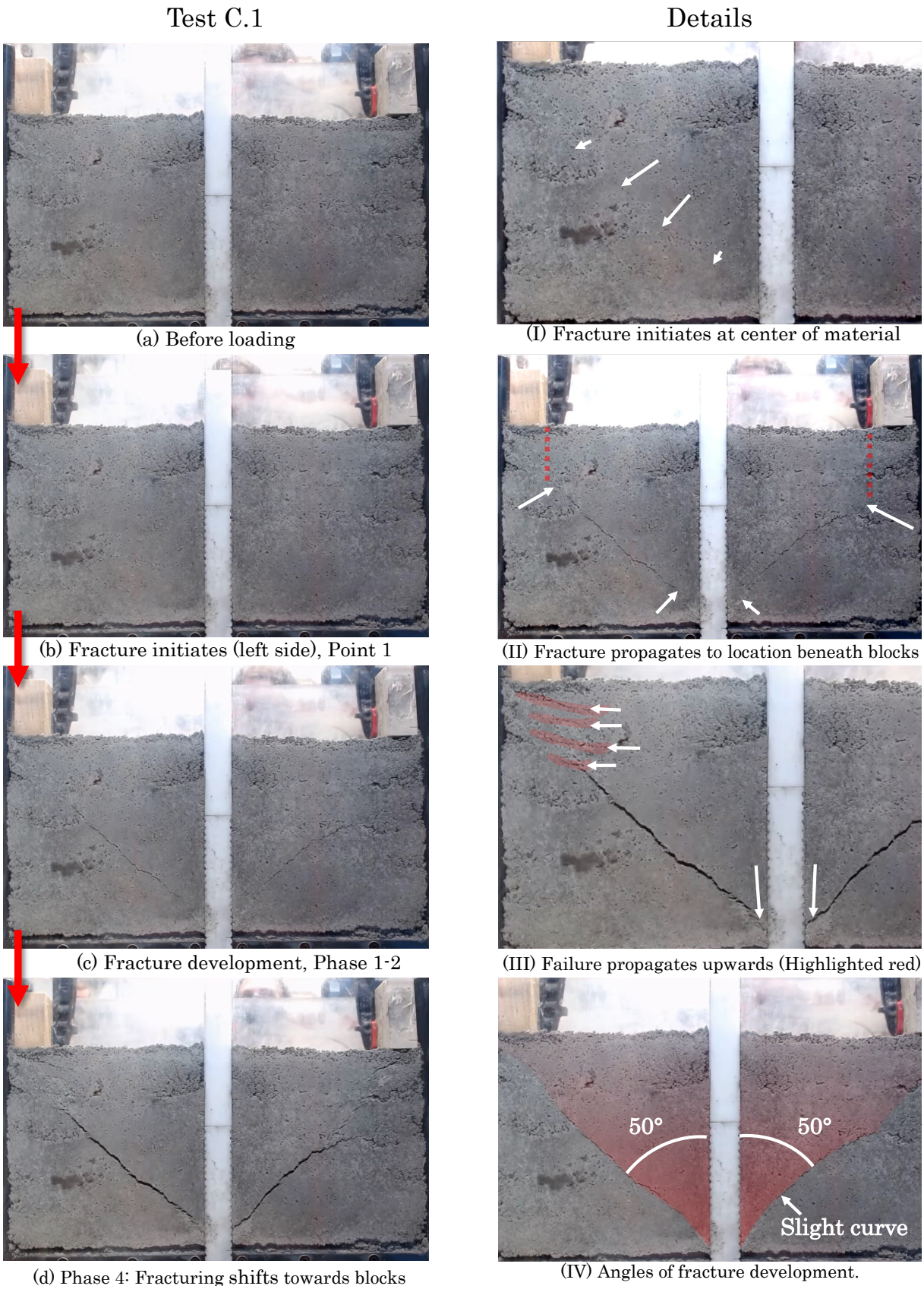

Figure 3.33: Photos from Test on C.1 (left). Phases correspond to the markings in the plot in Figure 3.32. Detailed images on the right.

Material C.2: 0-3 mm eclogite with 2% cement

Figure 3.34 shows the load-displacement plot for material C.2, a concrete containing 0-3 mm eclogite with 2% cement.

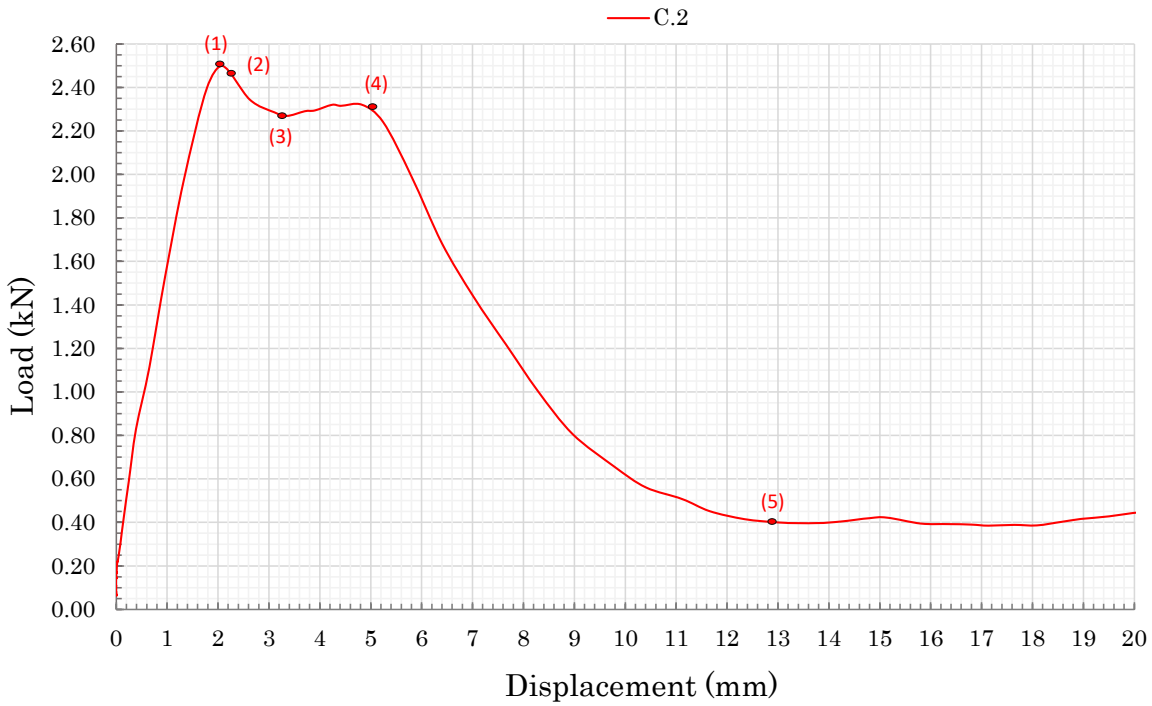

Figure 3.34: Load-Displacement plot for material C.2

The plot shows a linear-elastic response during **Phase 0-1**. At the peak load in Point 1, the first indication of a fracture begins to appear, in the center of the material. During **Phase 1-2** – lasting only a second and accounting for only 0.2 mm displacement – the fracture abruptly develops on both sides, propagating from the initial fracture in the center towards the anchor base and surface. Thus, the fracture creates the characteristic V-shaped failure body.

The development continues to Point 3, at which the fracture seems to have developed to the socket and surface on the right hand side. This development is less clear for the left hand side.

During **Phase 3-4**, fracture continues to develop by breaking small material bridges. There is a small load increase, before the resistance quickly reduces beyond Point 4. Intact material bridges continue to be sheared off during **Phase 4-5**, after which the complete V-shaped body is lifted at a nearly constant load.

Test C.2

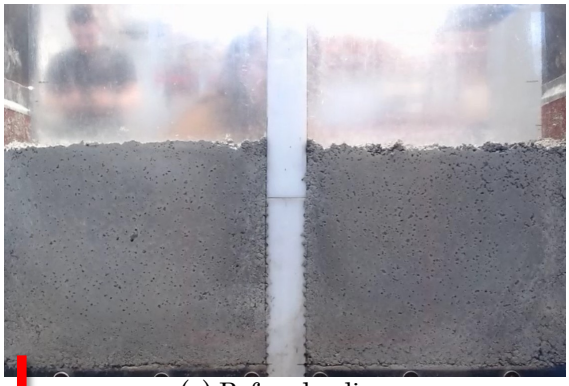

(a) Before loading

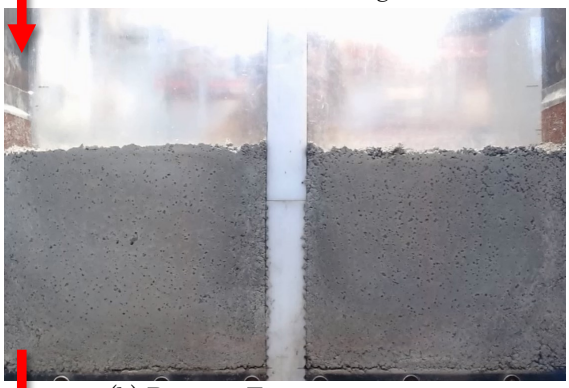

(b) Point 1: Fracture initiation

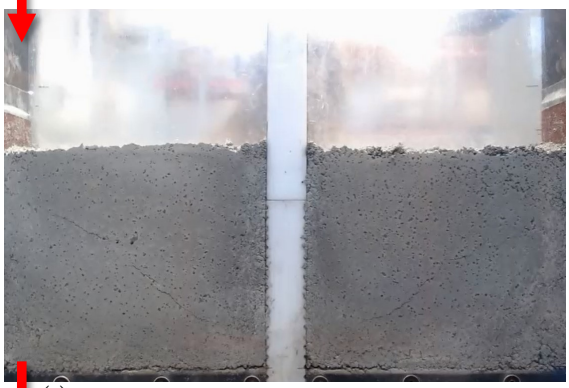

(c) Point 2: Propagating in both directions

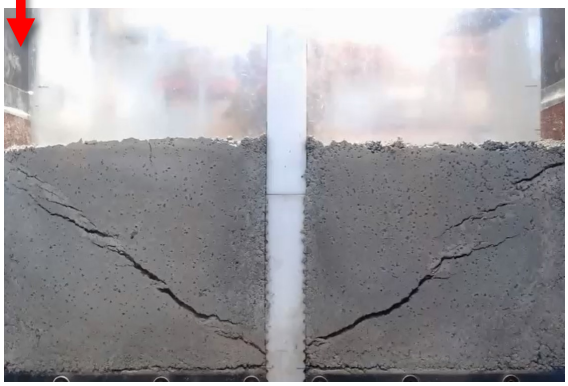

(d) Phase 4-5: Breaking intact bridges,

Details

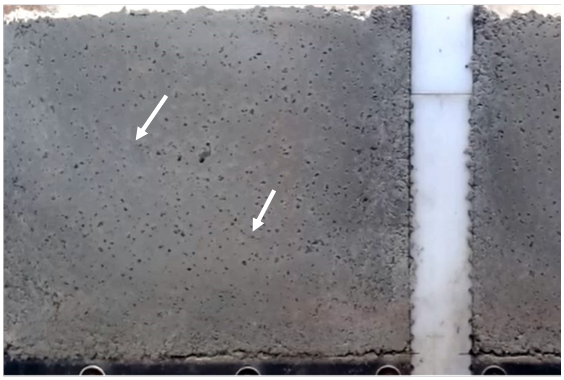

(I) Close-up of fracturing at Point 1

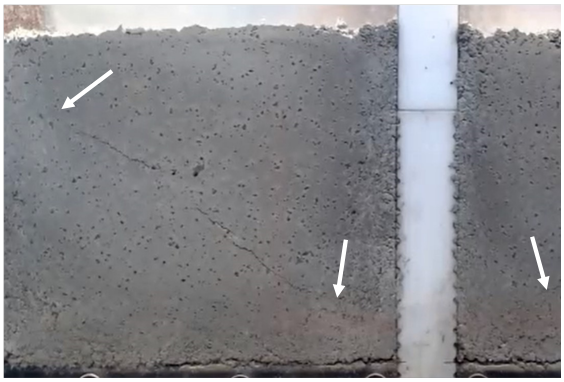

(II) Extent of visible fractures, Point 2

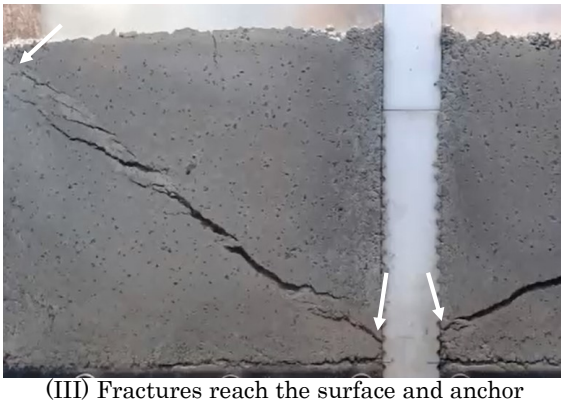

(III) Fractures reach the surface and anchor

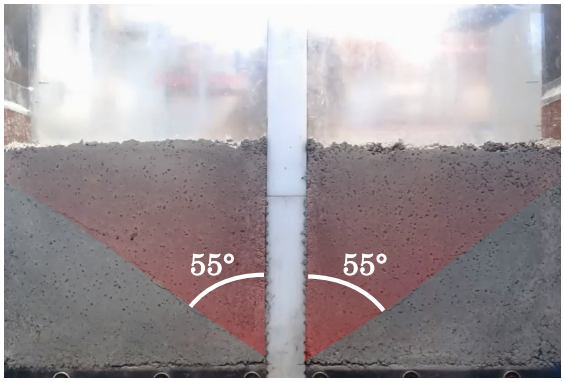

(IV) Failure angle

Figure 3.35: (a-d): Photos from test C.2, corresponding to the phases in Figure 3.34. (I-IV): Details from test C.2

3.4.3 Summary

Visible Observations

Key features of the failure patterns in the frictional and low-cohesive materials are listed in Table 4 and Table 5, respectively.

Table 4: Failure characteristics for the frictional materials. The apex point is measured from the base of the test chamber. "Initial" means the very first angle the separation attains from the socket, while "Final" gives the angle of the final shape, generally measured near the center of the sample, unless otherwise specified.

Type	Test No.	Material Depth, d (cm)	Failure Description				
			Apex Point, x (cm)	Angle (°)			Shape
				Initial	*Final*		
A.1	1	31	3.0-4.0	26-29	38-40		Curved V
	2	30	3.0-3.5	36-42	36-42		Straight V
A.2	1	28	≈ 1.0	43	38-39		Curved V
	2	29	1.0-2.5	42-52	28-32 36-42	(at socket) (at center)	Curved V
B.1	1	30	≈ 1.5	45-52	30		Curved V
	2	28	≈ 1.5	45-50	32-34		Varying V
B.2	1	29	3.5-4.5	32-36	32-36		Slightly Curved V
	2	29	3.5-4.0	31-37	37-38		Curved V

Table 5: Summary of the failure characteristics for each test on the low-cohesive materials. The apex point is measured vertically from the base of the test chamber.

Type	Material Depth, d (cm)	Failure Description			
		Initiation Point	Apex Point, x (cm)	Angle (°)	Shape
C.1	28	Center of material	2.0-3.0	50	V-shape w/ faint curve
C.2	20	Center of material	1.5-2.5	55	V-shaped

The angle with which the *curved* failure surfaces intercept with the horizontal surface, θ_i were measured and compared to the typical interception angle, ψ, for circular arc failure surfaces as proposed by Ball (1961). Figure 3.36 shows an example of how θ_i is measured. The results are listed in Table 6. Interception angles for tests A.1 test 2, C.1 and C.2 are omitted, as their failure surfaces were straight or did not intercept with the horizontal surface.

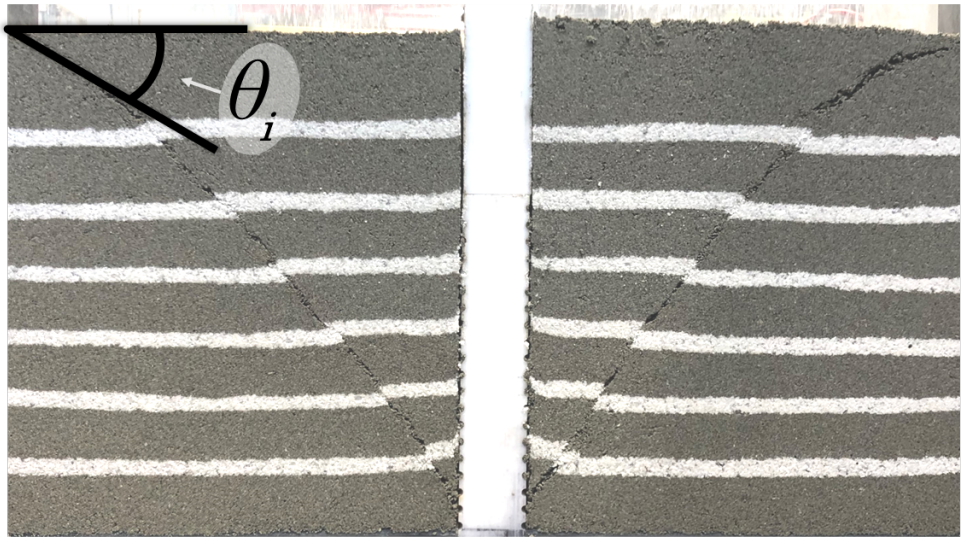

Figure 3.36: Example showing how the failure surface's interception angle with the horizontal is measured, Here, from material A.2 (0-3 mm moist eclogite).

Table 6: Curved failure surfaces' interception angles, θ_i, with the surface (horizontal), and comparison to ψ as proposed by Ball (1961) .

Type	**A.1**		**A.2**		**B.1**		**B.2**		**C.1**	**C.2**
Test No.	*1*	*2*	*1*	*2*	*1*	*2*	*1*	*2*		
Interception Angle, θ_i										
Left Side	37	-	20	22	43	40	30	28	-	-
Right Side	36	-	22	20	40	38	28	40	-	-
φ_{peak}	39	39	35	35	43	43	38	38	Unk.	Unk.
ψ, (45-φ_{peak}/2) (°)	26	-	28	28	24	24	26	26	-	-
θ_i *Deviation from* ψ (°)										
Left Side	11	-	-8	-3	19	16	4	2	-	-
Right Side	10	-	-6	-8	16	14	10	14	-	-
Average	10.5	-	-7	-5.5	17.5	15	7	8	-	-

Load-Displacement Characteristics

Table 7 on the next page summarizes key load-displacement measurements from all the physical tests, namely the phase of nearly linear-elastic material response and the peak resistance values.

Table 7: Maximum resistance and displacement of the linear elastic phase, and values at the peak load, P.

Material	**A.1**		**A.2**		**B.1**		**B.2**		**C.1**	**C.2**
Test No.	*1*	*2*	*1*	*2*	*1*	*2*	*1*	*2*		
Linear Phase Approx. Max Load (kN)	1.0	0.98	0.83	0.80	1.3	-	0.80	0.65	10	2.3
Linear Phase Approx. Max Displ. (mm)	1.1	1.3	0.80	1.5	2.0	-	1.0	0.70	5.0	2.0
Peak Load, P (kN)	1.28	1.09	1.18	1.02	1.37	-	0.988	0.856	11.6	2.50
Displ. At P (mm)	6.7	4.2	4.4	4.4	7.2	-	4.0	2.7	6.2	2.6

4 Numerical Modeling

4.1 Model Setup

Two-dimensional numerical models were created in RS2 (version 2019 11.002, Rocscience Inc.) to replicate the physical test apparatus as accurately as possible, thereby extending the study of the stress and failure conditions in the material, and allowing for easy parameter variations. A model draft was created using empirically guided estimations of the material properties as input parameters. Studies of the model at this preliminary stage aimed to generate a model that resembled the expectations of the designer, meaning that the output was in accordance with theory. Determining if the assigned conditions provided a reliable model required validations against results obtained from the physical model tests. Three numerical models were created and validated against the physical model tests: One simulating frictional material and two simulating cohesive materials.

4.1.1 Geometry and Boundary Conditions

A geometry with the same dimensions as the PVC test chamber and "anchor block" were created and assigned appropriate boundary conditions:

- unbound top surface on the soil/rock material,
- fixed vertical outer boundaries,
- rollers on the horizontal, lower boundary,
- fixed corners,
- staged, displacement-controlled joint boundaries on the moving anchor block, and
- a material surface boundary which be adjusted to to resemble the physical tests.

The interface between the test material and moving block was modeled by creating two different joint surfaces around the block – one artificially strong joint replicating the rough socket, "Socket Joint", the other one weak, "Smooth Joint". These joint surface conditions are necessary, since "if only material boundaries are used to separate the blocks, they will behave as a continuum" (Rocscience, 2020), thus, not allowing slip to occur between the two materials, and no frictional interaction. Both elastic and inelastic slip may occur along a joint boundary in RS2. Joints are assigned strength and stiffness properties that control how the boundaries respond to applied stresses (Rocscience, 2020).

However, a problem arises at the location where the Socket Joint and lower material boundaries intercept: It is not possible to assign boundary conditions at these nodes which satisfy the real physical behavior of both a) the immobile bottom frame, and b) the moving interface of the block as it passes this location. This would require assigning contradicting conditions to a single node. In this case, the best solution was found to be a fixed node at

these two points. The issue of compatibility is considered to be overcome as long as the vertical displacement does not surpass the local element size at these points. Therefore, mesh element density was increased from 10.0 mm above the bottom frame, while leaving the elements at the fixed nodes slightly larger, as shown in Figure 4.2

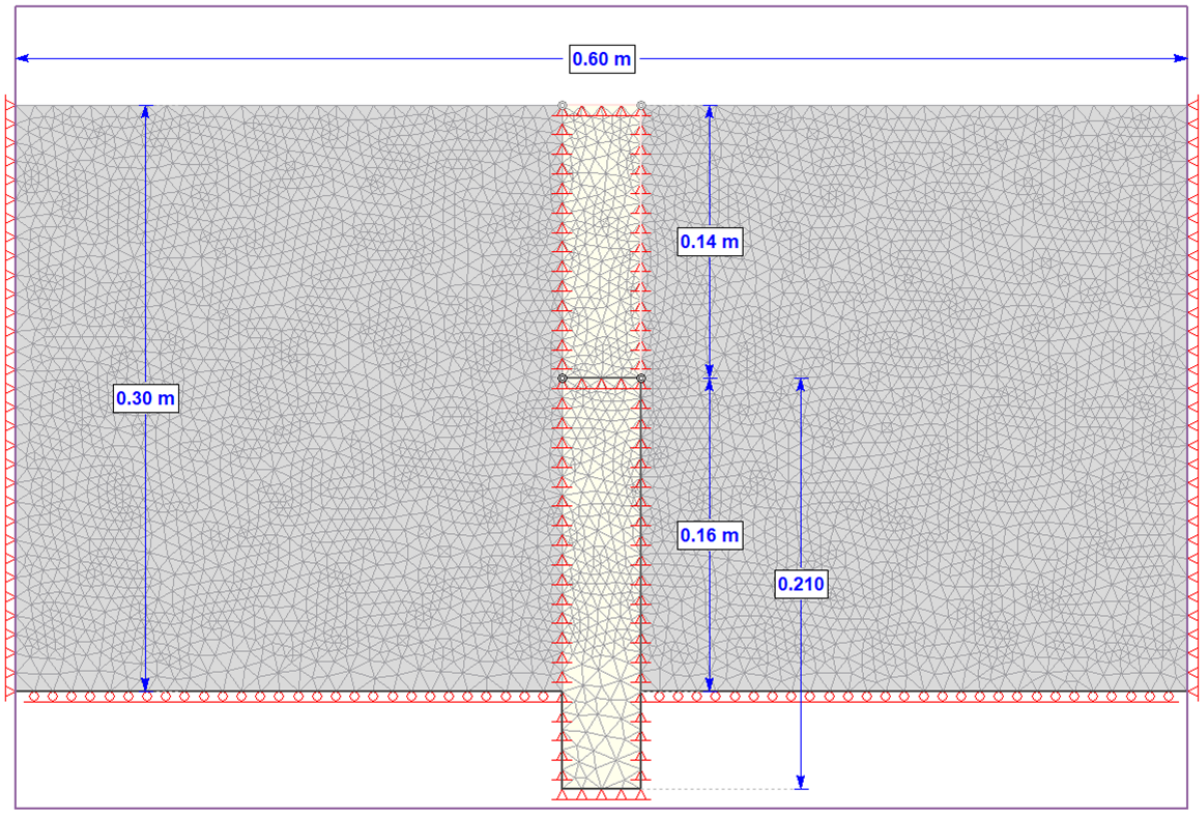

Figure 4.1: Geometry setup, mesh and boundary conditions of model in RS2 – initial stage.

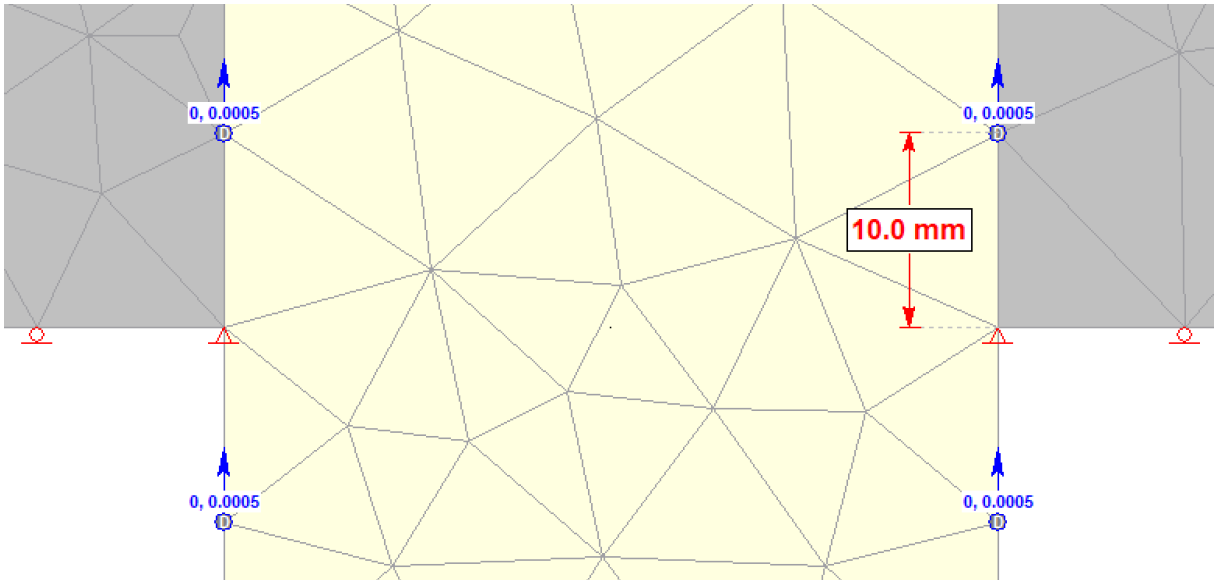

Figure 4.2: Enlarged image of the boundary conditions where the Socket Joint meets the lower boundary. The blue arrows show the assigned displacement (in meters) on the joint block in the current stage. Nodes at the intersections are fixed. The neighboring elements are 10.0 mm tall – larger than the total displacement studied in the simulations.

The fixed nodes do, however, create unrealistically high and low stresses within the anchor block at these points. This means that a load-controlled displacement will not be appropriate for this setup. Alternatives to the setup will be suggested in the Discussions.

Results from the physical models revealed that failure would in all but one case initiate well before the socket reaches 1.0 mm displacement, thus justifying studying a small total displacement numerically. Table 8 shows the assigned vertical displacement to the anchor block in each stage:

Table 8: Assigned vertical displacement on the anchor block joint boundaries at each stage.

Stage No.	**1. Initial**	**2**	**3**	**4**	**5**	**6**	**7**	**8**	**9**	**10**	**11**	**12**	**13**	**14**	**15**	**16**
Displacement (mm)	0.0	0.5	0.75	1.0	1.5	2.0	2.5	3.0	3.5	4.0	4.5	5.0	5.5	6.0	6.5	7.0

4.1.2 Input Parameters

Input parameters include the mechanical properties of the joints and materials, as well as the applied stresses. Physical tests on material A.1 (0-3mm dry eclogite) create the basis for input parameters in model "Soil 1". Similarly, parameters for model "Soil 2" are obtained from tests on material A.2 (0-3 mm moist eclogite). Values for Young's modulus and Poisson's Ratio are estimated from typical soil properties listed in BOUASSIDA GEOTECHNICS (Tables C.2 and C.4).

Models "Rock 1" and "Rock 2" aim to replicate findings from tests on the low-cohesive materials, C.1 (0-3 mm eclogite, 4 % cement) and C.2 (0-3 mm eclogite, 2 % cement). The cohesion value is estimated by constructing Mohr's circle with the average UCS values obtained from 3.2.2 and assumed internal friction angles of 60° and 55° for Rock 1 and Rock 2, respectively. Tensile strength was estimated as 0.1 times the cohesion, then adjusted incrementally based on the agreement between the physical observations and the numerical results. The final material input properties applied in the models are listed in Table 10.

Joint Properties

The mechanical properties of the joint surfaces remained the same through all the simulations. The Smooth Joint was assigned a negligibly low strength as it is intended to slip from the first movement. The Socket Joint is not assigned a slip-criterion, meaning that the contact behaves elastically according to its normal and shear stiffness. This way, the focus will be on studying failure in the test material itself, rather than on the contact.

In-Situ Stresses

The models are loaded under gravitational loading conditions, with equal horizontal to vertical stresses, i.e. $k = 1$. Model Soil 1 is applied an additional locked-in horizontal

stress of 0.0001 MPa to simulate a small horizontal stress increase from compaction in the physical model.

Table 9: Mechanical properties of joints defining the moving block.

Joint Name	Slip Criterion	Tensile strength (MPa)	Peak Cohesion (MPa)	Peak friction angle (°)	Normal Stiffness (MPa/m)	Shear Stiffness (MPa/m)
Smooth Joint	Mohr-Coulomb	0.0	0.0	0.1	1000	100
Socket Joint	None		N/A	N/A	2000	2000

Table 10: Material input values.

Property	Soil 1	Rock 1	Rock 2	Anchor Block
Unit Weight (MN/m3)	0.0210	0.0226	0.0233	0.0270
Stiffness				
Poisson's Ratio, ν	0.25	0.30	0.30	0.10
Young's Modulus (Mpa)	100	32	5	50000
Residual Young's Modulus (Mpa)	N/A	N/A	N/A	N/A
Failure Criterion	M-C	M-C	M-C	M-C
Material Type	Plastic	Plastic	Plastic	Elastic
Peak Strength				
Peak Tensile Strength (Mpa)	0	0.075	0.060	10
Peak Friction Angle (°)	39	60	55	45
Peak Cohesion (Mpa)	0	0.12	0.075	50
Residual Strength				
Residual Friction Angle (°)	36	40	40	N/A
Residual Cohesion (Mpa)	0	0	0	N/A
Dilation Angle (°)	0	0	0	N/A

4.2 Analysis

4.2.1 Model: Soil 1

Principle Stresses

Model Soil 1 aims to replicate a frictional material from test A.1 (0-3 mm dry eclogite) loaded under gravitational conditions, with a small horizontal stress applied in-situ, 0.0001 MPa, to simulate stresses from compaction. Thus, the principle stresses, σ_1 and σ_3, are initially orientated straight vertically and horizontally. An abrupt change to the orientation of σ_1 and σ_3 occurs after only a small displacement is applied to the anchor block. σ_1 visibly arches from an area of stress concentration at the surface of the socket, towards the material surface and vertical boundaries, as may be seen in Figure 4.3. Notice also how stress is reduced below the pressure arch.

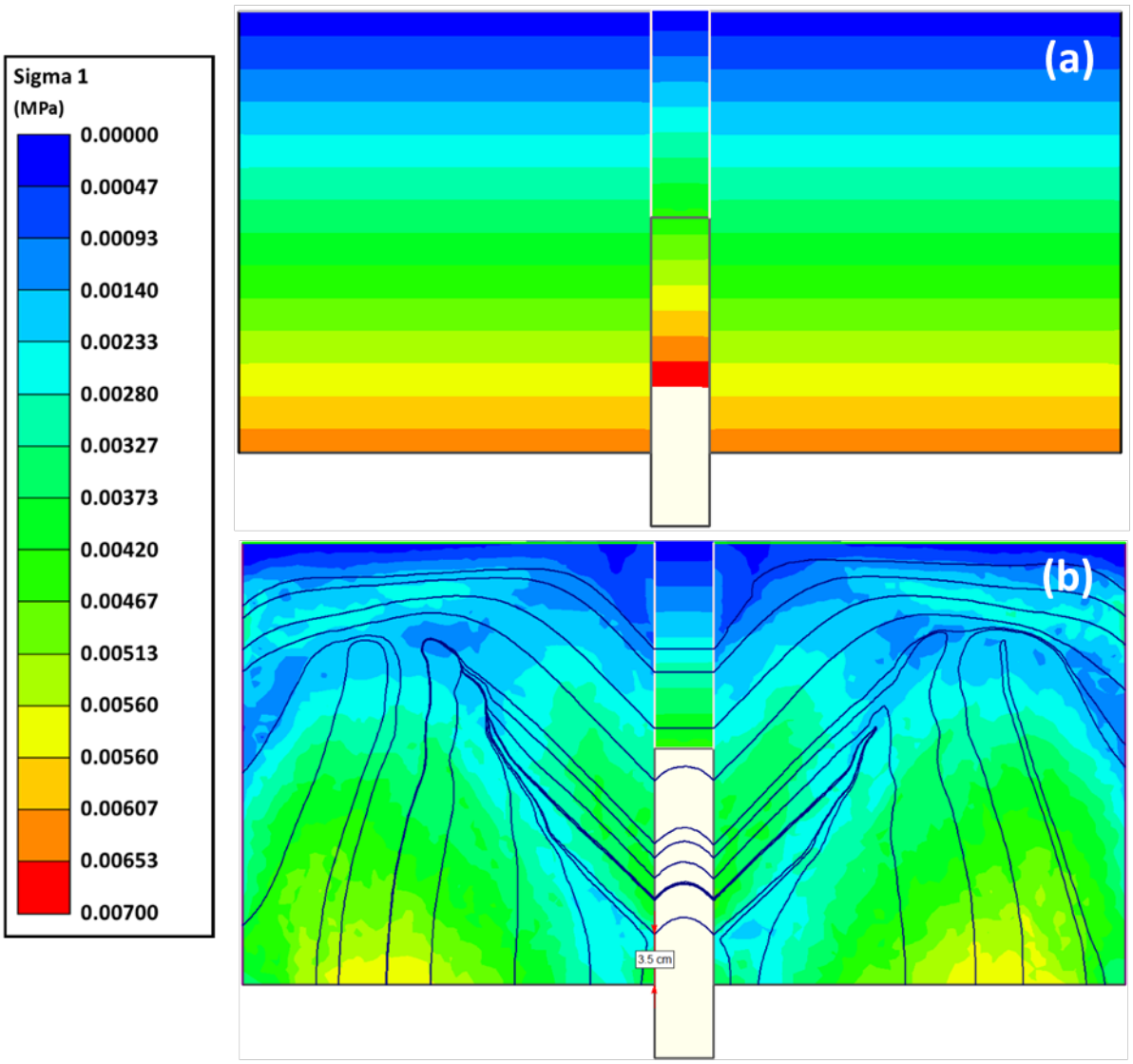

Figure 4.3: Initial stress state (a) and σ_1 stress flow directions (navy colored lines) (b) at 1.0 mm anchor displacement.

σ_1 clearly concentrates in a V-shaped zone with its apex at 3.5 mm from the anchor base. The direction of σ_1 is inclined approximately 45° from the anchor axis. The flow lines

gradually flatten toward the surface and begin to slope downward at the vertical boundaries. The enlarged images in Figure 4.4 show the increase of σ_1 at query points taken in the initial state (a) and within the pressure arch in (b), at 1.0 mm anchor displacement.

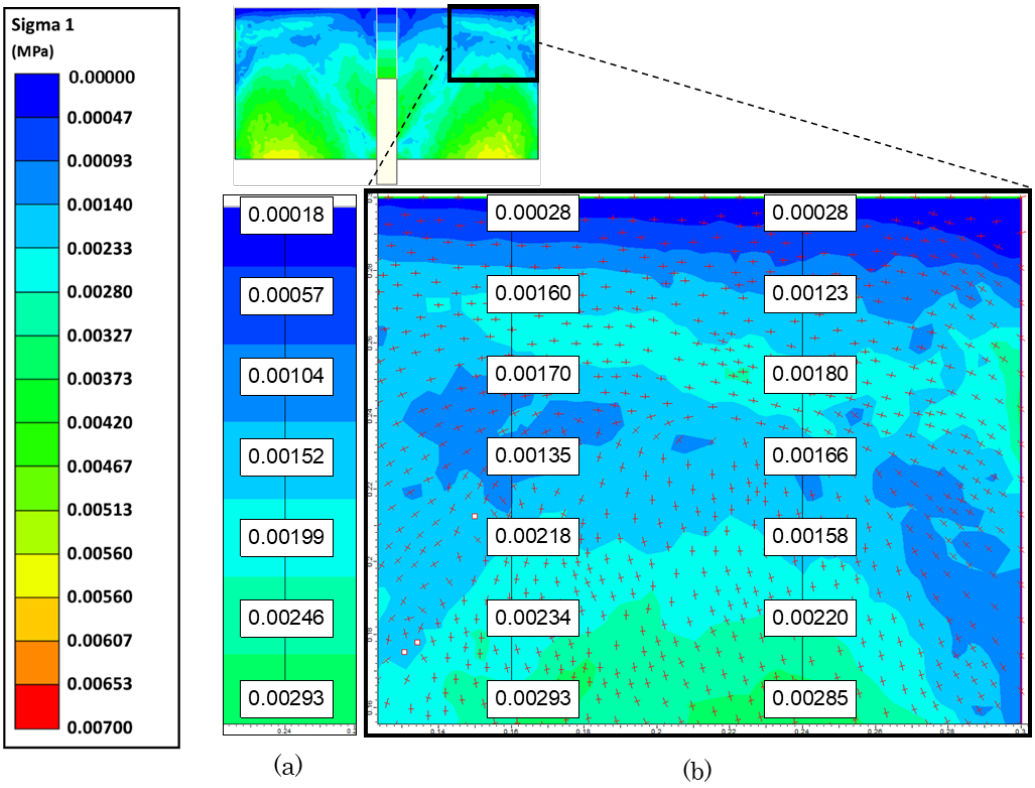

Figure 4.4: Enlarged image of σ_1 query points taken within the pressure arch (b) at 1.0 mm displacement, compared to initial state values in (a).

At 7.0 mm anchor displacement, which is where definite failure surfaces became visible in the physical test (Material A.1, test 2), the stress flow paths have attained a much narrower angle, approximately 30° from the anchor axis, as seen in Figure 4.5:

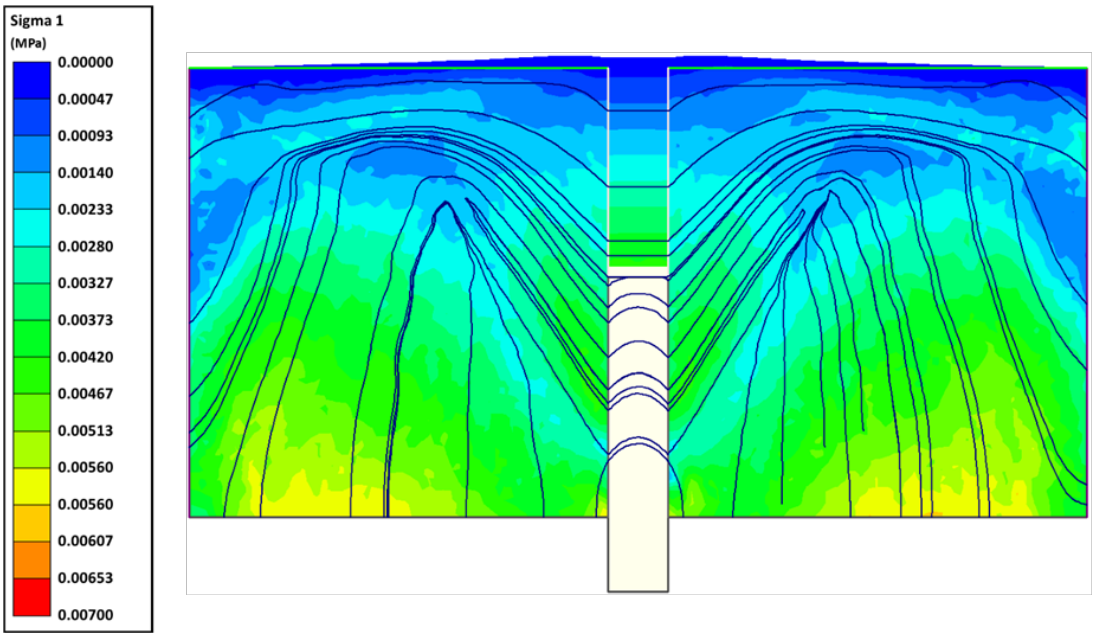

Figure 4.5: σ_1 stress flow lines at 7.0 mm anchor displacement.

Strain Analysis

The soil is in a state of shearing. As physical tests showed, separation from failure planes became visible at 7.0 mm anchor displacement. Separation between nodes is not possible according to the nature of FEM, however, plastic stain in these areas indicate where these failure planes are expected to appear. At 1.0 mm anchor displacement, which is when the material first visibly mobilized during physical tests, strain contours branch out from the apex of the influenced zone, at 38 and 39 degrees from the anchor axis. Note: the peak friction angle of the material is 39°.

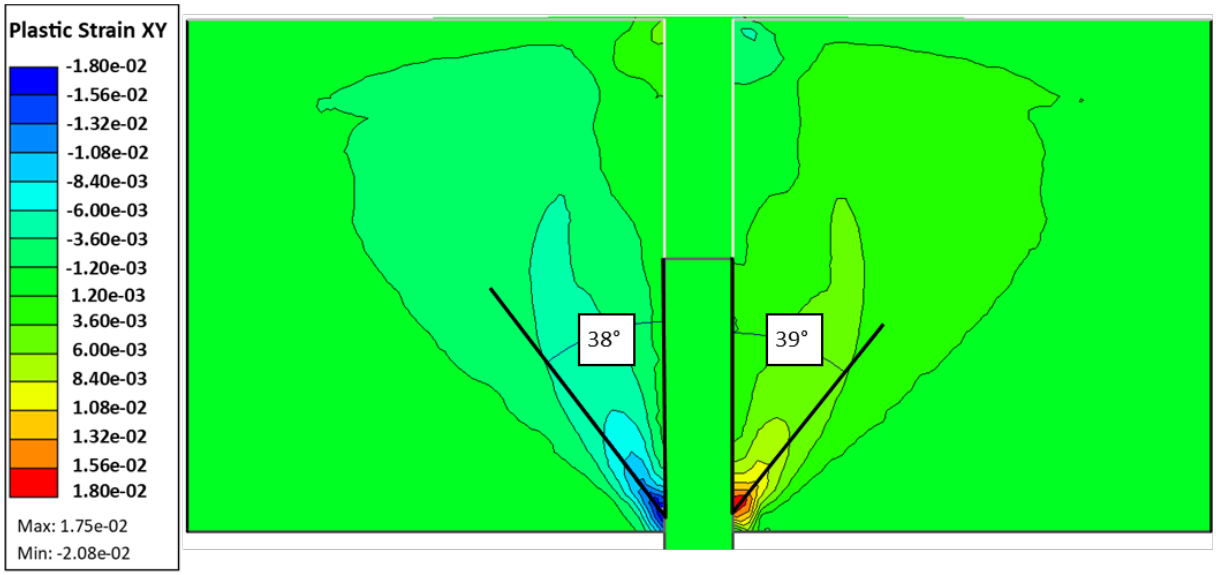

Figure 4.6: Strain contours at 1.0 mm anchor displacement.

The strain contours develop with the anchor's displacement. At 7.0 mm, the angle appears narrower, roughly 35°, which equals the material's residual friction angle. In these strain zones, the material is expected to fail, thus creating the delimited uplift body observed in the physical tests.

Material Displacement

Studying the total displacement over several stages, it is clear that the anchor mobilizes a wide V-shaped body of soil. This agrees well with what is to found in the physical tests. The affected zone has its apex 1.0-1.5 cm from the anchor base. Figure 4.7 shows the total displacement in the material at 1.0 mm (a) and 5.0 mm (b). These represent points in the physical tests (Material A.1) where movement first became observable and where a distinct V-shaped portion of soil was mobilized. Also notice that the displacement of the top soil slightly exceeds the displacement value of the anchor.

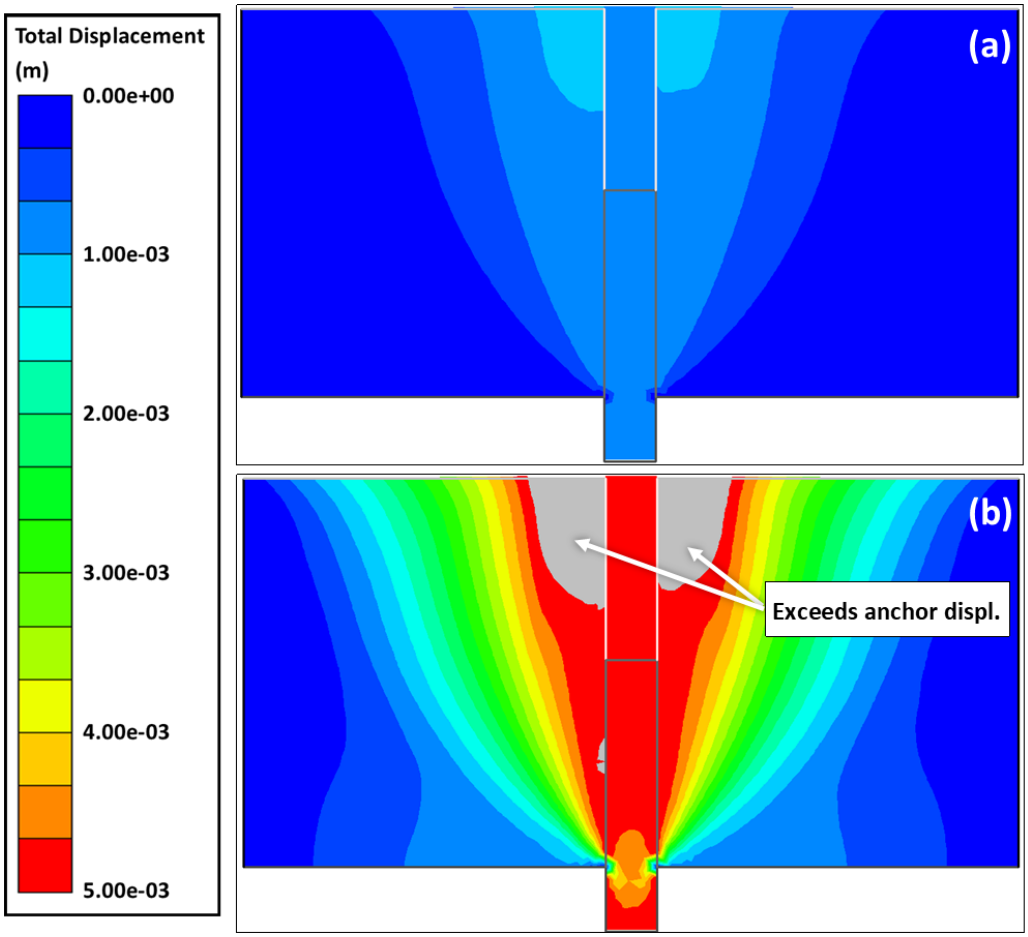

Figure 4.7: Total displacement at (a) 1.0 mm and (b) 5.0 mm anchor displacement.

The boundaries of the mobilized zone agree well with the contours of greatest strain, as shown in the side-by-side comparison in Figure 4.8.

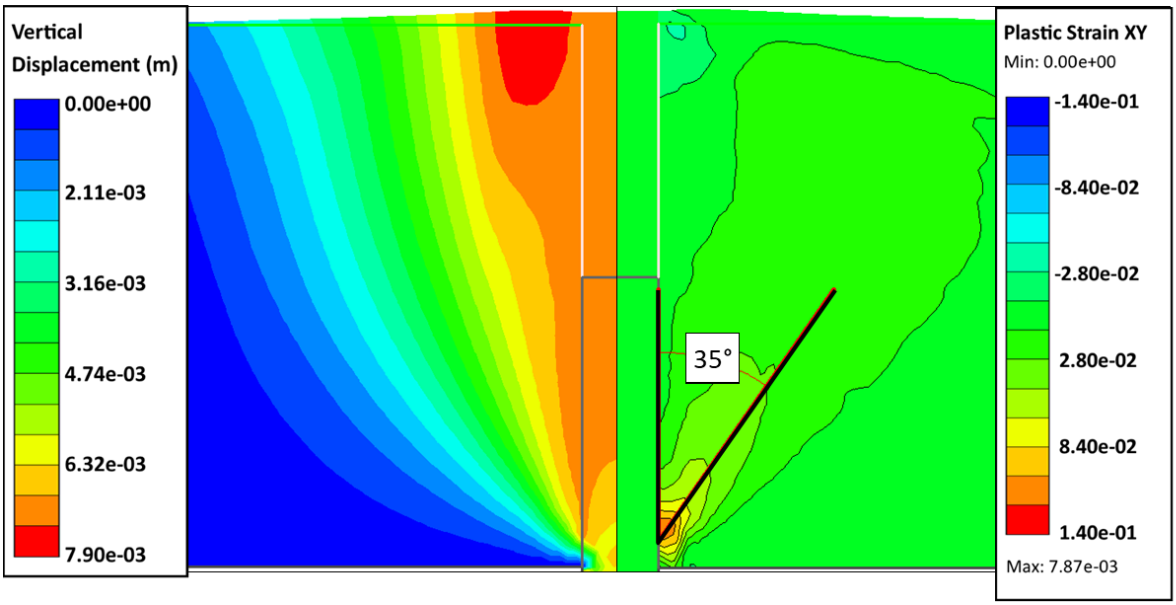

Figure 4.8: The figure shows a side-by-side comparison between the absolute vertical displacement (left side) and the plastic strain contours (right side), at 7.0 mm anchor displacement.

Comments:

- Arching effects as those described in 2.2 are undoubtedly in effect through the material, namely:

  1) the re-orientation of σ_1 and σ_3, causing σ_1 to follow arched stress flow trajectories from the socket toward the surface and wall boundaries,

  2) the pressure increase in the σ_1 arch, and

  3) the pressure reduction below the σ_1 arch, as the arch supports some of the weight.

- The area of increased pressure initiates roughly from the center on the socket

- Cone of mobilized soil initiates from a lower point – lower than what is observed in the physical tests, which was between 3.0 and 4.0 cm. Of course, the location of this apex is likely to be affected by the two fixed nodes described earlier.

- The angle of the maximum strain contours develops from approximately the peak friction angle, and narrows to the residual friction angle.

- As mentioned, the top soil showed some larger displacement than what was applied to the anchor, even though the material has not been assigned dilative properties.

4.2.2 Model: Rock 1

Model Rock 1 aims to replicate physical test C.1 (0-3 mm eclogite containing 4 % cement). Therefore, the boundary conditions are changed to mimic the modification made to the physical model, as described in Section 3.3.2. The changes to the numerical model are:

- vertically fixed nodes at the surface, extending 4.0 cm in from the top corners, and
- roller conditions on the vertical boundaries, as wall-to-material friction was low in the physical test.

Figure 4.9 shows the modified boundary conditions.

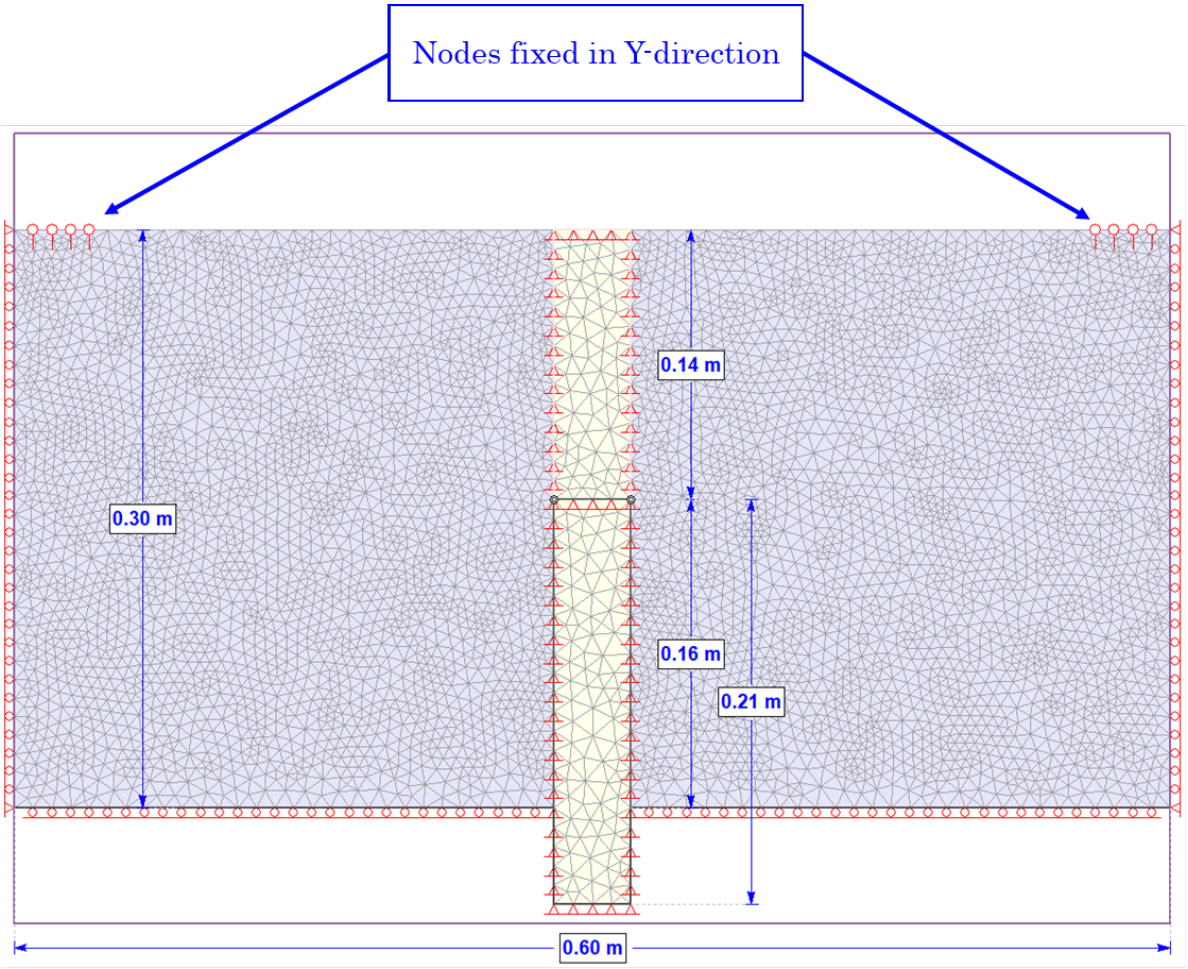

Figure 4.9: Modified boundary conditions for model Rock 1.

Principle Stresses

Model Rock 1 is of a low-cohesive material under hydrostatic, gravitational loading (k=1). Applying a small displacement to the anchor causes a re-orientation of the principle stresses and initiates shear and tensile failure in the material. σ_1 concentrates at a point around 3.5-4.0 cm high on the socket, and branches outward with an inclination to the anchor axis. Stress flow lines in Figure 4.10 show the trajectories of σ_1. They are nearly flat just above the points of failure, and narrow towards the top of the socket, thus creating a wide V- or U-shaped zone of increased pressure.

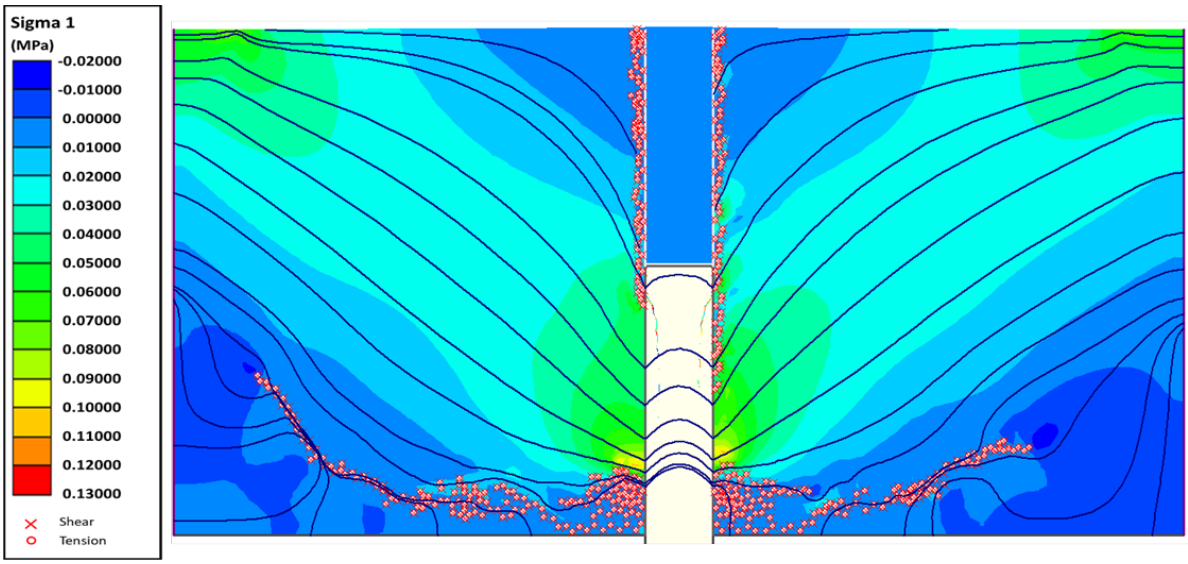

Figure 4.10: σ_1 flow lines (navy) at 0.5 mm anchor displacement.

Pressure within the σ_1-affected zone continues to rise as the anchor displaces upwards, as shown in Figure 4.11 (a). After 5.0 mm anchor displacement, the material fails within the pressure zone, thus creating a new failure body. This causes σ_1 to decrease, and forms a concave pressure arch below the new failure body, as seen in Figure 4.11 (b).

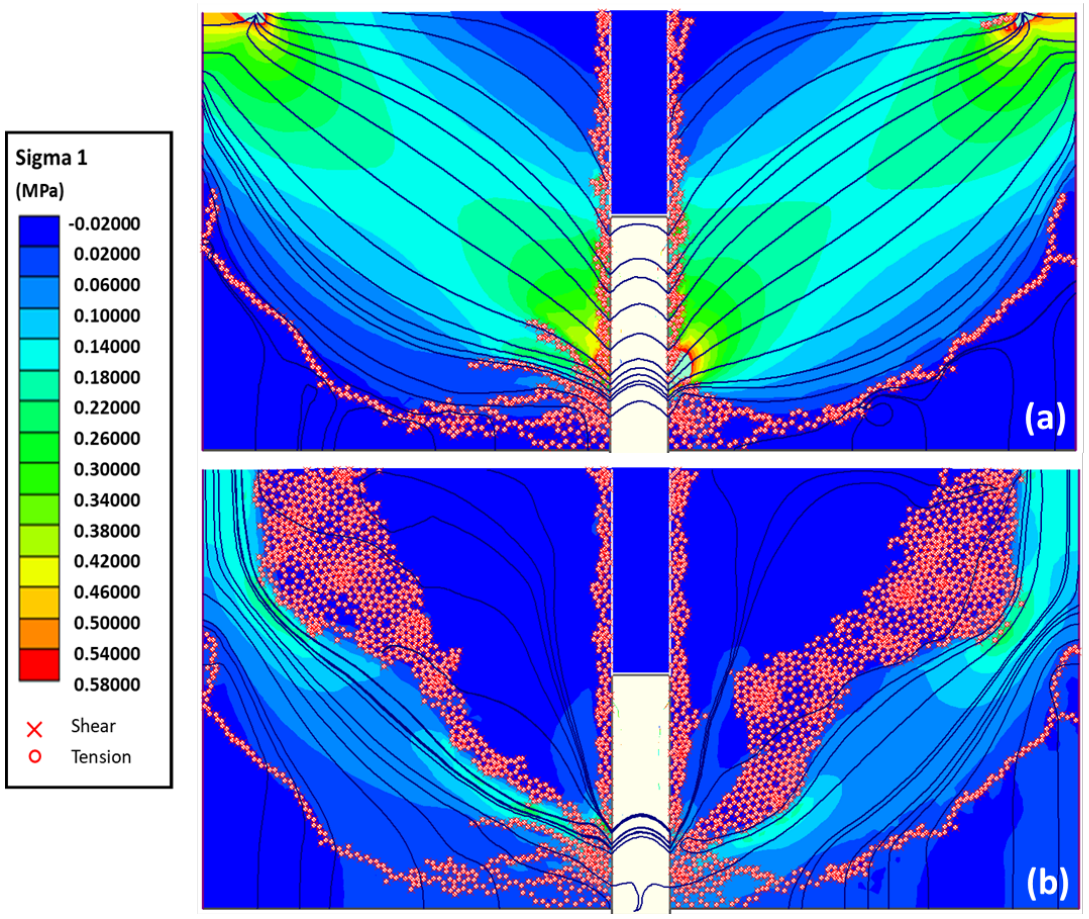

Figure 4.11: σ_1 flow lines (navy) at (a) 4.5 mm and (b) 5.0 mm anchor displacement.

Strain and Failure

As mentioned, shear and tensile failure initiates already before 0.5 mm displacement, branching out in a wide U-shape from below roughly 4.0 cm on the socket. A thin fracture quickly reaches the vertical boundaries (Figure 4.12), following the lower contours of the pressure zone created by σ_1. When the initial fracture has propagated to the walls, new ones emerge from the same location. These have a narrower angle from the anchor axis, between 65°-50°, and extend up to 11 cm into the material.

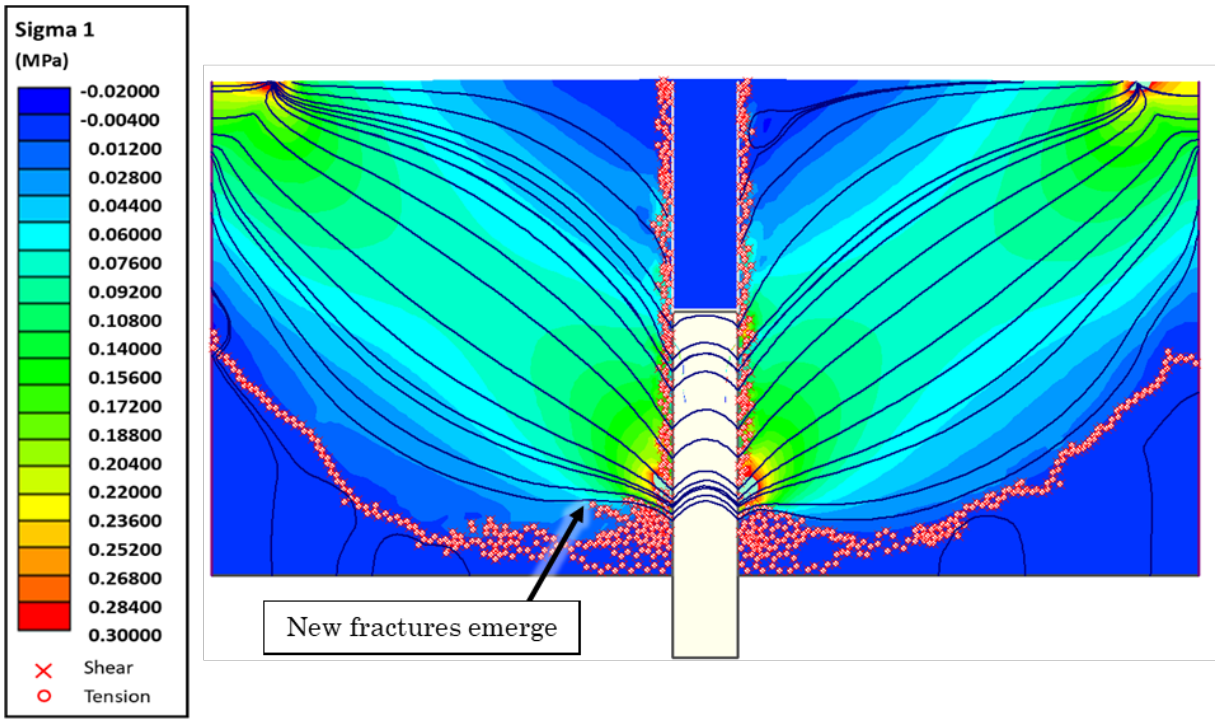

Figure 4.12: Figure showing how the first failure body, σ_1 flow lines (navy) and new fractures emerging, at 2.0 mm anchor displacement.

Strain analysis shows that straining follows the trajectories of σ_1 within the pressure arches. Figure 4.13 shows strain contours taken at 4.5 mm anchor displacement. Zones of maximum strain create approximately 50° to the anchor. After 5.0 mm displacement, new fractures abruptly appear in these zones. They maintain this angle from the socket to points located approximately 10 cm vertically below the fixed nodes on the material surface, as shown in Figure 4.13. From here, a larger zone of shear an tensile failure occurs, and progresses upwards towards the surface. This results in a new, V-shaped failure body defined by these failure zones. The new failure body is shown in Figure 4.14. Material surrounding the anchor block is also in a state of shear and tensile failure.

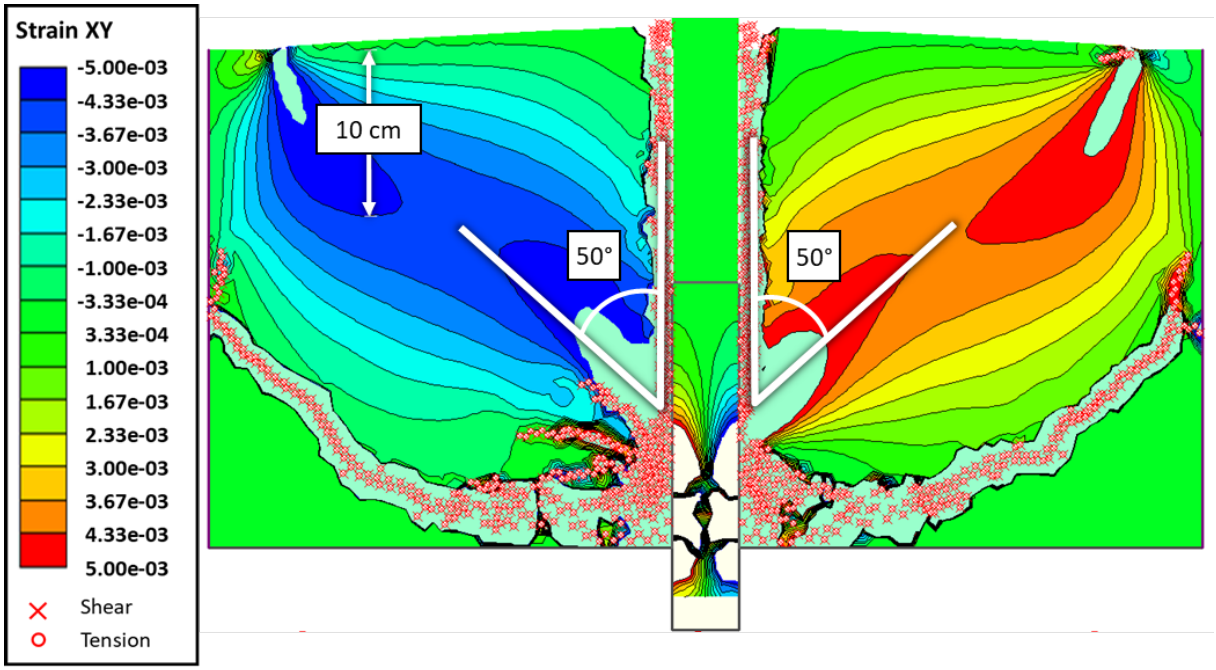

Figure 4.13: Strain contours at 4.5 mm anchor displacement.

Material Displacement

Displacement is largely controlled by the extent of the failure at each stage. The first fracture creates a large body that displaces upwards with the anchor. Below it, the material is at rest. The second failure body, delimited by the 50° inclined fractures, continues to displace with the anchor, while movement below it gradually decreases.

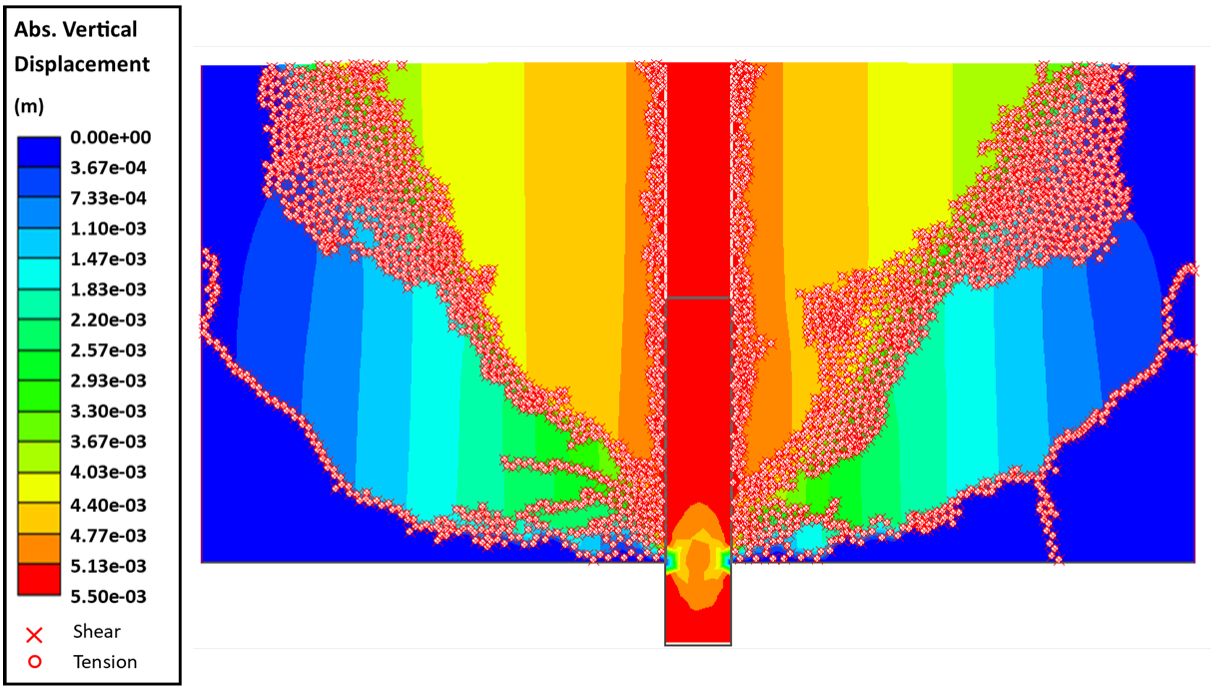

Figure 4.14: Vertical displacement at 5.5 mm anchor displacement, showing a new, clearly developed failure body.

Comments:
The main failure pattern of the physical test (C.1) is successfully reproduced in the numerical model.

4.2.3 Model: Rock 2

The material depth of the model is lowered to 20 cm to replicate physical test C.2 (0-3 mm eclogite containing 2 % cement), see Figure 4.15. Accordingly, model Rock 2 is of a very low-cohesive material under hydrostatic, gravitational loading.

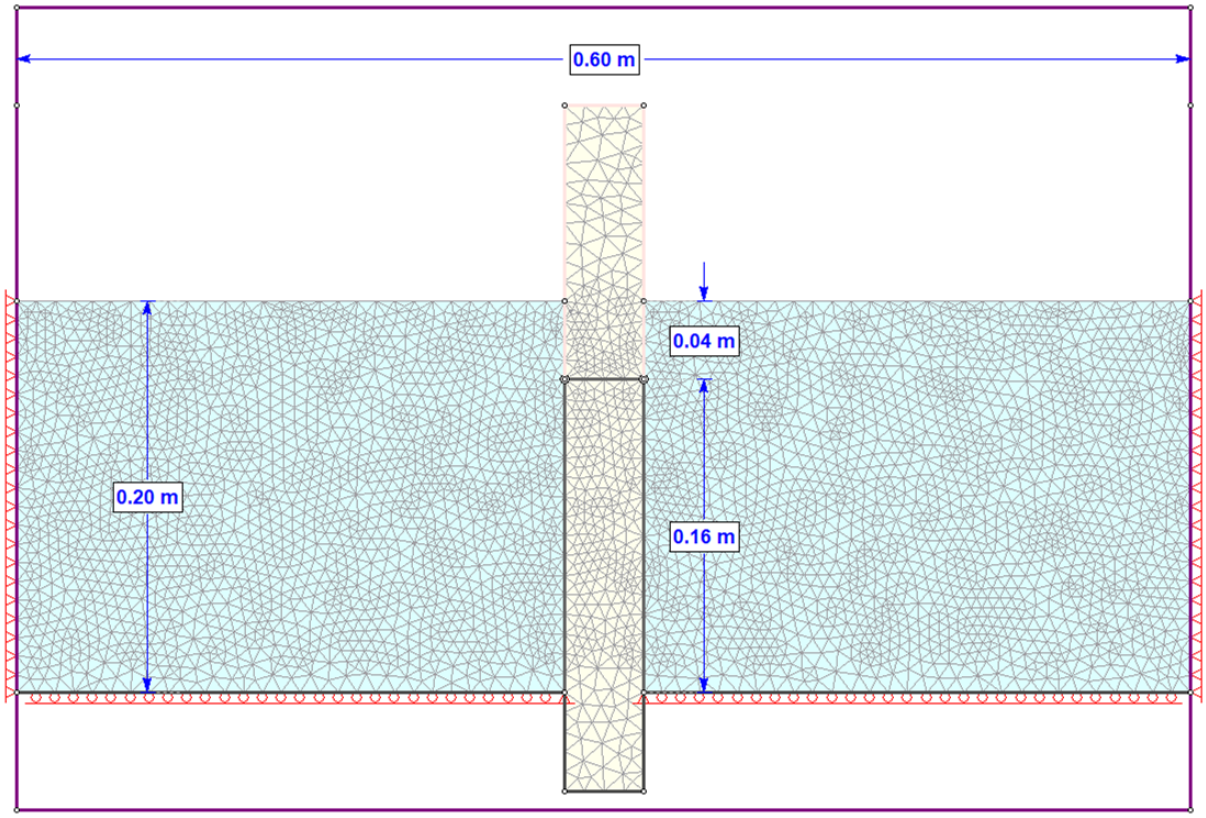

Figure 4.15: Model setup with adjusted material height.

Principle Stresses

Applying a small displacement to the anchor block causes a re-orientation of the principle stresses, as shown by the σ_1 stress flow lines (trajectories) in Figure 4.16, (a) to (c).

- At 0.5 mm anchor displacement, σ_1 creates arched stress flow lines branching out from the socket surface, 2.0-2.5 cm from the anchor base. The flow lines assume a wide angle to the anchor axis, between 60° to 70°, and narrow towards the top. Near the surface, they form convex pressure arches which slope downward towards the vertical boundaries.

- At 1.0 mm anchor displacement, the stress flow lines have developed differently between the left-hand side and the right-hand side. On the left, the stress arch has become more curved, at a steeper inclination from the socket surface. Pressure increases within the zone influenced by the σ_1 arch. On the right hand side, the curvature of the flow lines is less developed.Tensile stresses occur beneath affected zone, while slight pressure increase occurs at the surface of the material.

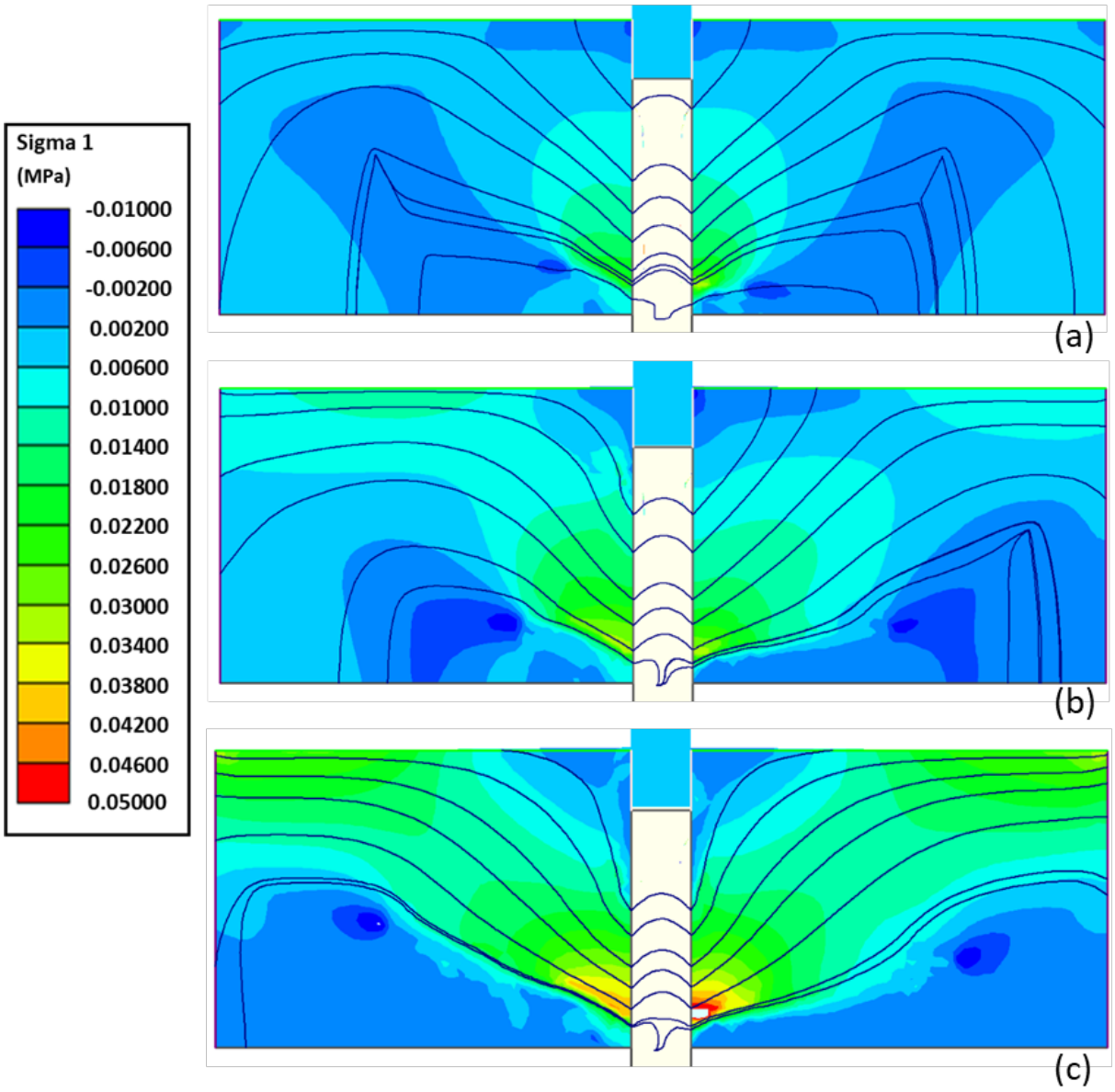

Figure 4.16: σ_1 stress flow (navy colored lines) at 0.5, 1.0 and 2.0 mm anchor displacement.

- At 2.0 mm anchor displacement, which equals the point of maximum resistance in the physical test (C.2), the σ_1 flow lines form a wide V-shaped zone of compression between the socket and thee top corners of the material. The affected zone show a significant stress increase – especially at the apex and the vertical walls, while beneath it, there are areas with material in tension.

- At 5.0 mm anchor displacement, physical tests show that the failure surfaces develop to the upper corners of the material. This stress state involves that the load from the anchor is carried through the failure body, while the underlying material should be unloaded (that is, only gravitational loads). Figure 4.17 confirms that this is the case.

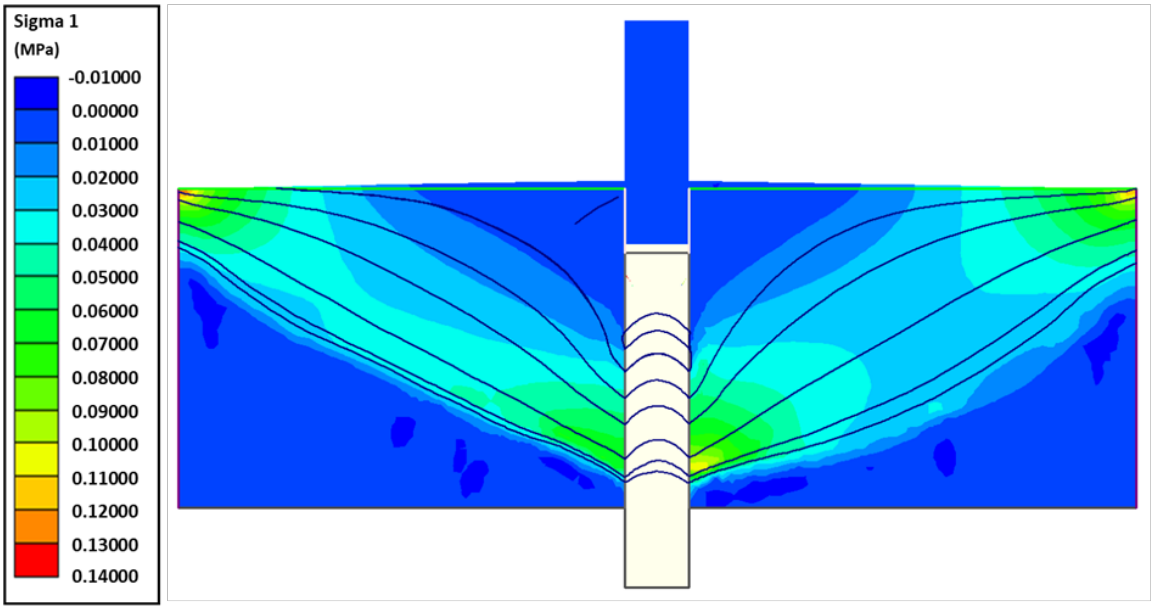

Figure 4.17: σ_1 with flow lines, at 5.0 mm anchor displacement.

Strain and Failure

Both tensile and shear failure initiate at the socket, below the location of stress concentration, i.e. 2.0-2.5 cm from the base. It propagates outward with an inclination around 55-60°, following the σ_1 trajectories. The failure undoubtedly follows the shape of the increased pressure-zone, and coincides with the locations of greatest strain. The fractures and strain zones are inclined at approximately 55-60 degrees from the anchor axis, though curves slightly wider on the right hand side. Figure 4.18 is taken at 2.0 mm anchor displacement, which is when physical tests showed fracture initiation in the center of the material.

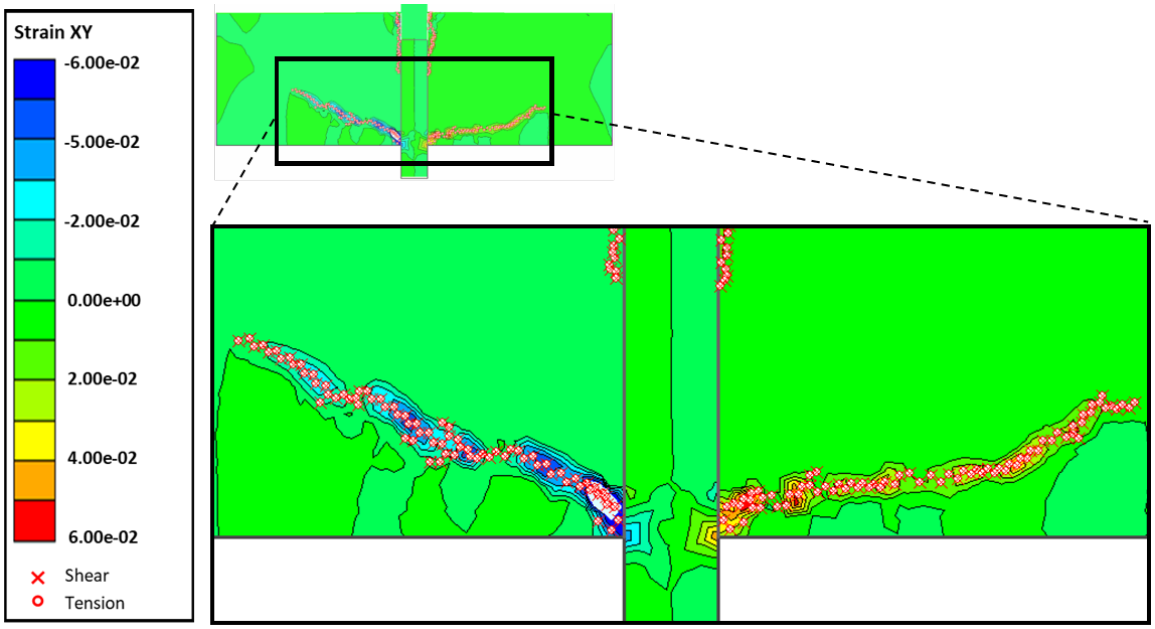

Figure 4.18: Strain contours, with shear and tensile failure indicators, at 2.0 mm anchor displacement.

Physical test C.2 implies that the failure reaches the surface around 5.0 mm anchor displacement. Figure 4.19 shows the extent of the strain zones and failure at this stage.

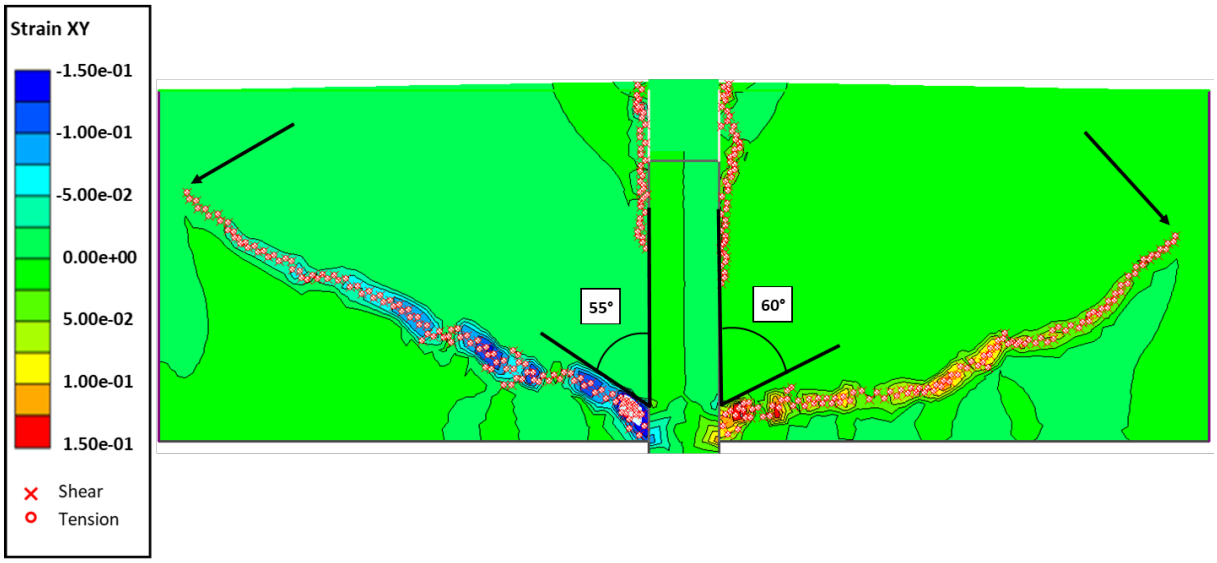

Figure 4.19: Extent of strain zones at 5.0 mm displacement.

Material Displacement

When the fracture development is small, the anchor mobilizes a wide area of the material, though the greatest movement is controlled by the extent of the fractures, as seen in Figure 4.20. As the anchor continues to displace, the fracture extends and creates a clearly delimited uplift body. Below it, the material is at rest, see Figure 4.21.

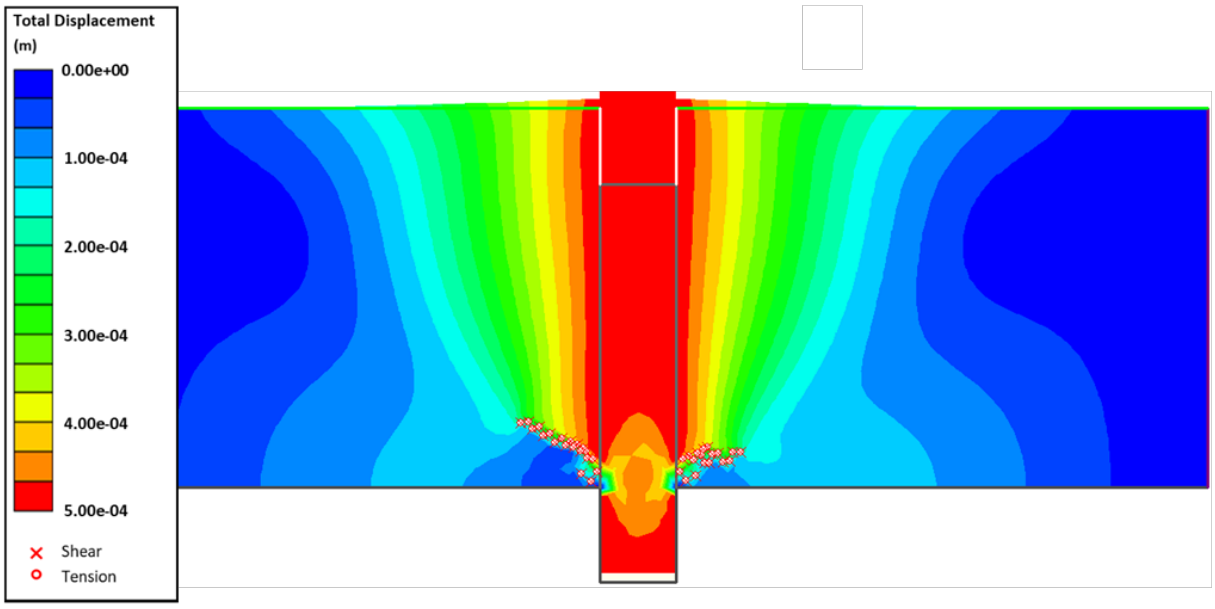

Figure 4.20: Total displacement, with shear and tensile failure indicated at 0.5 mm displacement.

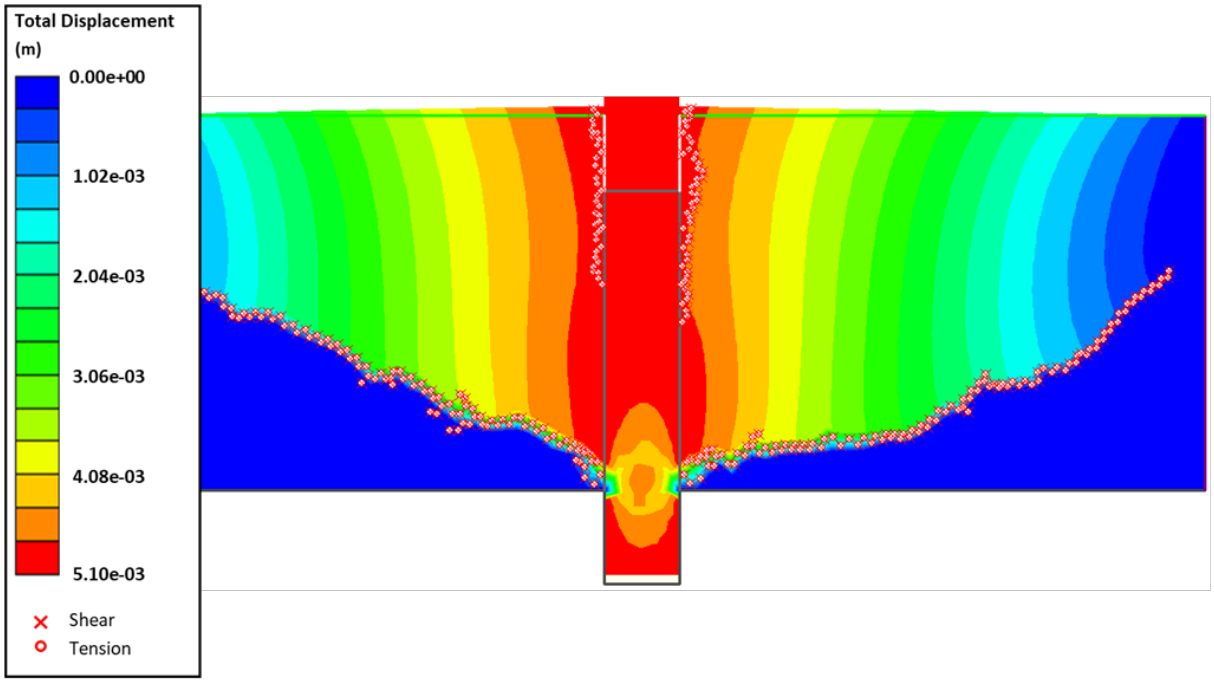

Figure 4.21: Total displacement, with shear and tensile failure indicated at 5.0 mm displacement.

Comments:

- During the physical test, failure propagated *from the center* and reached the socket after roughly 3.0 mm displacement. The model shows no indication of failure initiating from the center of the material, when considering tensile failure, shear failure or large strains.
- Variations between the right and left side are likely because the mesh is not completely symmetric.

5 Discussion

This section will begin with discussing some findings from the physical tests, then continue with a discussion of the results from the numerical analysis', comparing differences and findings between the two. Finally, some comments and model improvements are suggested.

5.1 Physical Model Tests

Results from the physical models tests show some obvious similarities to one another, both regarding the load-displacement curves and failure patterns through the materials.

Load-Displacement Characteristics

Figure 5.1 shows the typical appearance of a the load-displacement plots. In general, the load-displacement reactions can be described by a:

- pre-peak behavior,
- peak resistance,
- post-peak resistance decrease, and
- constant resistance.

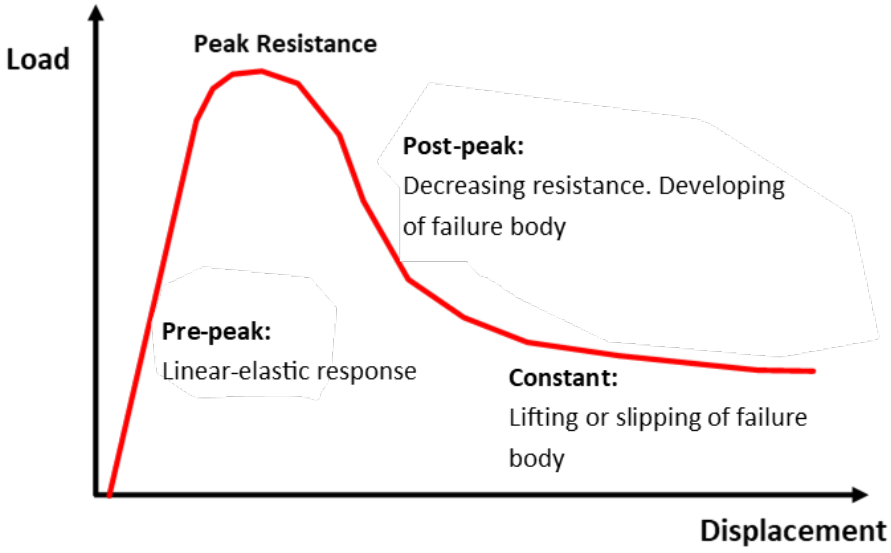

Figure 5.1: Characteristic load-displacement behavior from physical tests.

The pre-peak behavior occurs as an abrupt load increase over a small displacement of 1-2 mm (5 mm in test C.1), in which the resistance increases linearly to approximately 65-95 % of the peak value. The curve's slope reduces (non-linearly) and approaches a convex summit with a peak resistance after roughly 4.0-4.5 mm displacement in the majority of

the tests. During this phase, observable movement occurs in the material, and failure with visible separation initiates before reaching the maximum resistance. The failure continues to develop to the surface past the peak value while the resistance decreases. Eventually, the failure body is either lifted as an intact mass or the material slips off of the anchor block, leading to a constant resistance.

Peak Pullout Resistance
It is interesting that the failure begins to form before the peak resistance is reached in most of the frictional tests, as it indicates that the material may still attain loads even as failure has begun to develop. Also, reaching the peak load does not imply that a complete pullout body has been formed, and the materials provide resistance beyond the peak, until the material eventually slips off the anchor.

A second thing to notice is that the maximum resistance measured in the tests is higher than the sum of the system's average internal friction and the weight of the pullout bodies that are pushed upwards. For instance, take the pullout body that is created by the failure surfaces with an angle α to the anchor axis. The volume of the pullout body is then given by:

$$V = \tan\alpha \times (d - x)^2 \times w \tag{8}$$

where d is the material depth before the test, x is the height to the apex point from the base, and w is the width of the test chamber (100 mm).

The weight of the pullout body is then found by:

$$W = \rho_{comp} \times V \times g \tag{9}$$

where g is the acceleration of gravity, 9.8 m/s^2.

Assuming the system's average internal friction (F_{sys}) as 0.355 kN (average of the empty model values), one may obtain a corrected peak resistance, P_c by subtracting the friction from the peak resistance, i.e. P_c =P-F_{sys}. Then, it is possible to evaluate the resistance that is *not* caused by the weight of the pullout body. As Table 11 shows, the peak resistance (P) exceeds that which can be explained by the weight of the pullout body (W) plus the internal friction of the model. In fact, this extra resistance, (R_e), accounts for up to 85 % of the corrected peak resistance in the frictional materials, and up to an astonishing 98 % in the cohesive materials. Even when assuming the most conservative size of the pullout body, i.e. defined by the widest angles observed in each test (See Table 4), does this resistance exceed the weight.

Similarly, calculations for the cohesive materials are given in Table 12:

From this, it is evident other forces than weight contribute to the anchor's pullout resistance. Please note that the values for R_e/P_c are approximate, as the exact value for F is not known, and W is calculated on the basis of several simple assumptions. However, W

Table 11: Calculation of resistance from weight of pullout body, W, by the widest angles observed in each frictional material test.

Material		**A.1**		**A.2**		**B.1**	**B.2**	
Test no.		*1*	*2*	*1*	*2*	*1*	*1*	*2*
Volume, V	(m^3)	6.12E-03	5.83E-03	6.80E-03	8.02E-03	9.26E-03	4.21E-03	4.90E-03
Weight, W	(kN)	0.126	0.120	0.153	0.181	0.191	0.0870	0.101
P	(kN)	1.20	0.968	1.04	0.853	1.16	0.773	0.901
F_{sys}	(kN)	*0.355*	*0.355*	*0.355*	*0.355*	*0.355*	*0.355*	*0.355*
P_c: P-F_{sys}	(kN)	0.847	0.613	0.685	0.498	0.806	0.418	0.546
R_e: P_c-W	(kN)	0.721	0.493	0.532	0.317	0.615	0.331	0.446
R_e/P_c		85 %	80 %	78 %	64 %	76 %	79 %	82 %

Table 12: Calculation of resistance from weight of pullout body, W, in the cohesive materials.

Material		**C.1**	**C.2**
Volume, V	(m^3)	8.93E-03	5.56E-03
Weight, W	(kN)	0.198	0.127
P	(kN)	11.6	2.50
F_{sys}	(kN)	*0.355*	*0.355*
P_c: P-F_{sys}	(kN)	11.2	2.14
R_e: P_c-W	(kN)	11.0	2.02
R_E/P_c		98 %	94 %

is considered to be conservative, since the weight is calculated for the largest volumes mobilized, and not necessarily the final failure body.

Failure Propagation Through the Material

In all tests with the frictional materials, the failure propagates upward at an inclination from an apex point on the socket. The location of this point varies between the different materials, but remains consistent within the same material. Besides this, there has not been found any correlation between the moisture content or grain size with respect to the apex point's location.

The inclinations of the final failure surfaces typically vary with a few degrees from the peak friction angle, and create delimited straight or curved V-shaped failure bodies. In the case of B.1 (dry, coarse 0.5−6.3 mm eclogite), grains continuously loosened from the uplift body, the angle is considerably lower than both the peak and residual friction angle. The apex also progressed upwards, thus shrinking the failure body. Therefore, the weight of the initial failure body would overestimate the resistance after a certain displacement, as the loose material falls into the void created by the separation.

The two low-cohesive tests had different configurations. C.1 (0.5-6.3 mm eclogite, 4 % cement) had already been lifted with slippage on the sides before the wood blocks were clamped on, as shown in Figure 3.18. Therefore, the initial phase of the test caused a large displacement before approaching the peak value. This is assumed to be caused by the irregular surface pressing against the blocks, having to increase the contact before the stress is large enough to initiate failure in the material. Test C.2 (0.5-6.3 mm eclogite, 2 % cement) had a reduced material height and increased material-wall friction (See Figure 3.20). Despite these differences, the trend of both load-displacement plots show a peak value, followed by a decreasing resistance.

In test C1 the fracture begins to initiate before the peak resistance is reached, however in C.2, the fracture initiates *at* the peak value. The peak values of the cohesive materials are higher than for the soils, and considerably higher in C.1, which contains 4.0 % cement.

Interestingly, the fracture appears to initiate at the center of the cohesive material, and propagates in both directions at an angle, as shown in Figure 3.33 and 3.35. It develops through bridges of intact material between smaller fractures breaking off. The failure form creates a much wider angle than observed in the frictional material, and branches out towards the walls. Even in test C.2, which has a reduced material depth (20 cm), does the failure just barely touch the surface. In C.1, the failure form is clearly affected by the clamped-on blocks.

Failure's Interception with The Horizontal Surface
As the physical tests showed multiple cases of curved failure bodies forming under the load of the anchor, it was of interest to compare the observations to similar findings from other authors. Particularly, how the observed surface interception angle (θ_i) from the tests and the material's friction angle agrees with the interception angle for a circular arc failure (ψ) with end-plate embedded anchors. As θ_i deviated from 2° to 19° – and on average 10° (abs.) – from the calculated ψ, a *clear* agreement may not be claimed to exist between the interception angle from the tests and those expected for a circular arc failure form from end-plated anchors.

5.2 Numerical Simulations

Stress Fields
All three numerical simulations displayed the presence of arching effects as a result of the upward displacement of the anchor, that is:

- re-orientation of the principle stresses, causing σ_1 to concentrate in the shape of a positive (i.e. convex) pressure arch, and
- reduced pressure in the material below the stress arch.

The direction of the arch agrees with the theory of positive arching resulting from the

upward movement of the anchor relative to the materials. Based on the three simulations, it appears that the pressure arch takes a much narrower shape in the frictional material than in the cohesive materials. Compare for instance Figure 4.3 (a) and Figure 4.16 (b). The explanation for this is that the anchor mobilizes a more local zone of the material.Thus, the relative movement between mobilized and stationary soil is greater, which increases the vertical stress component induced by shearing resistance. In cohesive material, the vertical stress component is smaller, causing the pressure arch to be wider. It increases as the anchor continues to be pushed upwards.

The frictional material has a much lower shear strength than the cohesive materials, and no tensile strength. This means that the frictional material quickly enters a state of yielding. As a result of this, stress levels on the socket and in the pressure arch reach much lower values than what is observed in the cohesive materials. On the other hand, stress within the pressure arches reach high values before shear and tensile failure cause the cohesive materials to yield, thus reducing the pressure. Especially in the strongest material (Rock 1), stress is ten-folds greater than in the frictional material at the same anchor displacement, and several times greater than in the weaker Rock 2. It must be noted, however, that a direct comparison between the three models should not be made, as their configurations vary, and not only material the material input parameters.

In general, the stress field in the frictional model varies less with the anchor's displacement than it does in the cohesive materials, where it is largely affected by the extent of shear and tensile failure.

Failure Form

As mentioned, the frictional material quickly enters a state of shearing. Movement mobilizes in the shape of an inverted cone. Its boundaries coincided with the zones of greatest strain, and initiate from the socket surface. This is assumed to represent the uplift body seen in physical tests. At a small displacement, the angles of this greatest strain contours, were roughly equal the peak friction angle – when studying near the socket. After further displacement, they appeared to be controlled by the residual friction angle. The apex point was located 1.0-1.5 cm from the base, which was lower than expected from the physical results. The location of the apex is likely to have been affected by the two fixed nodes where the anchor joint intercepts the bottom, horizontal boundary.

In the cohesive materials, the zones of shear and tensile failure undoubtedly follow the lower "boundaries" of the pressure arches. This is unsurprising, as this boundary divides the material in two states: one more mobilized part with increased pressure, and the underlying part with less movement, which experiences some tensile stresses. Thus, shear and tensile failure follow this boundary at a wide angle from a point some centimeters high on the socket. In the case of Rock 1, this created an initial, large failure body. But due to the fixed nodes on the top corners, stress continued to increase in this failure body

as well, until it failed in a shape that very well represented the physical result. Similarly, Rock 2 failed as a single, wide cone-shape as the failure reached the vertical boundaries. Again, the model showed much similarity to the physical results. This implies that the input parameters agree with the properties of the physical materials, herein the friction angle which was estimated based on the failure angel in C.1 and C.2, and the cohesion determined by use of the friction angle and UCS values from tests. Another parameter was found to have a great influence on the failure shape and extent in the cohesive material, that is, Young's Modulus, E. It was by varying this, that the most resembling models were created.

A difference to comment on, is that failure clearly propagated *from* points on the socket, whereas the fractures first became visible from the *center* of the material in the physical tests. This is the harsh reality of physical and numerical modeling: the material simulated in Rock 1 and Rock 2 is perfectly homogeneous, and the contact with the boundaries is inseparable. In reality – physically – the concrete materials C.1 and C.2 contain air pockets, different mineral grains, varying contact with the socket and side walls, and so on. These are factors that may control the behavior on a micro-scale, which in turn affect the observed results. This is not to say that the numerical models are wrong or do not represent the physical models. The overall results from the numerical models agree well with the results obtained from the physical tests. Therefore, the models are considered to successfully represent the the physical model, despite some minor variations in the apex location and angle of the failure body.

5.3 Comments and Suggestions for Improving of the Models

- Ground anchors are normally loaded in tension from the top, whereas in this setup, the load is applied from the bottom. However, the affect of this different loading setup is considered to be negligible in this study.

- Keep in mind that the numerical model in RS2 by default has 1.0 m depth into the plane, and does not consider friction which may arise between the material av PVC glass in the physical tests.

- As mentioned, the fixed nodes in the numerical models create extreme stresses within the anchor block, and large strain in the neighboring nodes. The unfortunate result of this is that it is not possible to have a load-controlled displacement of the anchor. Thus, one looses one of the parameters which may be validated against the physical data. Attempts were made to calculate the load as a function of the vertical stress on the socket boundary (above the affected, fixed nodes), but the output was unrealistically high, and did not at all agree with the measures loads in the physical tests.

- The models, both physical and numerical, could be improved if the influence of the

lower boundary could be minimized. Especially, if the solution of fixing the nodes at the anchor/bottom frame could be omitted. For instance, the anchor could be installed so that it is entirely within the test chamber, resting on top of a layer om test material. If it is installed onto a steel rod of a *smaller* diameter, which is accurately fit into a slot in the steel frame, then the anchor may be pushed upward, while the effect of the lower boundary is be minimized. Similarly, a numerical model could be created where the anchor is not in contact with the lower boundary, but only the material.

- Additionally, other software may be better equipped for this type of simulations, by allowing for re-meshing between stages (reducing issues of element compatibility), or allowing the contact between the lower boundary and socket to slip.
- To improve the validations of the models, more simulations of frictional soils and cohesive materials should be performed and analyzed, using the same setups, but varying the input parameters.
- Additional parameters could be found for the materials, such as Young's modulus and the dilation angle. The dilation angle is known to affect the capacity of soil anchors.
- The results are valid within the tested materials and the procedures outlined in this thesis. Thus, it may not be appropriate to transfer findings from these models onto larger-scale anchorage in soil or rock masses. However, with further validation of the numerical models, parameter studies may be conducted to gain better insight.

6 Conclusions and Recommendations for Future Work

Conclusions

Failure in homogeneous, frictional materials and low-cohesive materials under the load of a ground anchor has been successfully simulated with a small-scale test apparatus. The main findings regarding failure through the materials are:

- Failure takes the form of an inverted cone.
- The location of the cone's apex point on the anchor depends on the material, but is generally within the bottom 1/4 of the sockets length.
- Failure initiates from the apex point and propagates at an inclination toward the surface.
- The angle of the failure body generally varies with a few degree's from the material's peak friction angle.
- The failure planes commonly curve slightly near the surface, though not in a full-circular shape.
- In most cases, initial pullout mobilizes a much larger portion of soil than what was delimited by the final failure surfaces.
- The cone angle is smaller in frictional materials, and wider in cohesive materials.

All material types displayed similar resistance in response to the anchor's displacement, namely:

1) a pre-peak phase with a linear-elastic response,
2) a peak resistance value,
3) a post-peak phase, with decreasing resistance as the failure body develops towards the surface, and
4) a constant resistance phase, where material either slips off or is lifted by the anchor as a separate, intact failure body.

Peak resistance values in cohesive materials is higher than in frictional materials, and increases with the amount of cohesion. Additionally, the maximum resistance in both the cohesive and frictional materials was shown to be considerably higher than the sum of the weight of the pullout body and the internal friction of the apparatus. This extra resistance has been shown to account for up to 85 % of the peak load in the frictional materials, and up to 98 % in the cohesive materials, when corrected for the apparatus' internal friction. It is safe to conclude that mechanisms other than weight contribute to

the pullout resistance. As the extra resistance occurs in the frictional materials as well, cohesion and tensile strength cannot be the only mechanisms contributing to this extra resistance.

In the majority of the physical tests, the failure initiated before reaching the peak load value. Hence, the anchor may still attain loads even as failure has begun to develop. Also, the peak load does not imply that a complete pullout body has been formed. The material provides resistance beyond the peak.

Numerical models were able to successfully represent most of the findings from the physical tests. From the numerical simulations, it has been shown that arching effect causes a stress increase on the socket and within a positive pressure arch branching from the socket surface. The arch is narrower in the frictional material and wider in the cohesive. The arch angle has been found to largely control the location and extent of failure. Additionally:

- The angles of the greatest strain to the anchor axis in the frictional material coincide with the peak friction angle at a small displacement, then develop to the residual friction angle after a larger displacement.
- The stress arch had a controlling effect on the location of failure in the cohesive materials. Particularly, failure followed the lower boundary of the zone affected by the increased pressure.
- The final failure cones had an angle roughly equal to the peak friction angle of the material.
- Youngs's modulus had a significant influence on the extent of shear and tensile failure in the cohesive materials.

The overall results from the numerical models agree well with the results obtained from the physical tests.

Recommendations for Future Work

More simulations should be performed by using input parameters corresponding to the properties of the tested materials. As the properties are already known and the physical tests performed and recorded, it should be a small work load in return of further validating the numerical models.

The results and conclusions are valid within the tested materials and the procedures outlined in this thesis. Thus, it may not be appropriate to transfer findings from these models onto larger-scale anchorage in soil or rock masses. Future work should therefore involve extending the selection of materials tested physically and simulated numerically. Parameter studies should be conducted with help from the numerical models to assess the influence of each parameter on the results.

There is no denying that the solution of the fixed nodes in the numerical models is not ideal, as they influence the neighboring elements and prevent validation against the load measured during the physical tests. This is considered a major shortcoming in the model layout. The problem might be solved by creating the numerical models in different software, or by minimizing the the effect of the lower boundary with a different setup of the apparatus, and thus, the numerical model.

On a larger scope, the setup should be up-scaled and equipped to facilitate horizontal stresses in the test material. Many variations in test materials, material depth, socket length, and more are necessary to gain a deeper and broader knowledge on failure through both frictional and cohesive materials under the load of anchors.

References

Anon, 1966. Rock foundations – technical engineering and design guidelines as adapted from the us army corps of engineers, no. 16.

Baker, W.H., Konder, R.L., 1966. Pullout load capacity of a circular earth anchor buried in sand. Highway Research Record .

Ball, A., 1961. The resistance to breaking-out of mushroom foundations for pylons.

Bergh-Christensen, J., Ongstad, A., 2010. STREKKFORANKRING I BERG Anchoring in rock, in: Fjellsprengningsteknikk: Oslo, 25. november 2010; Bergmekanikk: Oslo, 26. november 2010; Geoteknikk: Oslo, 26. november 2010, Oslo, Norway. pp. 203–217. URL: https://issuu.com/helligrafisk/docs/bok_fjellsprengningsdagen_2010/203.

BOUASSIDA GEOTECHNICS, . Properties of soils. https://bouassidageotechnics.files.wordpress.com/2016/03/appc_soil_properties_718.pdf Accessed: 19-02-2021.

Brown, E.T., 2015. Rock engineering design of post-tensioned anchors for dams – A review. Journal of Rock Mechanics and Geotechnical Engineering 7, 1 – 13. doi:https://doi.org/10.1016/j.jrmge.2014.08.001.

Coates, D., 1970. Rock Mechanics Principles. Mines Branch monograph, Mines Branch, Department of Energy, Mines and Resources, Canada. URL: https://books.google.no/books?id=ddTEQgAACAAJ.

Drusa, M., Kais, L., Bulko, R., 2014. 3d approach of arching effect in basal reinforcement layer. Procedia Engineering 91, 352–357.

Duncan, C.W., 1999. Foundations on rock. London: SPON EFN .

Handy, R.L., 1985. The arch in soil arching. Journal of Geotechnical Engineering 111, 302–318.

Hinton, E., Owen, D.R.J., 1980. Finite elements in plasticity: Theory and practice. Pineridge Press Limited.

Hobst, L., Zajíc, J., 1983. Anchoring in rock and soil. volume 33 of *Developments in geotechnical engineering*. 2nd completely rev. ed. ed., Elsevier, Amsterdam. Pages: XIV, 570.

Høgset, H.M., 2020. Principles of rock anchoring - a literature study and preparations for numerical modeling. TGB Specialization Project .

Ilamparuthi, K., Muthukrishnaiah, K., 1999. Anchors in sand bed: delineation of rupture surface. Ocean Engineering 26, 1249–1273. URL: https:

//www.sciencedirect.com/science/article/pii/S0029801898000341, doi:https://doi.org/10.1016/S0029-8018(98)00034-1.

International Society for Rock Mechanics, 1978. International society for rock mechanics commission on standardization of laboratory and field tests: Suggested methods for the quantitative description of discontinuities in rock masses, in: International Journal of Rock Mechanics and Mining Sciences & Geomechanics Abstracts, pp. 319 – 368.

ISRM, 1979. Suggested methods for determining the uniaxial compressive strength and deformability of rock materials: Part 1. suggested method for determining deformability of rock materials in uniaxial compression, in: International Journal of Rock Mechanics and Mining Sciences & Geomechanics Abstracts, pp. 137–138.

Jing, L., 2003. A review of techniques, advances and outstanding issues in numerical modelling for rock mechanics and rock engineering. International Journal of Rock Mechanics and Mining Sciences 40, 283–353.

Kang, J., 2007. Soil-Structure Interaction and Imperfect Trench Installations As Applied To Deeply Buried Conduits. Ph.D. thesis. Auburn University, Alabama.

Kim, H.K., Cho, N.J., 2012. A design method to incur ductile failure of rock anchors subjected to tensile loads. The electronic journal of geotechnical engineering : EJGE: World Wide Web journal of geotechnical engineering. 17, 2737–46.

Lai, H.J., Zheng, J.J., Cui, M.J., Chu, J., 2020. "soil arching" for piled embankments: insights from stress redistribution behaviour of dem modelling. Acta Geotechnica , 1–20.

Li, C.C., 2017. Rock Mechanics. Norwegian Univeristy of Science and Technology (NTNU). Trondheim.

Littlejohn, G.S., Bruce, D.A., 1975. Rock anchors state of the art. part 1: Design. Ground Engineering 8.

Littlejohn, S., 1993. Overview of rock anchorages. Pergamon.

Liu, J., Liu, M., Zhu, Z., 2012. Sand deformation around an uplift plate anchor. Journal of Geotechnical and Geoenvironmental Engineering 138, 728–737.

Majer, J., 1955. Zur berechnung von zugfundamenten. Osterreichische Bauzeitschrift 10, 85–90.

Mors, H., 1959. Das verhalten von mastgruendungen bei zugbeanspruchung.

Nickmann, M., Spaun, G., Thuro, K., 2006. Engineering geological classification of weak rocks, in: Proceedings of the 10th International IAEG Congress, Citeseer. pp. 1–9.

Niroumand, H., 2017. Chapter 2 - literature review, in: Niroumand, H. (Ed.), Irregular Shape Anchor in Cohesionless Soils. Butterworth-Heinemann, pp. 3–32. URL: https://

www.sciencedirect.com/science/article/pii/B9780128095508000022, doi:https://doi.org/10.1016/B978-0-12-809550-8.00002-2.

Norwegian Public Road Authorities, 1980. Vegbygging: normaler [håndbok 018].

Norwegian Public Road Authorities, 2004. Intern rapport nr. 2374 – forankring med bergbolter ved fundamentering av støttemurer og landkar på berg.

Norwegian Public Road Authorities, 2010. Håndbok 016-Geoteknikk i vegbygging.

Norwegian Public Road Authorities, 2014a. Geoteknikk i vegbygging: veiledning [Håndbok V220].

Norwegian Public Road Authorities, 2014b. Håndbok V221: Grunnforsterkning, fyllinger og skråninger.

Norwegian Public Road Authorities, 2015. Håndbok r210 laboratorieundersøkelser: 131 sikteanalyse (tørrsikting av vasket materiale). (Hentet 10/07/2020).

Opsal, Ø.L., 2017. Shear strength of dry tills from the southern half of norway in relation to bedrock geology. Norwegian Journal of Geology/Norsk Geologisk Forening 97.

Rocscience, a. Convergence criteria. URL: https://www.rocscience.com/help/rs2/assets/docs/convergence%20criteria.pdf. accessed 17/11/2020.

Rocscience, b. Initial stiffness. URL: https://www.rocscience.com/help/rs2/assets/docs/initial%20stiffness%20method.pdf. accessed 18/11/2020.

Rocscience, c. Stiffness properties. URL: https://www.rocscience.com/help/rs3/Geology/Materials/Stiffness_Properties.htm. accessed 18/11/2020.

Rocscience, 2020. Add a joint boundary in rs2. URL: https://www.rocscience.com/help/rs2/phase2_model/add_joint_boundary.htm?rhhlterm=slip. accessed 31/11/2020.

Showkati, A., Maarefvand, P., Hassani, H., 2015. Stresses induced by post-tensioned anchor in jointed rock mass. Journal of Central South University 22, 1463–1476. doi:10.1007/s11771-015-2664-x.

Terzaghi, K., 1943. Theoretical soil mechanics. johnwiley & sons. New York , 11–15.

U.S. Army Corps of Engineers, 1994. Engineering and design ROCK FOUNDATIONS. Engineering manual No. 1110-1-2908. Department of the Army, Washington DC. ch. 9 pp. 2.

Zhao, J., 2000. Applicability of mohr–coulomb and hoek–brown strength criteria to the dynamic strength of brittle rock. International Journal of Rock Mechanics and Mining Sciences 37, 1115–1121. URL: https://www.sciencedirect.com/science/article/pii/S1365160900000496, doi:https://doi.org/10.1016/S1365-1609(00)00049-6.

Hanna Margrete Høgset

FAILURE IN FRICTIONAL AND LOW-COHESIVE MATERIALS UNDER THE LOAD OF GROUND ANCHORS

NTNU
Norwegian University of
Science and Technology